# LOCAL PHASE MANIPULATION FOR MULTI-BEAM INTERFERENCE LITHOGRAPHY FOR THE FABRICATION OF TWO AND THREE DIMENSIONAL PHOTONIC CRYSTAL TEMPLATES Jeffrey Ryan Lutkenhaus, B.S.

Dissertation Prepared for the Degree of

DOCTOR OF PHILOSOPHY

**UNIVERSITY OF NORTH TEXAS** 

December 2016

#### APPROVED:

Yuankun Lin, Major Professor
Duncan Weathers, Committee Member
Usha Philipose, Committee Member
Hualiang Zhang, Committee Member
David Schultz, Chair of the Department of
Physics
David Holdeman, Dean of the College of Arts
and Sciences
Victor Prybutok, Vice Provost of the Toulouse
Graduate School

Lutkenhaus, Jeffrey Ryan. Local Phase Manipulation for Multi-Beam Interference

Lithography for the Fabrication of Two and Three Dimensional Photonic Crystal Templates.

Doctor of Philosophy (Physics), December 2016, 156 pp., 1 table, 61 figures, 178 numbered references.

In this work, we study the use of a spatial light modulator (SLM) for local manipulation of phase in interfering laser beams to fabricate photonic crystal templates with embedded, engineered defects. A SLM displaying geometric phase patterns was used as a digitally programmable phase mask to fabricate 4-fold and 6-fold symmetric photonic crystal templates. Through pixel-by-pixel phase engineering, digital control of the phases of one or more of the interfering beams was demonstrated, thus allowing change in the interference pattern. The phases of the generated beams were programmed at specific locations, resulting in defect structures in the fabricated photonic lattices such as missing lattice line defects, and singlemotif lattice defects in dual-motif lattice background. The diffraction efficiency from the phase pattern was used to locally modify the filling fraction in holographically fabricated structures, resulting in defects with a different fill fraction than the bulk lattice. Through two steps of phase engineering, a spatially variant lattice defect with a 90° bend in a periodic bulk lattice was fabricated. Finally, by reducing the relative phase shift of the defect line and utilizing the different diffraction efficiency between the defect line and the background phase pattern, desired and functional defect lattices can be registered into the background lattice through direct imaging of the designed phase patterns.

Copyright 2016

by

Jeffrey Ryan Lutkenhaus

#### **ACKNOWLEDGEMENTS**

First, I would like to recognize the intellectual and financial support of my advisor and dissertation committee chair, Dr. Yuankun Lin. Through the Research Assistantship generously provided by Dr. Lin, I have been fortunate enough to work in a laboratory environment for the last 5 years, learning applicable skills, publishing papers in peer-review journals, and travelling to Photonics West each year. I am grateful and proud to have learned and studied under his guidance and wisdom.

I would like to also thank the members of my dissertation committee, Dr. Duncan Weathers, Dr. Usha Philipose, and Dr. Hualiang Zhang. Your guidance through this process has been an immense help. I thank you heartily for your time and consideration, given your busy schedules.

My fellow colleagues in the lab, David George, David Lowell, Murthada Adewole, Mojtaba Moazzezi, Kris Ohlinger, and Safaa Hassan, also deserve recognition for the invaluable aid they provided for this research and the many enlightening conversations and discussions.

Above all others, I would like to thank my wife, Ileana, for her constant, unwavering love, patience, and support, and without whom, I might not have even pursued a graduate degree. Her loving encouragement and complete confidence in my abilities led to me reaching that which I previously believed to be unreachable. I also want to thank my son, Luke, for bringing so much joy into my life.

Finally, I thank God for all the blessings that I have in my life and for sending me down this path.

## TABLE OF CONTENTS

Pa	ge
CKNOWLEDGEMENTS	.iii
ST OF TABLESv	/iii
ST OF FIGURES	.ix
ST OF ACRONYMSx	κxi
HAPTER 1 INTRODUCTION	. 1
1.1 Motivation	. 1
1.2 Outline of Dissertation	. 3
HAPTER 2 FUNDAMENTALS OF PHOTONIC CRYSTALS	. 7
2.1 Maxwell's Equations to the Wave Equation	. 7
2.2 Scale Invariance	. 9
2.3 Photonic Crystal Lattices	11
2.4 Unit Cells and Brillouin Zones	16
2.5 Photonic Bands and the Band Gap	19
2.6 Defects in Photonic Crystals	26
HAPTER 3 FABRICATION OF PHOTONIC CRYSTALS	29
3.1 Overview of Photonic Crystal Fabrication Methods	29
3.2 Interference	32

3.3	Photoresist and Fabrication	36
3.4	Methods of Holographic Lithography	39
СНАРТ	ER 4 SPATIAL LIGHT MODULATORS	47
4.1	General Information	47
4.2	Phase Modulation from Liquid Crystals	48
4.3	4f Imaging System and Fourier Transforms	51
4.4	Spatial Light Modulators in Holographic Lithography	54
СНАРТ	ER 5 HOLGRAPHIC FABRICATION OF 3D PHOTONIC CRYSTALS USING A SILICON-	BASED
REFLEC	TIVE OPTICAL ELEMENT	55
5.1	Fabrication of the Reflective Optical Element	55
5.2	Five Beam Interference from Reflective Optical Element	57
5.3	Holographic Fabrication of Woodpile Photonic Crystal Templates	60
CHAPT	ER 6 DIGITALLY TUNABLE HOLOGRAPHIC LITHOGRAPHY USING A SPATIAL	LIGHT
MODUI	LATOR AS A PROGRAMMABLE PHASE MASK	65
6.1	Experimental Setup	65
6.2	Phase Pattern Design	67
6.3	Determination of the Phases of the Diffracted Beams	69
6.4	Holographic Fabrication	74
6.5	Further Discussion	75

CHAPTER 7 HOLOGRAPHIC FABRICATION OF FUNCTIONALLY GRADED PHOTONIC LATTICES
THROUGH SPATIALLY SPECIFIED PHASE PATTERNS80
7.1 Background Phase Pattern80
7.2 Missing Lattices in Periodic Photonic Lattices
7.3 Embedding Single Motif Lattices in Dual Lattice Photonic Structures 85
CHAPTER 8 GRADIENT INDEX STRUCTURES THROUGH SPATIAL LIGHT MODULATOR BASED
HOLOGRAPHIC LITHOGRAPHY91
8.1 Pixel-by-Pixel Phase Engineering
8.2 Effective Refractive Index of Holographically Fabricated Structures
8.3 Demonstration of Simple Gradient Index Structures using the SLM
CHAPTER 9 REGISTERING FUNCTIONAL DEFECTS INTO PERIODIC HOLOGRAPHIC STRUCTURES
9.1 Design and Fabrication of Desired Defects with Different Filling Fractions
9.2 Registering Desired Defects with 90° Bend with Periodic Structures
CHAPTER 10 HOLOGRAPHIC FABRICATION OF DESIGNED FUNCTIONAL DEFECT LINES IN
PHOTONIC CRYSTAL LATTICES USING A SPATIAL LIGHT MODULATOR
10.1 Theory
10.2 Functional Defect Lines in Square Photonic Lattices through 5-Beam Interference 123
10.3 Functional Line Defects in Square Photonic Lattices through Three-Beam
Interference

10.4	45° Orientation of Functional Line Defect in Square Photonic Crystal Lattice	129
10.5	Registering the Functional Line Defect in Square Photonic Crystal Lattices	131
CHAPTER	11 CONCLUSION	134
BIBLIOGR	APHY	136

## LIST OF TABLES

Table 3.1. A comparison of different methods of fabricating photonic crystals	30
---	----

# LIST OF FIGURES

Figure 2.1. The five Bravais lattices in two dimensions
Figure 2.2 Five of the 14 Bravais lattices in 3 dimensions, organized into 7 groups. Table in lower
right lists lattices not shown
Figure 2.3(a) Square lattice and (b) hexagonal lattice with lattice vectors, primitive cells, and
Wigner-Seitz cells specified
Figure 2.4. Wigner-Seitz cells for simple cubic, body-centered cubic, and face-centered cubic
lattices
Figure 2.5. First and Irreducible Brillouin zones for reciprocal (a) square and (b) hexagona
lattices
Figure 2.6. Brillouin zone of fcc lattice with irreducible Brillouin zone shown. Image from
Wikimedia Commons
Figure 2.7. (a) diagram of a 1D photonic crystal (dielectric stack). (b) Dispersion relation (band
diagram) for the structure in (a). Bandgap highlighted in yellow
Figure 2.8. Band diagram for 2D square lattice of dielectric cylindrical rods in air, a schema of
which is shown in the right side of the figure23
Figure 2.9. Band diagram of diamond lattice of air spheres in dielectric. Inset shows
arrangement of spheres in lattice
Figure 2.10. (a) Diagram of idealized woodpile structure. (b) Scanning electron microscope
(SEM) image of a woodpile photonic crystal template, viewed from above the structure. The
first, second, and third layers are visible
Figure 2.11. Diagram illustrating defect types in a 2D square lattice of isolated rods

Figure 2.12. FDTD simulation of electric field of propagating TM-polarized light in photonic
circuit in a 2D square lattice of isolated dielectric rods. The light propagating through the circuit
has a frequency within the photonic bandgap, and is confined to the circuit. Bends, splitters,
and channel-drop filters are present in the circuit
Figure 3.1. Chart showing iso-intensity surfaces for interference patterns from the interference
of (a) 2, (b) 3, and (c) 4 beams (3 side beams + 1 central beam). Polar interference angle with
optical axis is identical for all side beams. Azimuthal angles between side beams are (a) 180°,
(b) 120°, and (c) 90 for angle between k1 and k2, and between k2 and k3
Figure 3.2. Interference patterns of 4 side beams and a central beam (4+1) with (a) all of the
beams having the same phase, and (b) two of the side beams with phases shifted by $\pi/2$
relative to the other two side beams
Figure 3.3. Simulated effects of exposure threshold in MATLAB. (a) Longer exposure to laser
interference pattern leads to higher fill fraction and interconnected structure. (b) Shorter
exposure produces lower fill fraction and a lattice of isolated ellipsoids
Figure 3.4. Diagram of an example of a conventional holographic lithography setup. The beam is
expanded by the spatial filter (SF) and the polarization is adjusted by the waveplate (WP) before
it is split by the first beam splitter (BS). The two beams are split once again to produce 4 beams,
which are then directed by mirrors (M) to interfere at the photoresist sample. In the dashed
box, there are 12 bulk optical elements
Figure 3.5. Top cut prism with aperture to select beams and block unwanted illumination. This
example shows a TCP capable of generating 4 side beams and a central beam. Interference of
the beams occurs outside the bottom of the prism (shown to the right in this figure) 41

Figure 3.6. Diagram of single reflective optical element setup
Figure 3.7. (a) Single-layer DOE made of 4 diffraction gratings symmetrically arranged around a
mask. Diffracted beams are interfered beneath the DOE. (b) 3-layer DOE made of two
orthogonally-oriented gratings with a spacer in between
Figure 4.1. Diagram of the structure of a LCoS-SLM, broken down into layers 48
Figure 4.2. (a) Index ellipsoid for uniaxial LC molecule. Refractive indices along the principal
axes are shown. (b) Orientation of nematic LC molecules in a LC cell. The average orientation is
parallel to the director, but the positions of the molecules are random. (c) Schematic showing
the orientation of parallel-aligned nematic (PAN) LC molecules in a pixel between transparent
electrodes. The director of the LC layer is parallel to the surface of the electrodes 49
Figure 4.3. Diagram of 4f imaging system used in SLM optical setup
Figure 4.4. (a) 2D binary checkerboard phase pattern to be displayed on the SLM. (b) Fourier
plane image of beams diffracted from the SLM while the pattern in (a) was displayed 52
Figure 5.1. Fabrication process of the silicon-based reflective optical element. (a) The prism is
seated into the plastic window. (b) The PDMS forms a mold around the prism. (c) The prism is
removed and the silicon strips are placed in the inner facets of the PDMS mold. (d) The cross
aperture is placed on top of the mold
Figure 5.2. (a) Three beam interference pattern. (b) Five beam interference pattern, shifted by
0.25c due to phase delay 59
Figure 5.3. Schematic of the experimental setup for the fabrication of woodpile-like photonic
crystal templates using the single silicon-based reflective optical element

Figure 5.4. (a) Optical microscope image (40X) of 3D photonic crystal template in DPHPA
fabricated using single silicon based reflective optical element. (b) Optical microscope image of
close-up of an area of 3D photonic crystal template
Figure 5.5. (a) AFM image of holographically fabricated 3D photonic crystal template in DPHPA
with incident angle of 78°; (b) Surface profile measured along the red line in (a); (c) SEM image
of woodpile-like structure in photonic crystal template in DPHPA with incident angle of 78°; (d)
AFM image of photonic crystal template in DPHPA with incident angle of 74.9°; (e) Plot of
surface profile measured
Figure 6.1. Diagram of experimental setup for the use of the SLM for holographic lithography.
BE: Beam Expander, SLM: Spatial Light Modulator, L1: 1st lens (f1 = 400mm), FF: Fourier Filter,
L2: 2nd lens (f2 = 200mm), MO: 20X Microscope Objective lens, TS: Translation Stage, CCD: USB
camera. The CCD and sample stage were interchangeable upon the translation stage 66
Figure 6.2. (a) A tile unit of the phase pattern displayed on the SLM. The orange lines are drawn
on the pattern to assist in the viewing of the hexagons and the triangles (I thru VI) in the
hexagons. The gray levels of the triangles are set digitally. (b) Enlarged view of phase pattern
with a scheme showing diffraction directions and spots. (c) Photograph of diffraction pattern in
Fourier plane (2f point) taken with a USB CCD camera. Diffraction spots in between the dotted
red lines are the 1st order diffracted beams
Figure 6.3. (a) Enlarged view of the pattern from Figure 6.2(a) with hexagonal unit cell overlaid
in orange. Green circles indicate the beams diffracted from the pattern on the SLM. (b) Close-
up of red-highlighted kite-shaped region in (a). The phases of the beams are determined by the
average of the gray levels in each kite-shaped region 70

Figure 6.4. (a1, a2, a3) Hexagonal phase patterns with unit cell drawn in orange, and gray level of 153 for all gray triangles contributing to beam phases. (a2) Phase pattern with 102 gray level for dark gray triangles. (a3) Phase pattern with 51 gray level for dark gray triangles. (b1, b2, b3) Simulated four beam interference patterns for the beams with phases determined by the phase patterns in (a1, a2, a3), respectively.  $\alpha$  and  $\beta$  in (b1) designate the lattice constants. In (b2), the black arrows show the direction that the pattern shifts due to the change in phase. (c1, c2, c3) are CCD images of the four beam interference patterns captured after the microscope objective Figure 6.5. (a) Optical microscope image (40X) of 2D photonic crystal template in DPHPA, holographically fabricated using the phase pattern in Figure 6.4(a1) displayed on the SLM. (b) SEM image of fenced-in cylinder structures fabricated in DPHPA. (c) Close-up view from the sample seen in the SEM image in (b). (d) AFM image of photonic crystal template in DPHPA. (e) Figure 6.6. (a) Tile unit of a phase pattern with triangles (I-VI) all set to different gray levels. (b) Enlarged view of the pattern from (a) with hexagonal unit cell overlaid in orange. Green circles Figure 6.7. (a) Simulated four beam interference pattern for beams (1, 3, 4, 5) from Figure 6.6(b) generated by the phase pattern in Figure 6.6 (a) with phases determined by Eqs.(6.6)-(6.11). (b) CCD image of four beam interference pattern generated with the phase pattern in 

Figure 6.8. (a, b, c) Simulated four-beam interference patterns formed from beams 1, 3, 4, and
5, with phases of the beams assigned by the gray levels in the phase patterns in Figure 6.4(a1,
a2, a3), respectively78
Figure 7.1. (a) Detailed schematic of background phase pattern displayed on the SLM. (b) CCD
image of Fourier plane diffraction pattern from the laser diffracting from the phase pattern in
(a) displayed on the SLM. (c) Diagram of 4f setup showing diffraction angles ( $\theta_1$ ) and
interference angles ( $\theta_2$ )
Figure 7.2. (a) Simulated interference pattern with missing lattice line defect (dark line). (b)
SEM image of holographically fabricated structures in DPHPA photoresist with the designed
missing lattice line defect. (c) AFM image of the missing lattice line in the fabricated structures.
(d) AFM profile along the purple line crossing the dark line defect. (e) AFM profile along the
orange line running parallel to the dark line defect
Figure 7.3. (a) Enlarged view of embedded phase pattern in the majority phase pattern for
single lattice defects in dual-lattice bulk structure. The red, green, blue, and yellow hexagons
represent the boundary of the defect region. (b1) Basic hexagonal unit cell with different gray
levels in the six equilateral triangles that compose it. (b2) Orange hexagonal unit cell indicates
diffraction orientation and phase determined by gray levels in the majority background pattern.
(b3) Purple hexagonal unit cell indicates diffraction orientation and phase determined by gray
levels in the embedded defect region. (c) Different gray levels in the six triangles linked by (c1)
green, (c2) yellow, (c3) blue, and (c4) red hexagons corresponding to the hexagons of the same
color in (a)

Figure 7.4. (a) Diffraction pattern from the spatially variant phase pattern in Figure 7.3(a). (b)
CCD image of interference pattern in 4f region. (c) Simulated interference pattern for (c1) single
and (c2) dual lattice regions. (d) SEM image of holographically fabricated structures with single
lattice defect embedded in a dual lattice background
Figure 7.5. (a) SEM image of fabricated photonic structures with defect boundary marked by
red, green, blue, and yellow hexagons. (b) Simulated interference patterns for the boundary
regions indicated by (b1) red, (b2) green, (b3) blue, and (b4) yellow
Figure 8.1. (a) An enlarged portion of the phase pattern displayed on the SLM for the
generation of four 1st order beams. Each dark gray or light gray square is a single pixel
measuring 8 $\times$ 8 $\mu m$ in size. The orange box is drawn on the phase pattern to indicate the tile
unit of $2 \times 2$ pixels that is repeated to create the phase pattern. (b) Close up view of the pattern
from (a) with square unit cell overlaid in purple. Green circles indicate the beams diffracted
from the pattern on the SLM. (c) Photograph in Fourier plane of diffraction pattern generated
by the phase pattern in (a)
Figure 8.2. (a1) Enlarged portion of phase pattern with pixels I and III having a gray level of 30,
and pixels II and IV having a gray level of 94. (a2) CCD image of interference pattern formed
from beams generated by laser incident on SLM displaying pattern in (a1). (a3) Simulated iso-
intensity surfaces of unit cell of interference pattern in (a2). (b1) Enlarged portion of phase
pattern with pixels I and III having a gray level of 30, and pixels II and IV having a gray level of
255. (b2) CCD image of interference pattern from phase pattern in (b1). (b3) Simulated iso-
intensity surfaces of unit cell of interference pattern in (b2)

Figure 8.3. (a) SEM image of fabricated woodpile photonic crystal template in DPHPA
photoresist mixture. (b) AFM image of woodpile template. (c1) Surface profile along the red
line in (b). (c2) Surface profile along green line in (b)
Figure 8.4. (a) Schematic of a 5 beam interference. Iso-intensity surfaces of the unit cells of the
periodic five-beam interference pattern with one beam phase shifted by $0\pi$ (b), $0.6\pi$ (c), and
1π (d)
Figure 8.5. (a) Supercell phase tile assembled from unit cell tiles from Fig. 12(a1) & (b1). (b)
View of portion of phase pattern made from supercell phase tile in (a); repeat unit indicated.
(c) CCD image of the interference pattern in the 4f region, generated by tiling the supercell
phase tile in (a) across the entire SLM, and interfering the diffracted 0th order and four 1st
order beams
Figure 8.6. (a) Composite phase tile constructed from smaller phase tiles, which is repeated
across the SLM to produce a total phase pattern. (b) Photograph of diffraction pattern in the
Fourier plane generated by the phase pattern in (a); beams allowed to pass through the Fourier
filter are circled in red. (c) Phase tile with (1) 24 pixel period and (2) single pixel period. (d)
Fourier plane photographs of diffraction pattern from the phase pattern using the (1) (c1) tile,
and (2) the (c2) tile
Figure 8.7. (a) Two 2D intensity profiles taken at different planes in the axial direction, showing
the change in the interference pattern produced by the allowed beams in Figure 8.6(b). (b) CCD
image of the interference pattern produced by the superposition of the allowed beams in
Figure 8.6(b) at the 4f point. (c) Optical microscope image (40X) of holographically fabricated
structures in DPHPA

Figure 9.1. (a) Phase pattern with selected reduced area triangles designed using MATLAB program. The purple hexagon indicates the unit cell of phase pattern. Adjustable gray level and area of triangles labeled 1-6: the area of triangles 2, 4, & 6 were reduced to 75% of the size of triangles 1, 3, & 5. Beam 1 phase determined by the average gray level in the kite shaped area with red border in (a). (b) Simulated Fourier plane diffraction with 1st order diffracted beams labeled 1-6. Green circles indicate holes in the Fourier filter that allow first order diffracted Figure 9.2. Enlarged view of phase pattern with defect area. Region 1 triangle gray levels were {153,51,153,51,153,51}. Region 3 triangle gray levels were all 153. Region 2 triangle gray levels were {204,153,204,153,204,153}. The areas of the triangles in region 2 with gray levels of 204 were 75% of those with gray levels of 153.......108 Figure 9.3. (a) Fourier transform simulated interference pattern using the phase pattern in Figure 9.2 with a linear gamma curve. The red and white arrows point to boundaries between the defect region and the background. (b) Optical microscope image of fabricated structures in DPHPA. The red rectangle indicates the location of the defect produced from the interference region corresponding to regions 2 and 3 in the phase pattern. The orange dotted line indicates the boundary lattice between regions 2 and 3. The red arrow points to the right edge of the Figure 9.4. (a) Non-linear gamma curve provided by HoloEye. The two black squares represent the gray levels of 51 and 53. (b) Simulated interference pattern using the non-linear gamma curve. White rectangle indicates the location of the defect region corresponding to regions 2 and 3 in the phase pattern from Figure 9.2. (c) Optical microscope image of structures

holographically fabricated in DPHPA using the phase pattern from Figure 9.2 and the gamma curve in (a). White lines indicate the corners of the defect region, and the yellow dotted line indicates the boundary region between regions 2 and 3......111 Figure 9.5. (a) Background phase pattern of a periodic square lattice where a desired defect will be registered. (b) Enlarged view of the phase pattern of desired defects with a 90° bend (c) Enlarged view of phase pattern with phase of defect region and background calculated simultaneously. (d) Optical microscope image of fabricated thin-film sample using the phase Figure 9.6. (a) Enlarged view of the phase pattern with a 90° bend defect embedded in a uniform background phase with defect region and background phase calculated separately. (b) Photograph of diffraction pattern in Fourier plane produced by phase pattern in (a). (c) Figure 9.7. (a) Simulation of 4f interference pattern using Fourier transform of light allowed to pass through the Fourier filter as indicated in Figure 9.6(b). (b) Simulation of 4f interference pattern if the zero-order diffraction spot is blocked. (c) Optical microscope image (25X) showing a fabricated spatially variant 2D photonic crystal template with a 90° bend defect in a uniform Figure 10.1. (a) An enlarged view of the checkerboard phase pattern displayed on the SLM. The dashed purple square indicates the size of one unit cell of 8 x 8  $\mu$ m<sup>2</sup>. (b) CCD image of the diffraction pattern at the Fourier plane. The red circles indicate beams passing through the Fourier filter. (c) Scheme of the five beam interference arranged four-fold symmetrically. Beam

5 propagates along the z-axis. (d) Simulated intensity distribution for the interference of the
four first order beams with the central zero order beam
Figure 10.2. (a) Checkerboard phase pattern (with gray levels 30 and 255) and designed line
defect (gray level 255). Each bright or dark square in the pattern represents a single square SLM
pixel. (b) Close-up of portion of line defect in phase pattern. Arrows indicate the direction of
the lattice shift due to the phase shift. Red square represents the unit cell for calculating phases
of the interfering beams. (c) Optical microscope image of fabricated structures in DPHPA. Scale
bar measures 8 microns
Figure 10.3. (a) Checkerboard phase pattern with black (gray level 30) defect line. (b) Enlarged
view of line defect in phase pattern. Arrows indicate the direction of the lattice shift due to the
presence of the line defect phase. The red square represents the unit cell for calculating phases
of the beams. (c) Optical microscope image of line defect embedded in PhC lattice in DPHPA
fabricated through holographic lithography. Scale bar measures 8 microns
Figure 10.4. (a) CCD image of the diffraction pattern at the Fourier plane. The red circles
indicate beams passing through the Fourier filter. (b) Interference pattern of two 1st order side
beams with the central zero order beam. Scheme of white (gray level 255) (c) and dark (gray
level 33) (d) defect phase. Blue arrows indicate direction of the lattice shift due to the presence
of the defect. (e-f) Optical microscope images of fabricated defects in PhC lattice using the
defect phases in background phase pattern in (c-d), respectively. Scale bar measures 8 microns.
Figure 10.5. (a) Enlarged view of a diagonal line defect phase in the checkerboard phase
pattern. (b) Diagram of defect phase with accompanying lattice shifts indicated by the red

arrows. (c) Optical microscope image of fabricated structures in DPHPA produced by
overlapping two of the 1st order beams with the central zero order region diffracted from the
phase pattern in (a) displayed on the SLM. The red arrow indicates the pattern shifting
direction. The dashed blue line indicates the location of lattices if there is no pattern shifting.
Scale bar measures 8 microns
Figure 10.6. (a) CCD image of the diffraction pattern in the Fourier plane f1. All images are
rotated 45 degrees to orient the defect along the horizontal direction. Beams 1 and 2 were
filtered out with a mask. (b) The phase pattern displayed on the SLM and an optical microscope
image of the fabricated structure. The background of the SLM image consists of single pixels of
grey levels 254 and 158 and in the defect, the grey pixels have been changed to 224. (c) CCD
image of the interference pattern and optical microscope image of the recorded interference
generated by the phase pattern in (b), however with a longer defect. Scale bar is 5.65 microns
as measured by atomic force microscope

# LIST OF ACRONYMS

1D – one dimension(al)
2D – two dimension(al)
3D – three dimension(al)
AFM – Atomic force microscope
BE – Beam expander
BZ – Brillouin zone
CCD – Charge coupled device
CMOS – Complementary metal-oxide semiconductor
CVD – Chemical vapor deposition
CW – Continuous wave
DLW – Direct laser write
DMD – Digital micromirror device
DOE – Diffractive optical element
DPHPA – Dipentaerythritol penta/hexa-acrylate
EBL – Electron beam lithography
EM – Electromagnetic
FF – Fourier filter
FT – Fourier transform
GPU – Graphics processing unit
IBZ – Irreducible Brillouin zone
LC – Liquid crystal

LCoS – Liquid crystal on silicon

LUT – Look up table

MO – Microscope objective

NPG - N-phenyl glycine

NVP - N-vinyl pyrrolidinone

PAN – Parallel-aligned nematic

PDMS – Polydimethylsiloxane

PhC – Photonic crystal

ROE – Reflective optical element

SEM – Scanning electron microscope

SLM – Spatial light modulator

TCP - Top-cut prism

TE – Transverse electric

TEA - Triethylamine

TM – Transverse magnetic

USB - Universal serial bus

UV - Ultraviolet

#### CHAPTER 1

#### INTRODUCTION

#### 1.1 Motivation

Electronic microprocessor power has been increased by both increasing the number of transistors on a single processing unit and reducing the feature size of circuits. This method is approaching physical limits, due to bandwidth, heat, and quantum tunneling between wires on the chip. [1-3] Photonic, or light-based, devices combined with electronic integrated circuits may provide a solution to these problems. With a vastly higher data transfer rate and passive components which do not generate heat, photonic devices can provide the technology to continue increasing computing power past the limits of today's electronic integrated circuits. To utilize light as a method of data transfer, materials and devices are needed which can manipulate the flow of light, as in a circuit; photonic crystals have this capability.

Photonic crystals are periodic dielectric structures that can be used for manipulation and steering of light. This is accomplished via a photonic band gap, [4-6] which prevents electromagnetic wave propagation, either in certain directions or in all directions, depending on the structure. The photonic band gap for photonic crystals is analogous to electronic band gap in semiconductors. In semiconductor crystals, atoms create a periodic potential that the electrons can move through, and the electronic energy bands may have gaps that prevent propagation of electrons with certain energies in certain directions. A periodic distribution of dielectric material functions for photonic crystals as atoms do for electronic crystals. Analogous to impurities in silicon, engineered defects in photonic crystals can not only fundamentally change photonic crystal properties, but also offer new possibilities for designing functional

devices. Optical waveguides can be fabricated by adding linear defects to photonic crystals, making photonic circuits possible. [6] Just as with electronic crystals, photonic crystals can be used in the future as photonic chips for the integration of optical circuits. [7-8]

Photonic crystals have been the subject of intense research for the past two decades. Since then, many applications have been found for them. Engineered defects in photonic crystal can create optical waveguides, even with sharp bends with relatively low losses, [9-12] as well as resonant cavities that can be used for lasing, splitting, or filtering. [12-23] Photonic crystals have also led to the realization of negative refractive index metamaterials [24-33] and superlensing [29-31]. By controlling the variance of the filling fraction of a photonic crystal, gradient refractive index photonic crystal lenses are possible, as well as couplers for photonic crystal waveguides. [34-38] One of the more exotic applications of photonic crystals has led to the potential use of them to cloak small objects, that is, hide them beneath a photonic crystal with an engineered structure. [39-41]

For all the applications and research that has been conducted, novel methods of fabricating photonic crystals are still being studied. While many methods exist, rapid patterning of large areas of photonic crystals has been best accomplished by the use of holographic interference lithography. [42] Conventional interference lithography setups use many bulk optical elements, such as lenses, mirrors, beam splitters, etc. Reduction of the complexity of the optical setup is vital to reducing the mechanical instability of the optical setup, reducing error in the final fabricated structures, and also vital in reducing cost should holographic lithography be used for large-scale fabrication of photonic structures in industry. The focus of this dissertation is in the development of photonic crystal fabrication methods that are capable of local

manipulation of the phase of interfering beams for the fabrication of two- and three-dimensional photonic crystal templates. Through study of local control of the phases of the beams, we can create photonic crystal structures with embedded, engineered defects. These studies mark a step toward a fast, single step approach for holographic fabrication of photonic circuits embedded in photonic crystals (PhCs).

## 1.2 Outline of Dissertation

Chapter 1 introduces the topic of this dissertation. The motivation for the research performed is discussed to establish the significance and the reason for carrying out the experiments. The rest of the dissertation is outlined briefly, and the direction of the research is laid out and described.

Chapter 2 starts from Maxwell's equations to derive the wave equation. From there, crystal lattices and reciprocal lattices, as well as the concept of Brillouin zones are described before moving onto photonic crystals. The principles of photonic crystals and the photonic band gap are explained. Finally, principles of defects in photonic crystals are described.

Chapter 3 covers the methods of fabricating photonic crystals with a focus on holographic lithography. Interference of multiple beams is discussed to explain the formation of the various interference patterns needed for holographic fabrication of photonic crystals. Effects of the number of beams, the interference angle, as well as the amplitudes, polarizations, and phases of the beams on the structure of the interference patterns are discussed. Different holographic methods are explained and the methods chosen for this research are described.

Chapter 4 covers spatial light modulators, and concepts related to them are discussed in relation to their use in holographic lithography. Diffraction from periodic structures is also

covered, as the spatial light modulator is used as a diffractive optical element (DOE). Fourier transformations by lenses, filtering, and the 4f imaging system are described. Recent work in the field is described.

Chapter 5 begins the chapters that describe the results from our research. Here, the fabrication of photonic crystal templates by holographic lithography using a silicon-based reflective optical element. The construction of the ROE is described. The ROE is made to generate the requisite number of beams and the polarizations of the beams for a desired structure. Using the ROE, woodpile-type photonic crystal templates are fabricated in thin-film photoresist.

Chapter 6 describes our initial use of geometric phase patterns displayed on a spatial light modulator to generate diffracted beams from the spatial light modulator for the holographic fabrication of photonic crystal templates in thin-film photoresist. The ability of these phase patterns to control the phases of the diffracted beams is explored, and the fabricated compound photonic crystal templates are described.

Chapter 7 explores a method for the mathematically formulated phase engineering of interfering laser beams through a spatial light modulator for a holographic fabrication of graded photonic lattices. The desired phases can be programmed at specific locations by assigning gray levels in cellular structures. Single-lattice structures or missing lattices were embedded in dual-lattice periodic photonic structures as a way of demonstrating the validity of the method.

Chapter 8 presents simple gradient refractive index in bi-continuous holographic structures that are formed through five-beam interference. A theoretical approach for the realization of gradient index devices by engineering the phases of the interfering beams with a

pixelated spatial light modulator is described. The five beams with desired phases were generated through programming gray level super-cells in a diffractive spatial light modulator. As a proof-of-concept, gradient index structures were demonstrated using synthesized and gradient phase patterns displayed on the spatial light modulator.

Chapter 9 describes two methods for registering desired defect lattices within background periodic lattices using SLM-based holographic lithography. In the firs method, the diffraction efficiency from the engineered phase pattern was used to locally modify the fill fraction of polymerized materials in holographic structures, and at the same time, achieved the lattice matching between modified and background regions. In the second method, spatially variant lattices with a 90° bend were registered within background periodic lattices through two-step phase engineering of the laser beam.

Chapter 10 describes the holographic fabrication of designed defect lines in photonic crystal lattices through phase engineering using a SLM. The diffracted beams from the SLM not only carry the defect's content but also the defect related phase-shifting information. It is shown that the phase-shifting-induced lattice shifting in photonic lattices around the defects in a three-beam interference is less than the one produced by a five-beam interference due to the alternating shifting in lattice in a three beam interference. By designing the defect line at a 45 degree orientation and using three-beam interference, the defect orientation was aligned with the background photonic lattice, and the shifting was only in one side of the defect line, in agreement with the theory. Finally, a new design for the integration of functional defect lines in a background phase pattern reduces the relative phase shift of the defect and utilizes the different diffraction efficiency between the defect line and background phase pattern. It is

demonstrated that the desired and functional defect lattice can be registered into the background lattice through the direct imaging of designed phase patterns.

Chapter 11 concludes the dissertation with a summary of the results of the research performed.

#### CHAPTER 2

#### FUNDAMENTALS OF PHOTONIC CRYSTALS

Since photonic crystals are structures designed to manipulate electromagnetic fields, they are governed by the laws of electricity and magnetism. Thus, an understanding of Maxwell's equations, which describe these fields, is essential to the study of how electromagnetic waves propagate in photonic crystals.

## 2.1 Maxwell's Equations to the Wave Equation

Maxwell's equations in matter in time-domain differential form are given by

$$\nabla \cdot \boldsymbol{D}(\boldsymbol{r},t) = \rho \tag{2.1}$$

$$\nabla \cdot \boldsymbol{B}(\boldsymbol{r},t) = 0 \tag{2.2}$$

$$\nabla \times \mathbf{E}(\mathbf{r}, t) + \frac{\partial \mathbf{B}(\mathbf{r}, t)}{\partial t} = 0$$
 (2.3)

$$\nabla \times \boldsymbol{H}(\boldsymbol{r},t) - \frac{\partial \boldsymbol{D}(\boldsymbol{r},t)}{\partial t} = \boldsymbol{J}(\boldsymbol{r},t)$$
 (2.4)

where D is the displacement field,  $\rho$  is the free charge density, B is the magnetic induction field, E is the electric field, H is the magnetic field, and J is the current density. We consider a medium in which there are no sources of charge and no current flowing in the medium ( $\rho$ =0, J=0). It is also assumed that the medium is dielectric, lossless, and that the dielectric function,  $\epsilon$ (r), is real and positive. With these considerations in mind, the relationships between E and D, and B and H, can be written as

$$\mathbf{D}(\mathbf{r},t) = \varepsilon_0 \varepsilon(\mathbf{r}) \mathbf{E}(\mathbf{r},t) \tag{2.5}$$

$$\mathbf{B}(\mathbf{r},t) = \mu_0 \mathbf{H}(\mathbf{r},t) \tag{2.6}$$

where  $\varepsilon_0$  is the permittivity of free space,  $\varepsilon(r)$  is the dielectric constant, and  $\mu_0$  is the permeability of free space. There is a relative permeability factor in Eq. (2.6), but in most materials, this is effectively 1, so it is not shown. Substituting Eqs. (2.5) & (2.6) into Eqs. (2.1)-(2.4), and applying the assumptions of no sources and a lossless, isotropic dielectric with a real and positive dielectric function, Maxwell's equations become

$$\nabla \cdot \varepsilon(\mathbf{r})\mathbf{E}(\mathbf{r},t) = 0 \tag{2.7}$$

$$\nabla \cdot \boldsymbol{H}(\boldsymbol{r},t) = 0 \tag{2.8}$$

$$\nabla \times \mathbf{E}(\mathbf{r}, t) + \mu_0 \frac{\partial \mathbf{H}(\mathbf{r}, t)}{\partial t} = 0$$
 (2.9)

$$\nabla \times \boldsymbol{H}(\boldsymbol{r},t) - \varepsilon_0 \varepsilon(\boldsymbol{r}) \frac{\partial \boldsymbol{E}(\boldsymbol{r},t)}{\partial t} = 0$$
 (2.10)

Exploiting the linearity of Maxwell's equations and assuming that the field pattern changes harmonically with time, the spatial and time dependence can be separated and the equations for the electric and magnetic fields can be written as

$$E(r,t) = E(r)e^{-i\omega t}$$
 (2.11)

$$H(r,t) = H(r)e^{-i\omega t}$$
 (2.12)

Substituting Eqs. (2.11)-(2.12) into Eqs. (2.7)-(2.10) for the electric and magnetic fields, Maxwell's equations give

$$\nabla \times \mathbf{E}(\mathbf{r}) - i\omega \mu_0 \mathbf{H}(\mathbf{r}) = 0 \tag{2.13}$$

$$\nabla \times \mathbf{H}(\mathbf{r}) + i\omega \varepsilon_0 \varepsilon(\mathbf{r}) \mathbf{E}(\mathbf{r}) = 0 \tag{2.14}$$

Since the substitution of Eq. (2.11)-(2.12) into Eqs. (2.7)-(2.8) returns identical equations reiterating the condition of no sources or sinks, we forgo rewriting them. Rearranging Eq. (2.14)

as

$$\frac{1}{\varepsilon(\mathbf{r})}\nabla \times \mathbf{H}(\mathbf{r}) = -i\omega\varepsilon_0 \mathbf{E}(\mathbf{r}) \tag{2.15}$$

and taking the curl of both sides gives

$$\nabla \times \left[ \frac{1}{\varepsilon(\mathbf{r})} \nabla \times \mathbf{H}(\mathbf{r}) \right] = -i\omega \varepsilon_0 \nabla \times \mathbf{E}(\mathbf{r})$$
 (2.16)

By substituting Eq. (2.13) into Eq. (2.16) and utilizing the relationship,  $\varepsilon_0\mu_0=c^{-2}$ , where c is the speed of light, a frequency domain, vector wave equation presents itself.

$$\nabla \times \left[ \frac{1}{\varepsilon(r)} \nabla \times H(r) \right] = \left( \frac{\omega}{c} \right)^2 H(r)$$
 (2.17)

Eq. (2.17) can be written as

$$\Theta_H \mathbf{H}(\mathbf{r}) = \left(\frac{\omega}{c}\right)^2 \mathbf{H}(\mathbf{r}) \tag{2.18}$$

This is an eigenvalue problem with eigenvalues  $\left(\frac{\omega}{c}\right)^2$ , eigenfunctions (or eigenmodes) H(r), and an operator defined as  $\Theta_H \triangleq \nabla \times \left[\frac{1}{\varepsilon(r)}\nabla \times\right]$ . The operator is linear and Hermitian [6]. For a photonic crystal structure defined by a dielectric function  $\varepsilon(r)$ , the eigenvalue equation can be solved to find the eigenvalues and the eigenmodes.

#### 2.2 Scale Invariance

In practice, fabricating photonic crystals on the nanoscale can be difficult. However, Maxwell's equations and Eq. (2.17) have the benefit of being scale invariant. That is, there is no fundamental length scale. This means that systems that differ by a scaling factor behave the same, except that the eigenfrequencies and eigenmodes are scaled accordingly. This is important because photonic crystals made at a larger scale (for example, in the microwave or infrared regime) behave the same as a nanoscale photonic crystal intended for use in the visible range of the spectrum. To demonstrate this, let us start with Eq. (2.17), and scale the

dimensions of the dielectric function,  $\epsilon(r)$ , up or down by a multiplicative scaling constant, s, such that the vector wave equation, Eq. (2.17), in this scaled system is

$$s\nabla \times \left[\frac{1}{\varepsilon(\mathbf{r}/s)}s\nabla \times \mathbf{H}(\mathbf{r}/s)\right] = \left(\frac{\omega}{c}\right)^2 \mathbf{H}(\mathbf{r}/s)$$
 (2.19)

By dividing both sides by the scaling factors, s^2, we obtain

$$\nabla \times \left[ \frac{1}{\varepsilon(\mathbf{r}/s)} \nabla \times \mathbf{H}(\mathbf{r}/s) \right] = \left( \frac{\omega}{s} \right)^2 \left( \frac{1}{c} \right)^2 \mathbf{H}(\mathbf{r}/s)$$
 (2.20)

This is the same vector wave equation as Eq. (2.17), just with a dielectric function,  $\epsilon'(\mathbf{r}) = \epsilon(\mathbf{r}/s)$  and magnetic field,  $\mathbf{H}'(\mathbf{r}) = \mathbf{H}(\mathbf{r}/s)$ , scaled by the factor, s, and frequencies,  $\omega' = \omega/s$ . To better show that the equations are the same, save for the scaling factor, Eq. (2.20) can be rewritten as

$$\nabla \times \left[ \frac{1}{\varepsilon'(\mathbf{r})} \nabla \times \mathbf{H}'(\mathbf{r}) \right] = \left( \frac{\omega'}{c} \right)^2 \mathbf{H}'(\mathbf{r})$$
 (2.21)

This feature of Maxwell's equations also applies to scaling of the index of refraction. If the index of refraction (and consequently, the relative permittivity) is scaled by a constant, such as in the case that a material change is made (where, again, the assumption is made that the relative permeability is close to unity),

$$\frac{n}{s} = \sqrt{\varepsilon(\mathbf{r})} \iff n = \sqrt{s^2 \varepsilon(\mathbf{r})}$$
 (2.22)

Plugging the scaled dielectric function into the wave equation and multiplying both sides by the material scaling factor s^2 gives

$$\nabla \times \left[ \frac{1}{\varepsilon(\mathbf{r})} \nabla \times \mathbf{H}(\mathbf{r}) \right] = \left( \frac{\omega}{s} \right)^2 \left( \frac{1}{c} \right)^2 \mathbf{H}(\mathbf{r}) = \left( \frac{\omega'}{c} \right)^2 \mathbf{H}(\mathbf{r})$$
 (2.23)

In this case, the fields,  $\mathbf{H}(\mathbf{r})$ , do not change, but the frequency response of the system does, with the new frequencies,  $\omega' = \omega/s$ . This is another important feature, since photonic crystals are usually fabricated in a type of photoresist, and the photoresist is later replaced with a higher refractive index material. Since the frequencies scale linearly, the behavior of the system after the replacement of the photoresist material can be predicted. This will be discussed more in the next chapter.

## 2.3 Photonic Crystal Lattices

Since photonic crystals are periodic dielectric structures, describing their structures in terms of lattice symmetries and solid state physics provides an effective framework for defining the dielectric function in Eq. (2.17), which allows the eigenvalue problem to be solved. Crystals, in general, and including photonic crystals, are defined by a lattice and a basis. In electronic crystals, a basis is a group of atoms that can be repeated throughout space to construct a crystal. In photonic crystals, a structure made of macroscopic dielectric media makes up the basis. The lattice is the one, two, or three-dimensional repetition of points in space on which the basis is repeated. In three dimensions, the lattice is defined by primitive translation vectors (e.g.  $a_1, a_2, a_3$ ).

In general, lattices are classified based on the symmetry of the arrangement of the points in the lattice. Symmetry operations, such as rotation, reflection, or inversion, can be performed on the lattice. If after a symmetry operation, the lattice appears unchanged, it can be classified according to the conditions that the symmetry imposes. Lattices can be classified into 5 distinct lattice types in two dimensions and 14 lattice types in 3 dimensions. These special lattices types are known as the Bravais lattices. The five 2D Bravais lattices are shown in

Figure 2.1. The most general type of 2D lattice is the oblique lattice shown in the upper left corner of Figure 2.1. It is only invariant under a rotation of  $2\pi$  and  $\pi$ , with no conditions on the lattice vectors. The other types of 2D Bravais lattices are the square, hexagonal, rectangular, and centered rectangular lattices, all shown in Figure 2.1, with the conditions required for the construction of those lattices.

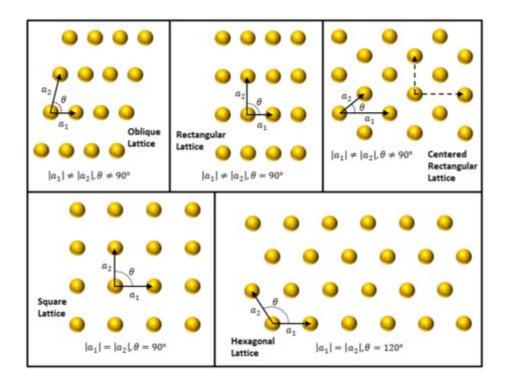


Figure 2.1. The five Bravais lattices in two dimensions.

Figure 2.2 shows five of the 14 Bravais lattice types in three-dimensions, which are classified into seven groups. [43] The triclinic lattice is the most general lattice, with no symmetry and no conditions imposed upon the lattice vectors. It should be mentioned that there are lattice types that are not classified into a category of Bravais lattice. For example, quasicrystals exist that have rotational symmetry, but no translational symmetry. [44-45] Also, lattices with dual or triple motif structures can be fabricated that have interesting properties. [46-47]

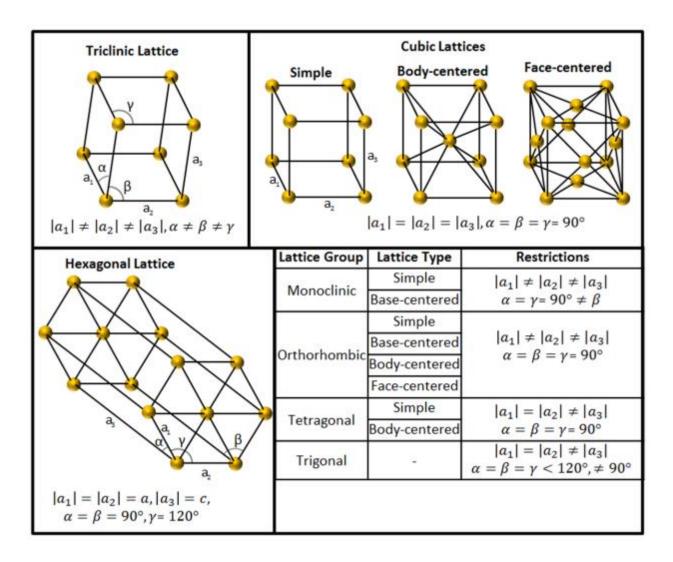


Figure 2.2 Five of the 14 Bravais lattices in 3 dimensions, organized into 7 groups. Table in lower right lists lattices not shown.

For photonic crystal lattices, the dielectric structure is periodic in 1, 2, or 3 dimensions, and invariant under translation defined by

$$\mathbf{r} = m_1 \mathbf{a}_1 + m_2 \mathbf{a}_2 + m_3 \mathbf{a}_3 \tag{2.24}$$

where  $m_i$  are integers, and  $a_i$  are the primitive translation vectors, or simply lattice vectors. The lattice vectors span the crystal lattice in physical space, known as the direct lattice. Any lattice

point in the crystal structure can be defined by Eq. (2.24). For example, at a point,  ${\bf r}'$ , with a translation defined by

$$\mathbf{r}' = \mathbf{r} + v_1 \mathbf{a}_1 + v_2 \mathbf{a}_2 + v_3 \mathbf{a}_3, \tag{2.25}$$

the dielectric structure is identical to a point  $\mathbf{r}$ . For a photonic crystal, Eq. (2.25) imposes a periodic condition on the position dependent dielectric function,

$$\varepsilon(\mathbf{r}) = \varepsilon(\mathbf{r} + \mathbf{T}) \tag{2.26}$$

where T is a translation vector given by

$$\mathbf{T} = m_1 \mathbf{a}_1 + m_2 \mathbf{a}_2 + m_3 \mathbf{a}_3 \tag{2.27}$$

such that the photonic crystal is invariant after the translation operation. From this periodic condition, the dielectric function,  $\epsilon(r)$ , can be expanded in a Fourier series, i.e. taking the Fourier transform of  $\epsilon(r)$  or building  $\epsilon(r)$  out of plane waves,

$$\varepsilon(\mathbf{r}) = \sum_{G} \varepsilon_{G} \exp(i\mathbf{G} \cdot \mathbf{r})$$
 (2.28)

where

$$\varepsilon_{\rm G} = V_c^{-1} \int dV \, \varepsilon(\mathbf{r}) \exp(-i\mathbf{G} \cdot \mathbf{r})$$
 (2.29)

and

$$\mathbf{G} = v_1 \mathbf{b}_1 + v_2 \mathbf{b}_2 + v_3 \mathbf{b}_3 \tag{2.30}$$

 $V_c$  is the volume of the unit cell.  $\varepsilon_G$  is the coefficient of the Fourier expansion, and G is a set of vectors in the reciprocal lattice. Applying the periodic condition in Eq. (2.26) gives us

$$\varepsilon(\mathbf{r}) = \sum_{G} \varepsilon_{G} \exp(i\mathbf{G} \cdot \mathbf{r}) = \sum_{G} \varepsilon_{G} \exp[i\mathbf{G} \cdot (\mathbf{r} + \mathbf{T})] = \varepsilon(\mathbf{r} + \mathbf{T})$$
(2.31)

By distributing the dot product of G through the parentheses on the right,

$$\sum_{G} \varepsilon_{G} \exp(i\mathbf{G} \cdot \mathbf{r}) = \sum_{G} \varepsilon_{G} \exp(i\mathbf{G} \cdot \mathbf{r}) \exp[i\mathbf{G} \cdot \mathbf{T}]$$
(2.32)

For the periodic condition to hold true,

$$\varepsilon_{G} = \varepsilon_{G} \exp(i\mathbf{G} \cdot \mathbf{T}) \tag{2.33}$$

and either  $\varepsilon_G = 0$ , or  $\exp(i\mathbf{G} \cdot \mathbf{T}) = 1$ . Utilizing the fact that  $\exp i(2\pi)N = 1$ , where N is an integer value, we come to the condition,

$$\mathbf{G} \cdot \mathbf{T} = (v_1 \mathbf{b}_1 + v_2 \mathbf{b}_2 + v_3 \mathbf{b}_3) \cdot (m_1 \mathbf{a}_1 + m_2 \mathbf{a}_2 + m_3 \mathbf{a}_3) = 2\pi N \tag{2.34}$$

If  $v_i$  and  $m_i$  are integer values, then for Eq. (2.34), and consequently, for the periodic condition in Eq. (2.26), to be true, then the following relation between the primitive lattice translation vectors,  $\boldsymbol{a}_i$ , and the primitive reciprocal lattice vectors,  $\boldsymbol{b}_i$ , must also be true

$$\boldsymbol{a}_i \cdot \boldsymbol{b}_i = \delta_{ij} \tag{2.35}$$

where  $\delta_{ij}=2\pi$  if i=j and zero otherwise. This relation can be used to define the reciprocal lattice vectors in terms of the lattice translation vectors,

$$b_1 = 2\pi \frac{a_2 \times a_3}{a_1 \cdot (a_2 \times a_3)} \qquad b_2 = 2\pi \frac{a_3 \times a_1}{a_1 \cdot (a_2 \times a_3)} \qquad b_3 = 2\pi \frac{a_1 \times a_2}{a_1 \cdot (a_2 \times a_3)}$$
(2.36)

These reciprocal lattice vectors span the reciprocal lattice, and are associated with each point in the crystal, as the direct lattice is. The direct lattice has units of length and the reciprocal lattice has units of  $2\pi$ /length. The reciprocal lattice exists in Fourier space, or k-space, just as wave vectors do. With wave vectors associated with electromagnetic wave propagation are defined in k-space, it is useful to define photonic crystals using a lattice that is also defined in the same way.

### 2.4 Unit Cells and Brillouin Zones

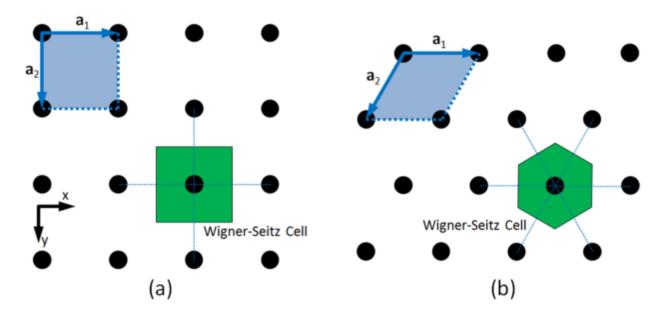


Figure 2.3(a) Square lattice and (b) hexagonal lattice with lattice vectors, primitive cells, and Wigner-Seitz cells specified.

While the crystal lattice can be constructed through translations defined by Eq. (2.24), that equation merely defines the location of the lattice points. A unit cell is needed to fully construct the photonic crystal. The unit cell with the least volume required to fill all of space is repeated at each lattice point with no overlap between cells. Each unit cell will only have one lattice point within it, and the shape of the unit cell is highly dependent on the symmetry of the crystal. The unit cell can be the primitive cell defined by the lattice translation vectors, as seen in the two-dimensional examples in Figure 2.3 above.

Figure 2.3 shows a square lattice with lattice vectors shown in the top left, labeled a1 and a2. The dotted lines extending from the ends of the lattice vectors complete a square unit cell with area a^2. Another type of unit cell is called the Wigner-Seitz cell. It is found by drawing lines to the nearest neighboring lattice points, drawing bisector lines (or planes, in 3D)

normal to the first set of lines. The smallest area (or volume, in 3D) enclosed by the bisector lines (planes in 3D) is the Wigner-Seitz cell, represented by the green square in the square lattice in Figure 2.3(a). A similar comparison is shown in Figure 2.3(b) for a 2D hexagonal lattice. In the hexagonal lattice, the primitive cell is a parallelogram with side lengths equal to the lattice spacing, whereas the Wigner-Seitz cell is a hexagon that is rotated 90°. Here, 2D examples were given, but the process applies just as well in three-dimensions, where the Wigner-Seitz cells are polyhedrons. As an example, the Wigner-Seitz cells for three different cubic lattices are shown in Figure 2.4.

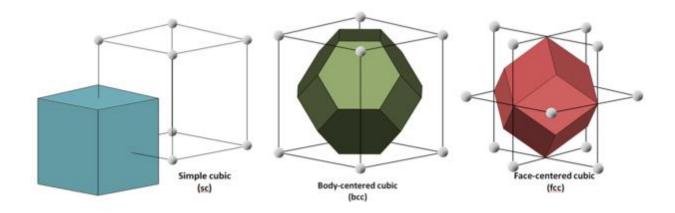


Figure 2.4. Wigner-Seitz cells for simple cubic, body-centered cubic, and face-centered cubic lattices.

While unit cells can be defined in the crystal lattice, it is the unit cells of the reciprocal lattice that are most useful in describing the propagation of light in a photonic crystal. In the reciprocal space, the Wigner-Seitz unit cell is called the Brillouin zone (or more specifically, the first Brillouin zone). It is constructed in the exact same way as the Wigner-Seitz cell in the direct lattice. Examples of Brillouin zones in 2D square and hexagonal reciprocal lattices are shown in Figure 2.5 below.

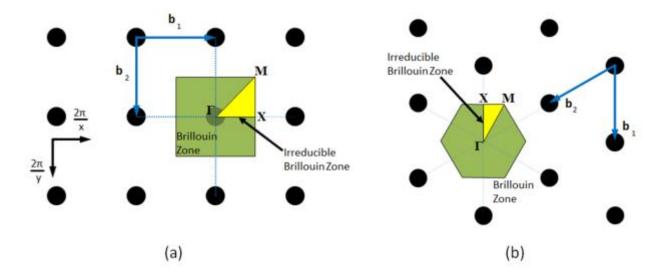


Figure 2.5. First and Irreducible Brillouin zones for reciprocal (a) square and (b) hexagonal lattices.

Due to symmetry, many points in the Brillouin zone are redundant. The Brillouin zone can be reduced to a non-redundant set of points that are not related by symmetry. This non-redundant set of points is called the irreducible Brillouin zone (IBZ), and is indicated in Figure 2.5 by a yellow, shaded, triangular area. There are special symmetry points on the IBZ that are labeled in the figure. Γ (gamma) is set to the origin at the center of the Brillouin zone, X indicates the center of a facet of the Brillouin zone, and M marks the center of the line where two facets meet. IBZs in 2D are simple to illustrate, but in three dimensions, the IBZ can have a complicated shape, depending on the lattice chosen. In Figure 2.6, the Brillouin zone for an FCC lattice, which has a BCC reciprocal lattice, (the BCC lattice has a FCC reciprocal lattice, as well) is shown. A complete listing of Brillouin zones and the irreducible Brillouin zones can be seen in the appendix of Setyawan and Curtarolo [48].

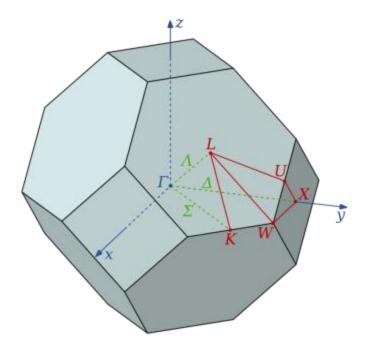


Figure 2.6. Brillouin zone of fcc lattice with irreducible Brillouin zone shown. Image from Wikimedia Commons.

# 2.5 Photonic Bands and the Band Gap

The discrete periodic structure of photonic crystals leads to discrete solutions to the eigenvalue equation in Eq. (2.18). Using Bloch theorem, solutions to the eigenvalue problem take the form of

$$\mathbf{H}_{k}(\mathbf{r}) = \mathbf{u}_{k}(\mathbf{r}) \exp(i\mathbf{k} \cdot \mathbf{r}) \tag{2.37}$$

where k is a wavevector of the form,

$$\mathbf{k} = v_1 \mathbf{b}_1 + v_2 \mathbf{b}_2 + v_3 \mathbf{b}_3 \tag{2.38}$$

with  $b_i$  being the reciprocal lattice vectors of the crystal, and  $u_k(\mathbf{r})$  is a periodic envelope function satisfying the periodic boundary condition. Because  $u_k(\mathbf{r})$  satisfies the periodic condition, it has the same symmetry as the photonic crystal lattice. The magnetic field modes and the envelope function are indexed according to the k-vector. The wavevectors are chosen

in reciprocal lattice coordinates to identify corresponding locations in the Brillouin zone of the photonic crystal. By inserting the Bloch state,  $\mathbf{H}_k(\mathbf{r})$ , into Eq. (2.18), we obtain

$$\nabla \times \left[ \frac{1}{\varepsilon(\mathbf{r})} \nabla \times \mathbf{u}_{k}(\mathbf{r}) \exp(i\mathbf{k} \cdot \mathbf{r}) \right] = \left( \frac{\omega(\mathbf{k})}{c} \right)^{2} \mathbf{u}_{k}(\mathbf{r}) \exp(i\mathbf{k} \cdot \mathbf{r})$$
(2.39)

Here, the frequency eigenvalues and the magnetic field eigenmodes are dependent upon the wavevector chosen. Applying the product rule,  $\nabla \times (f\mathbf{A}) = f(\nabla \times \mathbf{A}) - \mathbf{A} \times (\nabla f)$ , twice to Eq. (2.39), and dividing through by the exponential terms on both sides, we find

$$(i\mathbf{k} + \nabla) \times \frac{1}{\varepsilon(\mathbf{r})} (i\mathbf{k} + \nabla) \times \mathbf{u}_{\mathbf{k}}(\mathbf{r}) = \left(\frac{\omega(\mathbf{k})}{c}\right)^2 \mathbf{u}_{\mathbf{k}}(\mathbf{r})$$
 (2.40)

This equation can be solved numerically for a photonic crystal structure specified by a dielectric function,  $\epsilon(\mathbf{r})$ , to find the set of discrete frequency functions,  $\omega_n(\mathbf{k})$ , where n is the band number, and k is a wavevector within the Brillouin zone.  $\omega_n(\mathbf{k})$  are continuous functions of k. Plotting k vs  $\omega_n(\mathbf{k})$  gives the dispersion relation, or the photonic band structure, as it is also known. From the photonic band diagram, the allowed directions of propagation of EM waves with frequencies specified by the photonic bands can be determined.

To reduce the amount of redundant calculations, the band structure is calculated only for critical symmetry points (and points interpolated between them) within the irreducible Brillouin zone, as all other locations within the entire Brillouin zone are related to the IBZ by the symmetry relations and the periodic nature of the lattice. Generally, the band structure is not solved for analytically. Numerical methods such as finite-difference time domain (FDTD) or plane wave expansion (PWE) are used to find the band structure. For example, the MIT Photonic Bands (MPB) application uses PWE in the frequency domain to calculate the dispersion relations for specified photonic structures. [49]

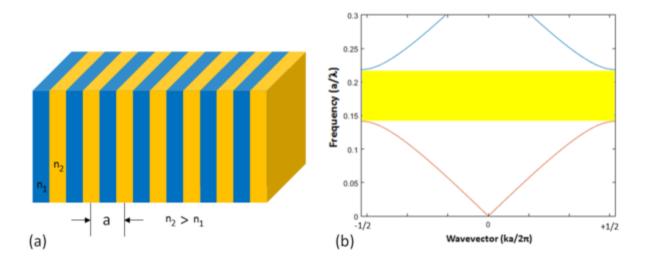


Figure 2.7. (a) diagram of a 1D photonic crystal (dielectric stack). (b) Dispersion relation (band diagram) for the structure in (a). Bandgap highlighted in yellow.

Figure 2.7(a) shows a diagram of a 1D photonic crystal made from alternating dielectric layers, and the band diagram for the structure is shown in Figure 2.7(b). The period of the 1D lattice is a, and the period of the reciprocal lattice is  $2\pi/a$ , placing the boundaries of the Brillouin zone at  $\pm\pi/a$ . The frequencies,  $\omega_n(\mathbf{k})$ , are calculated for k values along the direction of periodicity, in this case, the z-axis. Modes with k=+ $\pi/a$  or k=- $\pi/a$  are related by a reciprocal lattice translation equal to the size of the Brillouin zone, so the bands are folded back into the Brillouin zone from the edges. There is a gap between the lowest, or first, band, and the higher second band. To understand the origin of the gap, consider two electric field modes at the edge of the Brillouin zone, where k=  $\pi/a$ . As mentioned earlier, the field modes take on the same symmetry as the lattice. To see how the field will be distributed, we look to the variational principle, which is used to calculate the bands. The lowest band is found from the field with the lowest frequency,  $\omega_0$ , that minimizes the variational energy functional, given by

$$E_{v} \triangleq \frac{\left(\mathbf{H}, \widehat{\Theta}\mathbf{H}\right)}{\left(\mathbf{H}, \mathbf{H}\right)} \tag{2.41}$$

Manipulating this equation using Eqs. (2.13),(2.14),and (2.18), Eq. (2.41) becomes

$$E_{v} \triangleq \frac{\int d^{3} \mathbf{r} |\nabla \times \mathbf{E}(\mathbf{r})|^{2}}{\int d^{3} \mathbf{r} \, \varepsilon(\mathbf{r}) |\mathbf{E}(\mathbf{r})|^{2}}$$
(2.42)

From Eq. (2.42), it can be seen that in order to minimize the variational energy, the denominator must be maximized. This is accomplished by concentrating the electric field inside areas of high refractive index. Since the 1D crystal in Fig. 2.something is made from two dielectric materials, the energy of the electric field in the lowest band is concentrated in the higher index material (in the diagram, n2>n1). The modes of the next band will be orthogonal to the ones in the lowest band; the modes of the third band will be orthogonal to the second, etc. Since the modes of the band above the gap must have the same symmetry as the previous band, and are orthogonal to the band below the gap, the energy of the modes of the higher band will transfer into the lower index regions of the 1D photonic crystal. This concept is transferrable to 2D and 3D lattices. [6]

Photonic band gaps arise when there are no bands (that is, no  $\omega_n$  for a set of wavevectors) in a range of frequencies. Electromagnetic waves with frequencies in the bandgap are forbidden to propagate within the photonic crystal. A partial bandgap occurs when propagation of EM waves is forbidden only in a certain set of directions, or in a single polarization. A complete band gap forbids EM wave propagation for all frequencies within the bandgap from all directions and of any polarization. Since the width of the bandgap in terms of absolute  $\omega$  will change according to the period of the lattice, the standard gage of the size of the bandgap is presented in terms of the gap-midgap ratio,

$$gap - midgap ratio = \frac{\Delta \omega}{\omega_m}$$
 (2.43)

where  $\Delta\omega$  is the frequency width of the bandgap, and  $\omega_m$  is the middle frequency in the gap. The photonic bandgap can be altered by selecting the symmetry of the lattice, and optimizing the filling fraction and the refractive index contrast for maximization of the bandgap. Generally, a high refractive index contrast between the materials making up a photonic crystal is needed to maximize the bandgap. [6]

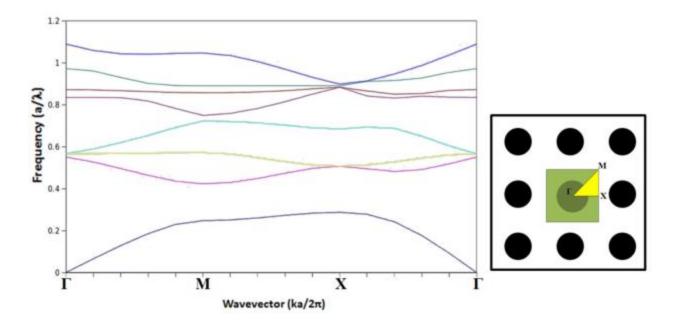


Figure 2.8. Band diagram for 2D square lattice of dielectric cylindrical rods in air, a schema of which is shown in the right side of the figure.

In two-dimensional photonic crystals, propagation of electromagnetic waves is restricted to the plane of periodicity of the crystal. Electromagnetic modes in 2D photonic crystals are classified according to polarization as either transverse-electric (TE), where the electric field is in the crystal plane and the magnetic field is normal to the plane, or transverse magnetic (TM), where the magnetic field is in the plane and the electric field is normal. 2D

photonic crystals with a periodic structure of isolated high refractive index regions will favor a bandgap in the TM polarization, as seen in Figure 2.8. Here, the first few photonic bands for a square lattice of dielectric cylindrical rods are shown. In the insets, diagrams of the crystal and of the reciprocal lattice with the IBZ overlaid upon it are shown. The band diagram was calculated along the perimeter of the IBZ (from  $\Gamma$  to X to M, then back to  $\Gamma$ ) using MIT Photonic Bands software. As seen in the photonic band structure in Figure 2.8, the TM modes have a bandgap between the first and second bands. In contrast to this example, a periodic array of air holes in high index dielectric will favor a bandgap in the TE polarization, but not in the TM polarization. To have a complete photonic bandgap in a 2D photonic crystal, with a bandgap appearing in both the TE and TM polarizations, a photonic crystal with isolated and connected high index regions must be made. [6] A honeycomb-type structure made of a triangular lattice of air holes in dielectric provides a balance between the isolated and interconnected regions that allows a complete photonic bandgap for all polarizations and directions [50]. While the triangular lattice of air holes in dielectric provides a complete photonic band gap, other parameters besides the choice of lattice are often needed to be taken into account, such as the refractive index contrast, size of the rods/holes in comparison to the size of the unit cell (filling fraction), and the shape and orientation of the rods/holes.[51] By reducing the symmetry by adding a second rod/hole to the basis, the band gap can be made even larger. [52-53]

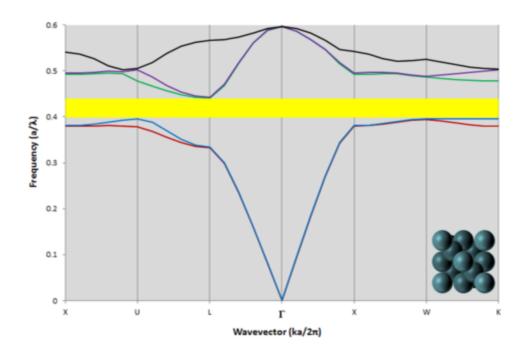


Figure 2.9. Band diagram of diamond lattice of air spheres in dielectric. Inset shows arrangement of spheres in lattice.

In 3D photonic crystals, the variety of structures possible is limitless. But in three dimensions, interconnected structures are necessary not just for bandgap generation, as in the two-dimensional case, but also for structural stability. The diamond lattice has proven to be an effective means of achieving complete bandgaps in three-dimensions, due to the near spherical shape of the Brillouin zone. [54] In Figure 2.9, a band diagram for a diamond lattice of air spheres in dielectric is shown. There is a complete band gap between the second and third bands of with a gap-midgap ratio of 10.7%. Other photonic crystals with the diamond lattice include Yabolonovite and the woodpile structure. [55-56] Figure 2.10 shows an idealized diagram and an example of a woodpile structure in (a) and (b), respectively. Woodpile photonic crystals have a structure that consists of layers of "logs" arranged in an alternating pattern. The first layer, green in Figure 2.10(a), is oriented parallel to the x-axis. The second layer, in light

blue, is orthogonal to the first and oriented parallel to the y-axis. The third layer is parallel to the first layer, but shifted by a half of a lattice constant. And the fourth layer has the same orientation as the second, but also shifted by a half of a lattice constant. Woodpile photonic crystals exhibit large complete band gaps, with gap-midgap ratios of around 20%. [56] For this reason, they have been the subject of much study, with the goals of maximizing the bandgap [57] and utilizing less-costly methods of producing them. [58] Chapters 5 and 8 discuss our methods of fabricating woodpile and woodpile-like photonic crystal templates.

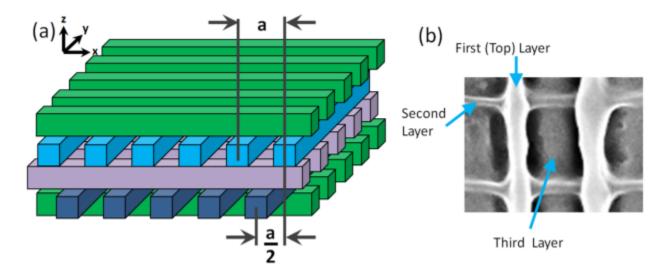


Figure 2.10. (a) Diagram of idealized woodpile structure. (b) Scanning electron microscope (SEM) image of a woodpile photonic crystal template, viewed from above the structure. The first, second, and third layers are visible.

# 2.6 Defects in Photonic Crystals

EM modes with frequencies in the bandgap of a photonic crystal are not allowed to propagate. But if a defect is created inside the photonic crystal, such as a missing rod or row of rods, EM waves with frequencies inside the bandgap will be allowed to propagate inside the defect. Defects are not restricted to removal of lattice points. This is illustrated in Figure 2.11. A

rod or row of rods can be increased or decreased in size, the spacing between lattice points can be changed for a group of lattice points [6], or the type of lattice itself may change. [59] Defects need only to break the symmetry of the photonic crystal at a point or collection of points. Although in the examples of this section, the discussion is mainly of two-dimensional photonic crystals with defects, one-dimensional and three-dimensional photonic crystals with defects have been realized. 1D photonic crystals with defects can confine light within a nanocavity [60], and point and line defects embedded into woodpile photonic crystals can be used to realize true three-dimensional photonic circuits. [14,61]

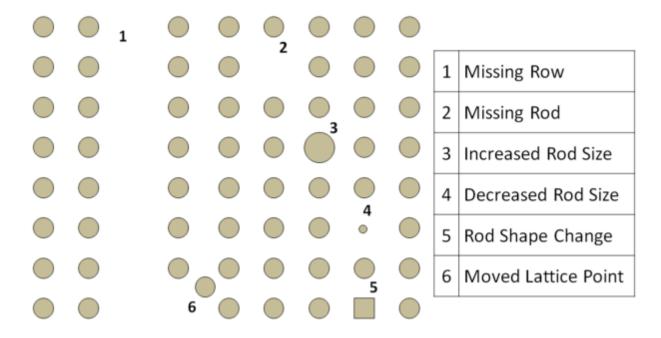


Figure 2.11. Diagram illustrating defect types in a 2D square lattice of isolated rods.

In general, there are two types of defects within the bulk of photonic crystals: point defects and linear defects. Point defects can be introduced into a photonic crystal to create a resonant cavity with a resonant frequency inside the bandgap, which has found applications for producing micro- and nanocavity lasers. [20-21,23,62] Linear defects can be used to realize photonic crystal waveguides. [9-12,14,18] Since the modes in the line defect have frequencies

inside the photonic bandgap, they are forbidden to propagate into the bulk of the crystal. Because of this, light propagating in the linear defect can do so without scattering losses, making photonic crystals an ideal medium for producing micro/nanoscale photonic circuits. Additionally, combinations of linear and point defects can be used to produce passive photonic circuit elements, such as splitters [12-13], bends [9,12], linear waveguide-cavity filters, add-drop and channel-drop filters [6,15-19], examples of can be seen in the image of the finite-difference time-domain (FDTD) simulation in RSOFT of the electric field of a TM wave propagating through a photonic circuit in a square lattice of rods in Figure 2.12.

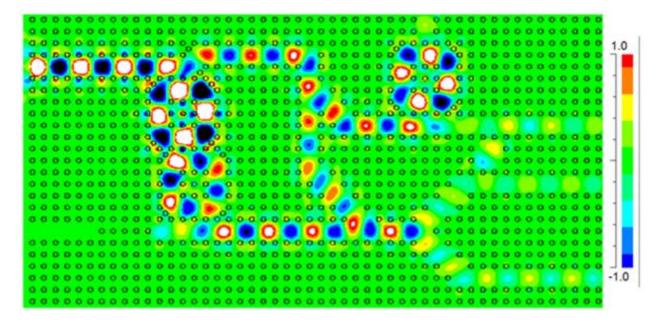


Figure 2.12. FDTD simulation of electric field of propagating TM-polarized light in photonic circuit in a 2D square lattice of isolated dielectric rods. The light propagating through the circuit has a frequency within the photonic bandgap, and is confined to the circuit. Bends, splitters, and channel-drop filters are present in the circuit.

#### CHAPTER 3

#### **FABRICATION OF PHOTONIC CRYSTALS**

Photonic crystals have opened up many possibilities for the manipulation and control of light. Defect structures in photonic crystals can be arranged to produce photonic circuits, which can lead to devices for photonic computing components. But fabrication of photonic crystals remains a challenge, particularly 3D photonic crystals. Fabrication methods have come a long way from the drilling of a macroscopic dielectric slab to create Yablonovite for the microwave range of the spectrum. [55] Microscale and nanoscale fabrication is more accessible now, with the variety of tools available. While there are many methods for fabricating photonic crystals, only a few select methods will be discussed here. With each method, there are advantages and disadvantages depending on the intended purpose of fabrication. Speed of fabrication, resolution of fabricated structures, diversity of structures produced, and, of course, cost, are factors determining the course of our research. A brief review of the fabrication methods will be outlined before discussing the one used in our research: holographic (interference) lithography.

## 3.1 Overview of Photonic Crystal Fabrication Methods

Table 3.1, displayed below, shows a comparison of the methods of fabrication of photonic crystals. The five methods being compared are colloidal self-assembly, electron beam lithography, direct laser writing, and holographic lithography. Colloidal self-assembly was first used for production of inverse opal photonic crystals in 2001 [63] by depositing silica microspheres in suspension onto a silicon substrate. The microspheres form a close-packed FCC lattice on the substrate, and the empty spaces between the spheres were infiltrated with silicon

via chemical vapor deposition (CVD). The silica spheres were then removed by etching, leaving behind a Si inverse opal structure. Advances in colloidal self-assembly have led to the incorporation of defects into the structures [64], but the method is prone to assembly defects such as vacancies, disorder, and stacking faults [65].

Method	Advantages	Disadvantages
Colloidal Self-	Inexpensive	Slow process
Assembly	<ul> <li>Variety of structures possible (limited by micro- or nanoparticles used for assembly)</li> </ul>	Prone to defects
Electron Beam	Very high resolution (sub-10 nm)	<ul> <li>Slow (layer by layer)</li> </ul>
Lithography	Wide variety of nanostructures possible	Expensive
Direct Laser	<ul> <li>Very high resolution (sub-10 nm)</li> </ul>	• Slow
Writing	No limit on variety of structures	<ul> <li>Can only fabricate small areas.</li> </ul>
Holographic	Large area fabrication	Resolution not as high as
Lithography	Wide variety of structures possible	direct laser writing.
	Uniform fabricated structures	
	Fast process	

Table 3.1. A comparison of different methods of fabricating photonic crystals.

Electron beam lithography (EBL) has been used since the 1990s to fabricate photonic crystals. [20, 66-68] In recent years, it is still used to produce photonic nanostructures on a sub-10 nm scale, which is smaller than other methods are currently capable of. However, the slow, scanning layer-by-layer nature of EBL means that fabrication of large area patterns or 3D structures takes too long for rapid fabrication of photonic structures. [69] While EBL is too slow for large area fabrication, it finds use in fabrication of photomasks, which are used in lithography setups, particularly in the semiconductor industry.

Direct laser writing (DLW) is a method which rivals electron beam lithography in terms of possible structures and resolution. DLW accomplishes this through two-photon absorption in photoresist. Photoresists manufactured for use in lithography, such as SU-8, are sensitive to the

ultraviolet (UV) range of light (below 380nm). In a two-photon polymerization process, the photoresist molecule absorbs two photons simultaneously, which behaves like the molecule absorbed a single photon with half the wavelength of the two photons. For example, two 532nm wavelength photons being absorbed simultaneously will cause the same excitation as a single 266nm wavelength photon. To achieve two-photon absorption, the intensity must be very high in order to have enough photons to have the chance of a two-photon excitation.49 Typically, this is achieved using a pulsed laser with a high numerical aperture microscope objective lens to tightly focus the light into a very small spot.[70-72] Recently, a continuous wave 532nm laser was used to direct laser write structures in SU-8.[72] Single photon absorption was ruled out in that case, leaving two-photon absorption as the mechanism behind the polymerization of SU8. DLW is a layer-by-layer process, and as such, is very slow to fabricate even small structures.

Holographic lithography makes use of laser beams interfering in the same region to form a periodic intensity distribution of light in photoresist, which is able to form an entire photonic crystal lattice template in a vastly shorter timeframe than the other methods, with the entire exposure process taking seconds. Holographic lithography has been shown to be a versatile, low-cost method of fabrication. While the resolution achieved by this method is not as fine as direct laser writing or electron beam lithography, it is able to pattern much larger areas in a much shorter time. For these reasons, holographic lithography is used in our research as a simple, versatile, low-cost method of rapidly fabricating photonic crystal templates.

### 3.2 Interference

Holographic lithography is based on the interference of two or more coherent, monochromatic electromagnetic plane waves (typically collimated laser beams) to produce a periodic 1D, 2D, or 3D intensity pattern that is recorded in photoresist. The electric field of a monochromatic plane wave (laser beam) is given by

$$\mathbf{E}(\mathbf{r},t) = \mathbf{E}_0 \exp[i(\mathbf{k} \cdot \mathbf{r} - \omega t + \delta)] \tag{3.1}$$

where  $\mathbf{E}(\mathbf{r},t)$  is the complex electric field,  $\mathbf{E}_0$  is the electric field strength constant in the direction of the electric field polarization,  $\mathbf{k}$  and  $\omega$  are the wave vector and angular frequency of the plane wave, respectively, and  $\delta$  is the initial phase of the beam. [73] The real part of the electric field, which is the physical solution, is given by

$$\mathbf{E}(\mathbf{r},t) = \mathbf{E}_0 \cos(\mathbf{k} \cdot \mathbf{r} - \omega t + \delta) \tag{3.2}$$

From the superposition principle, the total electric field at a point where the separate electric fields of two or more plane waves overlap is simply the vector sum of the individual fields:

$$\mathbf{E}_{total} = \mathbf{E}_1 + \mathbf{E}_2 + \cdots \tag{3.3}$$

The intensity of the total electric field is given by

$$I = \langle \mathbf{E}_{total}^2 \rangle = \langle (\mathbf{E}_1 + \mathbf{E}_2 + \cdots) \cdot (\mathbf{E}_1 + \mathbf{E}_2 + \cdots) \rangle$$
 (3.4)

which is to say that the intensity is the time average of the square of the total electric field. By carrying out the dot product on the right side of Eq. (3.4), the equation becomes

$$I = \langle \sum_{i=1}^{N} \mathbf{E}_{i}^{2} \rangle + 2 \langle \sum_{i < j}^{N} \mathbf{E}_{i} \cdot \mathbf{E}_{j} \rangle$$
(3.5)

The first term on the right side of Eq. (3.5) takes the form

$$\langle \mathbf{E}_{i}^{2} \rangle = \langle \mathbf{E}_{0i}^{2} \cos^{2}(\mathbf{k}_{i} \cdot \mathbf{r} - \omega t + \delta_{i}) \rangle$$
 (3.6)

Utilizing the trigonometric identity for cos(A-B), the cosine part of Eq. (3.6) becomes

$$\cos^{2}(\mathbf{k}_{i} \cdot \mathbf{r} - \omega t + \delta_{i}) = [\cos(\mathbf{k}_{i} \cdot \mathbf{r} + \delta_{i}) \cos(\omega t) + \sin(\mathbf{k}_{i} \cdot \mathbf{r} + \delta_{i}) \sin(\omega t)]^{2}$$

$$= \cos^{2}(\mathbf{k}_{i} \cdot \mathbf{r} + \delta_{i}) \cos^{2}(\omega t) + \sin^{2}(\mathbf{k}_{i} \cdot \mathbf{r} + \delta_{i}) \sin^{2}(\omega t)$$

$$+ 2 \cos(\mathbf{k}_{i} \cdot \mathbf{r} + \delta_{i}) \sin(\mathbf{k}_{i} \cdot \mathbf{r} + \delta_{i}) \cos(\omega t) \sin(\omega t)$$

$$(3.7)$$

Given the following time averages of the trigonometric functions,

$$\langle \cos^2(\omega t) \rangle = \frac{1}{2}$$
  $\langle \sin^2(\omega t) \rangle = \frac{1}{2}$   $\langle \cos(\omega t) \sin(\omega t) \rangle = 0$  (3.8)

and keeping in mind that  $E_{0i}^2$  is a constant value, we find that

$$\langle \mathbf{E}_i^2 \rangle = \mathbf{E}_{0i}^2 \left[ \frac{1}{2} (\cos^2(\mathbf{k}_i \cdot \mathbf{r} + \delta_i) + \sin^2(\mathbf{k}_i \cdot \mathbf{r} + \delta_i)) \right]$$
(3.9)

Making use of one more trigonometric identity,

$$\langle \mathbf{E}_{i}^{2} \rangle = \frac{\mathbf{E}_{0i}^{2}}{2} \tag{3.10}$$

The second term on the right hand side of Eq. (3.5), known as the interference term, and takes the following form,

$$\langle \mathbf{E}_i \cdot \mathbf{E}_j \rangle = \langle (\mathbf{E}_{0i} \cos(\mathbf{k}_i \cdot \mathbf{r} - \omega t + \delta_i)) \cdot (\mathbf{E}_{0j} \cos(\mathbf{k}_j \cdot \mathbf{r} - \omega t + \delta_j)) \rangle$$
(3.11)

Using the same cos(A-B) identity as in Eq. (3.6), we find that

$$\langle \mathbf{E}_{i} \cdot \mathbf{E}_{j} \rangle = \langle \mathbf{E}_{0i}$$

$$\cdot \mathbf{E}_{0j} (\cos(\mathbf{k}_{i} \cdot \mathbf{r} + \delta_{i}) \cos(\mathbf{k}_{j} \cdot \mathbf{r} + \delta_{j}) \cos^{2}(\omega t)$$

$$+ \sin(\mathbf{k}_{i} \cdot \mathbf{r} + \delta_{i}) \sin(\mathbf{k}_{j} \cdot \mathbf{r} + \delta_{j}) \sin^{2}(\omega t) +$$

$$+ \cos(\mathbf{k}_{i} \cdot \mathbf{r} + \delta_{i}) \sin(\mathbf{k}_{j} \cdot \mathbf{r} + \delta_{j}) \cos(\omega t) \sin(\omega t)$$

$$+ \sin(\mathbf{k}_{i} \cdot \mathbf{r} + \delta_{i}) \cos(\mathbf{k}_{i} \cdot \mathbf{r} + \delta_{i}) \cos(\omega t) \sin(\omega t) \rangle$$

$$(3.12)$$

After performing the time average, the two cross terms become zero, and the remaining terms pick up a factor of 0.5, resulting in the following equation,

$$\langle \mathbf{E}_{i} \cdot \mathbf{E}_{j} \rangle = \frac{1}{2} \mathbf{E}_{0i} \cdot \mathbf{E}_{0j} (\cos(\mathbf{k}_{i} \cdot \mathbf{r} + \delta_{i}) \cos(\mathbf{k}_{j} \cdot \mathbf{r} + \delta_{j})$$

$$+ \sin(\mathbf{k}_{i} \cdot \mathbf{r} + \delta_{i}) \sin(\mathbf{k}_{j} \cdot \mathbf{r} + \delta_{i}))$$
(3.13)

which leads to

$$\langle \mathbf{E}_i \cdot \mathbf{E}_j \rangle = \frac{1}{2} \mathbf{E}_{0i} \cdot \mathbf{E}_{0j} \cos[(\mathbf{k}_i - \mathbf{k}_j) \cdot \mathbf{r} + (\delta_i - \delta_j)]$$
(3.14)

Taking the results of Eq. (3.10) and Eq. (3.14) and substituting them into Eq. (3.5), we arrive at a general equation for the intensity distribution from the interference of an arbitrary number of monochromatic electromagnetic plane waves (laser beams),

$$I = \sum_{i=1}^{N} \frac{\mathbf{E}_{0i}^2}{2} + \sum_{i < j}^{N} \mathbf{E}_{0i} \cdot \mathbf{E}_{0j} \cos[(\mathbf{k}_i - \mathbf{k}_j) \cdot \mathbf{r} + (\delta_i - \delta_j)]$$
(3.15)

Eq. (3.15) presents the interference pattern in terms of parameters that can be controlled in interference lithography. The number of beams, N, determines the dimensionality of the lattice, as seen in Figure 3.1, where two interfering beams produce a 1D grating (Figure 3.1(a)), three beams produce a 2D lattice (here, a hexagonal symmetry) (Figure 3.1(b)), and four beams can produce a 3D lattice(Figure 3.1(c)). Indeed, four non-coplanar beams can be interfered to produce any of the 14 3D Bravais lattices in a single exposure [74-75] or in multiple exposures [76-77]. By interfering more than 4 beams, even more structures are possible, including woodpile photonic crystals [78] and photonic quasicrystals [79-82].

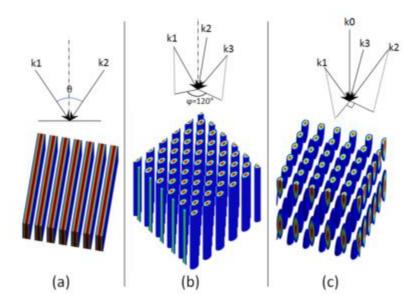


Figure 3.1. Chart showing iso-intensity surfaces for interference patterns from the interference of (a) 2, (b) 3, and (c) 4 beams (3 side beams + 1 central beam). Polar interference angle with optical axis is identical for all side beams. Azimuthal angles between side beams are (a) 180°, (b) 120°, and (c) 90 for angle between k1 and k2, and between k2 and k3.

The difference between the wave vectors of the different beams,  $\mathbf{k}_i - \mathbf{k}_j$ , determines the reciprocal lattice vectors of the lattice, and subsequently, the lattice vectors of the crystal lattice. The lattice constants of the photonic crystal resulting from the interference of multiple beams are proportional to the wavelength, due to the reciprocal lattice vectors being inversely proportional. The polarization vectors of the laser beams determine the distribution of intensity within the unit cell. [47, 83] The phase difference between the beams,  $\delta_i - \delta_j$ , can have a great effect on the interference pattern. By shifting the phase of one or more beams, the resulting interference pattern will shift, and the intensity distribution within the unit cell can change. [47, 84-89] For example, with four side beams and central beam, as seen in Fig. 3.2, the pattern

shifts from a lattice of isolated ellipsoids to an interconnected woodpile-like structure when two of the beams are given a phase shift of  $\pi/2$ .

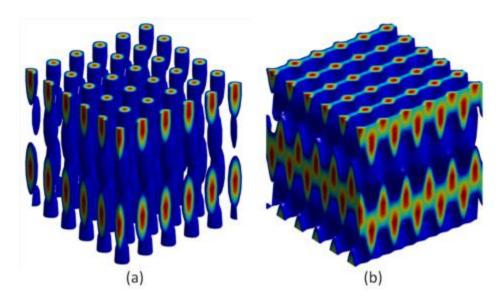


Figure 3.2. Interference patterns of 4 side beams and a central beam (4+1) with (a) all of the beams having the same phase, and (b) two of the side beams with phases shifted by  $\pi/2$  relative to the other two side beams.

### 3.3 Photoresist and Fabrication

Some of the conditions for holographic lithography are not represented in Eq. (3.15). The properties of the exposure process and of the photoresist also have an effect on the structure that develops. Photoresists consist of a monomer that has been sensitized to light of a certain wavelength or range of wavelengths. There are two types of photoresists: positive and negative. In a negative photoresist, the resist that is exposed to the light of the interference pattern is polymerized, and the unexposed resist is removed with a developer. In a positive photoresist, the resist that has been exposed to the interfering beams is removed, while the unexposed regions are allowed to polymerize and remain, leaving the inverse structure of the

interference pattern. For the research covered in this dissertation, negative photoresist was used.

Photoresists are made to be sensitive to certain spectra of light, but mixtures of photoresist monomer with various sensitizer chemicals can make the photoresist mixture more sensitive to a particular wavelength. For example, SU-8 photoresist has strong absorption in the UV range, [90] but adding photosensitizers will make SU-8 sensitive to wavelengths in the visible spectrum. [91] Dipentaerythritol penta / hexa-acrylate (DPHPA), [92] the photoresist used in the research described in later chapters, can be sensitized to light of 532 nm wavelength by adding the photoinitiator Rose Bengal. [88] The amount of photoinitiator (as well as co-initiator and chain extender) varies between setups and applications. [93-94]

The number and intensity of the interfering beams can affect these numbers, as well as the exposure time of the photoresist to the interference pattern. In Figure 3.3, two simulations in MATLAB of a five beam interference pattern are shown (4 side beams and a central beam). The interference pattern is calculated, and then a threshold operation is performed, removing the iso-intensity surfaces below that threshold. In Figure 3.3(a), the simulated exposure time is longer, resulting in a structure with a higher filling fraction. In Figure 3.3(b), the exposure time is less, resulting in a more isolated structure. Ideally, for a 3D photonic crystal template, the structure should be bicontinuous, meaning that the polymerized photoresist structures are interconnected and that the air regions are also interconnected.

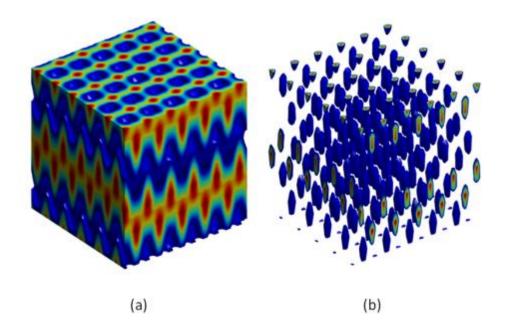


Figure 3.3. Simulated effects of exposure threshold in MATLAB. (a) Longer exposure to laser interference pattern leads to higher fill fraction and interconnected structure. (b) Shorter exposure produces lower fill fraction and a lattice of isolated ellipsoids.

A bicontinuous structure allows the undeveloped photoresist to be dissolved and removed from the polymerized photonic crystal template after exposure by allowing the developer to flow freely throughout the template. For an overexposed structure, as in Figure 3.3(a), the undeveloped photoresist will become trapped and irremovable. For an underexposed structure, as in Figure 3.3(b), the exposed regions are isolated, and the entire structure will collapse and wash away with the photoresist in the development process. Bicontinuity is not a necessary condition in 1D or 2D photonic crystal templates, as the developer can wash completely over the entire surface, removing unpolymerized photoresist.

To produce the photonic crystal from the template, a silicon double inversion procedure can be used. [95] After removing the unpolymerized photoresist, the inverse structure of a 3D photonic crystal template can be made through infiltration with silica via chemical vapor

deposition. The photoresist can be removed after this step using plasma etching or heating to high temperatures. Then the inverse structure is infiltrated with Si, the silica is dissolved, leaving behind a Si replica of the holographically fabricated photonic crystal template.

# 3.4 Methods of Holographic Lithography

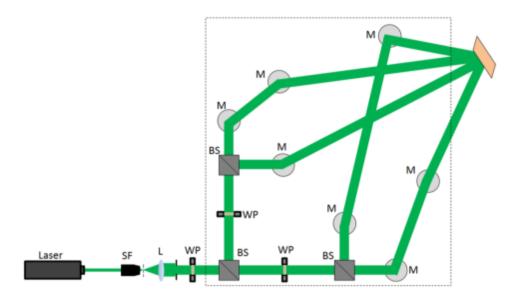


Figure 3.4. Diagram of an example of a conventional holographic lithography setup. The beam is expanded by the spatial filter (SF) and the polarization is adjusted by the waveplate (WP) before it is split by the first beam splitter (BS). The two beams are split once again to produce 4 beams, which are then directed by mirrors (M) to interfere at the photoresist sample. In the dashed box, there are 12 bulk optical elements.

As seen in Figure 3.1, any structure fabricated through holographic lithography must use two or more beams. There are many methods for generating the requisite number of beams needed to produce any desired pattern. Conventional holographic optical setups [47, 87, 96] generate the multiple beams using bulk optical elements such as beam splitters, mirrors, and wave plates (for polarization), as seen in an example setup in Figure 3.4. Furthermore, to modify parameters such as phase or polarization of the individual beams, additional optical

elements have to be added to the setup. Such complex setups are subject to misalignment, with even small deviations in the optical path length of the interfering beams introducing phase delays which may not be desirable for fabrication of certain structures. Additionally, complex conventional interference lithography setups are subject to vibration as well, which can further complicate the fabrication process by adding a time-dependent phase delay to the beams. To avoid such complex setups, some groups opted to use multiple exposures of two beam interference patterns, but this increases the length of the exposure process. [97] To reduce both fabrication time and the complexity of the optical setup and consequently, reduce the probability of misalignment and the effects of vibration, holographic lithography setups can be modified to use a single refractive, reflective, or diffractive optical element to generate the interfering beams. A single laser beam can be used with a single optical element to generate the beams and expose the photoresist film to the interference pattern in one step. Thus, the process is shortened, complexity is reduced, and the optical setup is more stable.

Refractive single optical elements have found much use in the last decade for fabrication of photonic structures. [78-81,98-104] Typically, a top-cut prism (TCP) is used with an aperture array to simultaneously generate and interfere the beams together. A diagram of a TCP-based setup is shown in Figure 3.5. A single, expanded, collimated laser beam is incident upon an aperture array, which selects a number of side beams and a central beam. The beams enter the TCP, whereupon they are reflected from the internal surfaces of the facets of the prism and are transmitted through the bottom of the prism, where they interfere with the central beam in a photoresist film positioned just beneath.

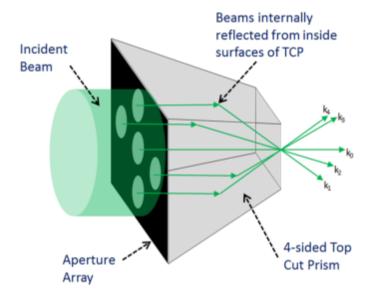


Figure 3.5. Top cut prism with aperture to select beams and block unwanted illumination. This example shows a TCP capable of generating 4 side beams and a central beam. Interference of the beams occurs outside the bottom of the prism (shown to the right in this figure).

This approach was used in by Wu et al in 2005 [98] to fabricate 2D hexagonal and 3D fcc-type photonic crystal in SU-8 photoresist. The following year, hexagonal TCPs were used to holographically fabricate 2D honeycomb structures [99]. By using a four-sided, truncated pyramidal prism with wave plates mounted in the aperture above the prism to adjust the polarizations of each beam, Pang et al realized a woodpile photonic structure in SU-8 photoresist [78]. TCPs have also been used to fabricate through holographic lithography a variety of photonic quasicrystal structures [79-81], and even metamaterial structures [101]. While a TCP can generate and interfere the beams needed to fabricate many different structures, to create structures with large bandgaps requires tuning the phase of at least one beam. In Xu et al [102], a glass slide was mounted on a rotation stage and positioned in front of a top-cut, four-sided prism, providing a phase delay for one of the beams. By rotating the glass

slide, the phase could be tuned to different values. With a phase delay  $\Delta\delta$  =  $\pi$  in one of the beams, interconnected woodpile structures were produced that had a bandgap with a gap-midgap ratio of 25%.

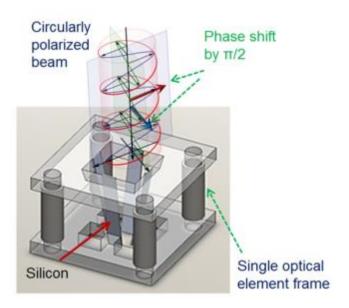


Figure 3.6. Diagram of single reflective optical element setup.

Reflective optical elements (ROE) make use of dielectric facets set into a mold or frame [105-107]. A diagram of an ROE setup is shown in Figure 3.6. A circularly polarized beam is incident upon the ROE. An aperture array (not shown) blocks unwanted light and allows certain beams of the incident laser to enter the ROE. The allowed light is reflected from silicon (or other dielectric) facets that have been placed inside at an angle  $\beta$  into 4 or more s-polarized beams (depending on the number of facets in the ROE). If  $\beta$  is kept close to the Brewster angle of the facet material, then most of the light will be s-polarized. Due to the intrinsic phase shift of  $\pi/2$  in a circularly polarized beam, a four-faceted ROE will have a phase shift of  $\pi/2$  in two of the side beams, resulting in a woodpile-type photonic crystal. ROEs with five facets were shown to yield 3D five-fold symmetric quasicrystal structures when photoresist was exposed to the

interference pattern created by the interfering beams generated by the ROE, and 6-fold symmetric structures were fabricated with a 6+1 beam configuration generated by a hexagonally arranged ROE. [107] ROEs will be discussed more in Chapter 5.

Diffractive optical elements (DOE) are typically diffraction gratings or arrangements of diffraction gratings in which the beams diffracted from the gratings are interfered together to produce photonic crystal templates. The diffraction from a grating is given by the grating equation,

$$a\sin\theta = m\lambda \tag{3.16}$$

where a is the period of the grating, m is the order of the diffracted beam,  $\lambda$  is the wavelength of the incident laser beam, and  $\theta$  is the angle that the diffracted beam of order m is diffracted into. Gratings can be readily fabricated using holographic lithography, [82,93-94,108] as seen in the image of two interfering beams in Figure 3.1, or by using electron beam lithography. [109] The gratings used in holographic lithography typically take the form of phase masks, where the grating consists of a metal or dielectric deposited onto a substrate with a periodic height difference, leading to a periodic difference in the refractive index. This leads to multiple diffracted beams that can be used for fabrication of photonic crystal templates. Two examples of DOEs are shown in Fig. 3.8

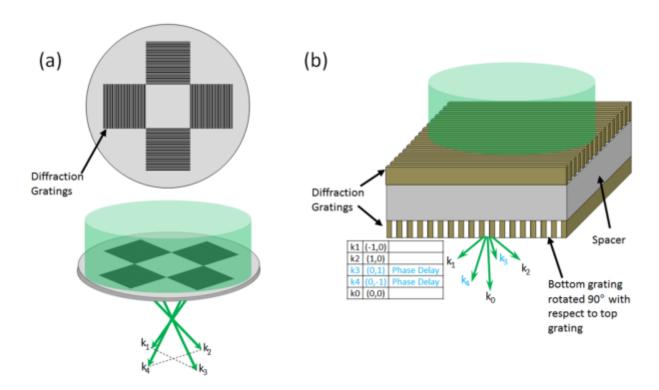


Figure 3.7. (a) Single-layer DOE made of 4 diffraction gratings symmetrically arranged around a mask. Diffracted beams are interfered beneath the DOE. (b) 3-layer DOE made of two orthogonally-oriented gratings with a spacer in between.

Berger et al [110] first used a single DOE, a mask composed of three diffraction gratings rotated 120° relative to each other, to holographically fabricate 2D hexagonal photonic crystals in 1997. The three first order beams diffracted from the gratings were interfered in a region below the mask, creating a 2D hexagonal interference pattern in photoresist. Following that line of work, Divliansky et al [111]used a DOE similar to that of Berger et al, but added a hole in the center of the 3 grating mask to allow a central beam to pass through. The resulting structure was a 3D hexagonal structure. The interference of a central beam along the optical axis of the setup with beams arranged symmetrically from off-axis introduces a periodicity in the interference pattern parallel to the optical axis (typically labeled as the z-axis). More diffraction gratings can be arranged symmetrically about the center of the mask, which

generates more first order beams that can be interfered. By arranging five diffraction gratings symmetrically about the center of the mask and allowing the central beam to pass through, 3D ten-fold symmetric quasicrystal structures can be formed. [82] With four gratings arranged symmetrically about a central aperture on the mask, four side beams plus a central 3D face-centered tetragonal interference patterns can be formed. When a phase shift of  $\pi$  is introduced into a side beam, a diamond –like lattice is formed. Additionally, by blocking part of the central beam with an amplitude mask, a line defect can be created in the lattice. [94]

Another type of DOE used to fabricate 3D photonic crystals is a stack of two orthogonally oriented gratings. In Ohlinger et al, [108] two orthogonally oriented diffraction gratings were separated by thermally tunable spacer layer. A single circularly polarized laser beam was incident upon the three-layer DOE. The first grating diffracts an incident, linearly polarized laser beam into two first order beams, (+1, 0) and (-1, 0), and a zero order beam, (0, 0). The second, orthogonally-oriented grating diffracts the (0, 0) beam, producing two new first order beams, (0, +1) and (0, -1), and a zero order beam. But since the (+1, 0) and (-1, 0) beams generated from the first grating have a longer optical path length, they have a phase delay. The DOE was heated so that the spacer layer would expand, tuning the phase delay that was added to the (±1, 0) beams. The expansion of the spacer layer was controlled such that the phase delay for the  $(\pm 1, 0)$  beams was adjusted to be  $\pi/2$ . When the (0, 0),  $(\pm 1, 0)$ , and  $(0, \pm 1)$  beams are interfered in photoresist thin film positioned beneath the DOE, interconnected woodpile structures were produced. Earlier papers [163-164] reported the use of DOEs consisting of two orthogonally oriented gratings separated by an air gap adjusted to produce a phase delay of  $\pi/2$  in the (±1, 0) beams to fabricate diamond-like woodpile photonic lattices. The air gap was

tuned using a pressure adjustable mount. Both approaches to the 3-layer phase mask method display the capability to produce a range of structures using four 1<sup>st</sup> order diffracted beams and a 0<sup>th</sup> order beam by tuning the phase of two of the beams. However, the number of first order beams generated, as well as the diffraction angle of the beams, is locked upon fabrication of the phase mask. To dynamically change the number of beams generated, the diffraction angle of the first order beams diffracted from the surface, and fine adjustment of the phases of the those beams, a spatial light modulator with phase modulation can be used.

#### CHAPTER 4

#### SPATIAL LIGHT MODULATORS

### 4.1 General Information

A spatial light modulator (SLM) is a device that creates a spatially varying modulation of the amplitude or phase of incident light. Amplitude modulation spatially varies the amplitude of the beams as a function of position. Phase modulation adjusts the phase of the beam by modifying the optical path length.

Commercially available SLMs typically use two different methods of light modulation: digital micromirror devices (DMD) and liquid-crystal-on-silicon (LCoS). DMDs, such as the Texas Instruments digital light processing (DLP) chip, are devices which are often used in digital projector units found in classrooms and cinema. DMDs use a rectangular array of microscopic mirrors on hinges that tilt toward or away from the light source, creating a dark or bright spot in the modulated beam. The advantages of using a DMD are the high damage threshold [112] and high resolution. The disadvantage is that commercially available DMDs are binary amplitude modulators, incapable of modulating the phase. [113] Since DMDs cannot modify the phase of light incident upon the device, we look to LCoS devices.

LCoS-SLMs are capable of modifying the phase of an incoming beam by changing the orientation of molecules in a layer of liquid crystal (LC) in an array of digitally addressed pixels. This results in a change in the refractive index of the pixel, and the optical path length of the beam changes, resulting in a phase delay for that portion of the beam. A diagram of the SLM structure of the SLM used for this research, the HoloEye PLUTO, is shown in Fig. 4.1(b). Incident light passes through the glass cover, transparent electrode, and alignment layers. Upon

propagating through the liquid crystal layer, the incident light picks up a certain amount of phase, dependent on the orientation of the liquid crystal molecules in that layer. Light passes the second alignment layer and is reflected from the reflective pixel layer on the silicon CMOS layer. The second traversal of the LC layer adds a second phase delay to the beam before the leaving the SLM.

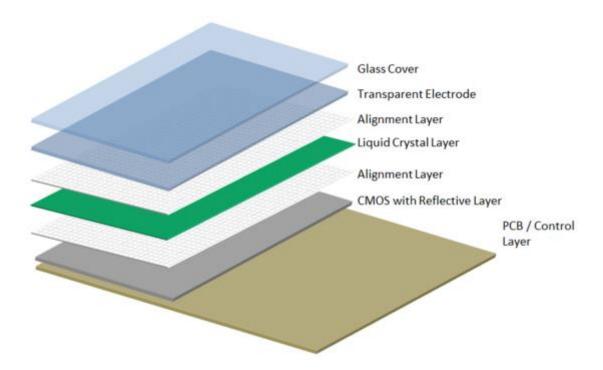


Figure 4.1. Diagram of the structure of a LCoS-SLM, broken down into layers.

# 4.2 Phase Modulation from Liquid Crystals

Liquid crystals are states of matter that have properties that are between a solid crystal and a liquid. While there are many different types of LC, the type used in LCoS devices is primarily of the nematic phase. Nematic liquid crystals are composed of uniaxial, rod-like molecules, as seen in Figure 4.2. The index ellipsoid for a uniaxial LC molecule, with the principal axes and the refractive index along those axes indicated, is shown in Figure 4.2(a). For a uniaxial LC molecule, the refractive index along two of the principal axes is the same. The

director points along the long axis of the molecule, which has a refractive index of  $n_e$  for a laser with the electric field orthogonally polarized to the director. The short axes of the molecule have a refractive index of  $n_o$ . [114,115] These two values describe the birefringence of the liquid crystal, given by

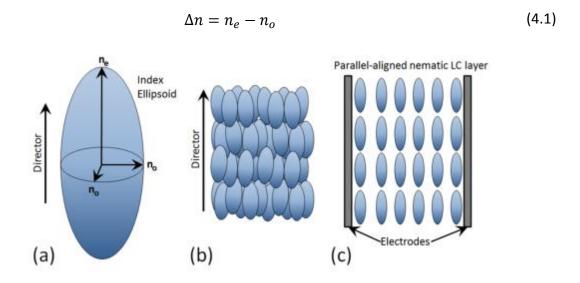


Figure 4.2. (a) Index ellipsoid for uniaxial LC molecule. Refractive indices along the principal axes are shown. (b) Orientation of nematic LC molecules in a LC cell. The average orientation is parallel to the director, but the positions of the molecules are random. (c) Schematic showing the orientation of parallel-aligned nematic (PAN) LC molecules in a pixel between transparent electrodes. The director of the LC layer is parallel to the surface of the electrodes.

Nematic liquid crystals tend to order themselves such that the long axes of all the molecules are parallel, but the molecules do not organize into layers or planes like a solid crystal. This is shown in Figure 4.2(b). Aside from the condition that the long axes are parallel, there is no order to the arrangement of the nematic liquid crystal molecules. In the HoloEye PLUTO SLM, the liquid crystals are parallel-aligned nematic, which means that the long axes of the liquid crystal molecules are parallel to the electrode surfaces, as seen in Figure 4.2(c). [116-117]

When a voltage is applied across the transparent electrode layers, the applied electric field induces dipoles in the LC molecules, which cause a torque to be applied to the LC molecules. The torque, described by  ${\bf N}={\bf p}\times{\bf E}$  for each LC molecule, is in a direction such that the long axis of the molecules will rotate to align with the electric field produced by the voltage. The angle that the molecules rotate, due torque produced by the electric field from the applied voltage, is given by [114]

$$\theta = \frac{\pi}{2} - 2 \tan^{-1} \exp\left(-\frac{V - V_c}{V_0}\right), \text{ for } V > V_c$$
 (4.2)

where V is the applied voltage, Vc is a voltage below which no rotation of the molecules occurs, and Vo is a constant. For a beam of light incident upon the liquid crystal cell, with the electric field of the beam polarized parallel to the long axes of the LC molecules prior to application of the voltage, the resulting phase shift [114] is described by

$$\varphi = \frac{2\pi d}{\lambda} [n(\theta)] \tag{4.3}$$

where d is the thickness of the liquid crystal layer,  $\lambda$  is the wavelength of the incident beam, and  $n(\theta)$  is the index of refraction of the liquid crystal cell, defined by

$$\frac{1}{n^2(\theta)} = \frac{\cos^2 \theta}{n_e^2} + \frac{\sin^2 \theta}{n_o^2}$$
 (4.4)

The phase shift is governed by the tilt angle of the LC molecules in each pixel, which is determined by the applied voltage across the pixel. The voltage across a pixel (LC cell) is determined by the SLM software from a lookup table (LUT), also called a gamma curve, that converts the gray levels in a grayscale image, sent from a computer's graphics processing unit (GPU), into voltages. [116] Thus, the phase shift for the beam at each pixel is determined by the gray levels of each pixel of an image displayed on the SLM.

### 4.3 4f Imaging System and Fourier Transforms

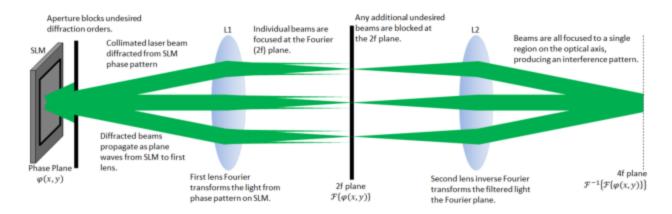


Figure 4.3. Diagram of 4f imaging system used in SLM optical setup.

Figure 4.3 shows a diagram of the 4f imaging system used in the SLM optical setup. On the left is the SLM with a phase image displayed on it. For the purposes of our research, the phase images displayed on the SLM are either binary or contain few gray levels. A binary phase image, such as the binary checkerboard image seen in Figure 4.4(a), can act as a diffractive phase mask when displayed on the SLM. A collimated laser beam incident on the SLM while the binary checkerboard phase is displayed will diffract into many orders according to Eq. (3.16). The wavelength of the laser beam is fixed, so only the period of the phase pattern affects the diffraction angles. In Chapters 6-10, we make use of phase patterns on the SLM and will discuss the subject more in those chapters.

A shield and iris aperture in front of the SLM block most diffracted orders, allowing only the lower order (zero, first, second, etc.) beams to propagate. To make use of the diffracted beams, a converging lens is placed a distance f1 from the SLM, where f1 is the focal length of the lens. The lens will individually focus each beam from directions ( $\theta x$ ,  $\theta y$ ) to points  $(x',y')=(f\theta_x,f\theta_y)=(f\lambda v_x,f\lambda v_y)$  in the back focal plane of the lens, where ( $\theta x$ ,  $\theta y$ ) are the

projections onto the x & y planes of the angle that the beam makes with the optical axis, respectively, f is the focal length,  $\lambda$  is the wavelength, and  $(v_x, v_y)$  are the spatial frequencies in the x and y directions of the gray levels (different phase levels) constituting the phase pattern.

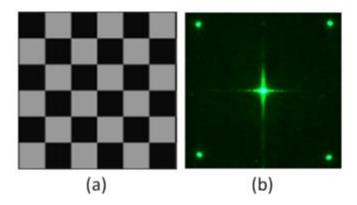


Figure 4.4. (a) 2D binary checkerboard phase pattern to be displayed on the SLM. (b) Fourier plane image of beams diffracted from the SLM while the pattern in (a) was displayed.

Converging lenses have the very useful property of being able to Fourier transform an input image such as the phase pattern on the SLM. [73,114] The diffracted beams that are at a small enough angles to pass through the aperture of the lens will undergo a Fourier transform. If f(x,y) represents the input phase distribution on the SLM at the front focal plane of the first lens, then  $F(v_x, v_y)$  is the Fourier transform of the phase distribution, [114,] described by

$$F(v_x, v_y) = \int_{-\infty}^{\infty} f(x, y) \exp[2\pi i (v_x x + v_y y)] dxdy$$
 (4.5)

But Eq. (4.5) does not alone describe the complex electric field amplitude of the distribution of light diffracted into the 2f plane. Instead, it can be described with

$$E(x,y) = h_0 \exp\left[\frac{i\pi}{\lambda f^2} (d - f)(x^2 + y^2)\right] F(v_x, v_y)$$
 (4.6)

where f is the focal length, d is the distance from the f(x,y) plane to the lens, and h0 is factor from the propagation of the plane wave through free space, given by [114]

$$h_0 = \frac{i}{\lambda f} \exp[ik(d+f)] \tag{4.7}$$

If the phase image displayed on the SLM is not at the front focal plane of the first lens, then the exponential term in Eq. (4.6) will add a lens phase [114] to the field in the 2f plane. But if the SLM is located exactly at the front focal plane of the lens such that d = f, then the exponential term in Eq. (4.6) is equal to unity, h0 becomes a constant, and the complex field amplitude becomes

$$E(x,y) = h_0 F(v_x, v_y) \tag{4.8}$$

The Fourier transform of the phase pattern on the SLM, represented by Eq. (4.8), forms a diffraction pattern in the 2f plane from the beams diffracted from the pattern, as seen in Figure 4.4(b). Each diffraction spot represents a spatial frequency of the phase pattern. It is in the 2f plane that a filter can be placed to block unwanted diffraction spots. For example, in Chapter 6, four of the first order diffracted beams are allowed to pass through the filter, but the zero order beam (on the optical axis) and all beams with orders higher than the first are blocked, preventing propagation to the second lens. The second lens is located a distance f2, the focal length of the second lens, from the 2f plane. It performs an inverse Fourier transform on the selected beams, which causes the individual beams to once again propagate as plane waves and recombine at the 4f point. The recombination of the selected beams at the 4f point creates an interference pattern. A thin film of photoresist placed at this point will record the interference pattern (Eq. (3.15)), resulting in a photonic crystal template, as is demonstrated in Chapters 6-10. If no filtering is performed, and all of the diffracted beams are allowed to

interfere at the 4f point, then the resultant intensity pattern will reconstruct the original phase pattern as an intensity pattern. [114]

# 4.4 Spatial Light Modulators in Holographic Lithography

Recently, SLMs have been used to engineer the phases of interfering beams through computer generated holograms to fabricate various photonic structures, such as quasi-periodic [118,119], periodic [89,119–120], multi-periodic [121], and chiral photonic structures [122]. Several methods have been used to incorporate desired functional defects into the PhC lattice through SLM-based holographic lithography [123-136]. Pioneering works using SLM as a masks or an adaptive optical element have demonstrated the formation of complex point and line defects and zigzag waveguides in PhC [123, 136]. Desired point defects can be fabricated into background PhC lattices using an SLM by superposing a Bessel beam into the background wavefield [124,125]. By specifying the phases [126] or gray levels of simple geometric phase patterns [127] and displaying them on the SLM, point or line defects can be embedded in PhCs. Gradient photonic lattices can be generated through spatially varying pixel-by-pixel phase engineering of phase patterns [128], or through production of hexagonal lattice wave fields with a gradient basis [130]. Spatially variant photonic crystal lattices have been fabricated with the SLM using an innovative synthesis approach that calculates the structure of the lattice while varying lattice orientation, lattice spacing, and filling fraction [133,137-140]. Although these methods were successful for the fabrication of functional PhCs using an SLM, arbitrary designs of phase patterns can result in an assignment of several gray levels on a single pixel, thus having a superlattice effect.

#### CHAPTER 5

#### HOLGRAPHIC FABRICATION OF 3D PHOTONIC CRYSTALS USING

#### A SILICON-BASED REFLECTIVE OPTICAL ELEMENT<sup>1</sup>

Conventional multiple-beam interference lithography setups typically require several bulk optical elements, such as beam splitters, mirrors, and polarizers, to modify and control the interference parameters. Such setups can be very complicated and optically unstable. To reduce complexity and increase stability in the optical setup, single diffractive or reflective optical elements can be used. In this chapter, we demonstrate a single beam and single optical element based holographic fabrication method where the number of beams, the polarization of the beams, the interference angle of the beams, and the ratio of the intensities of the beams relative to the incident beam can be generated as desired.

#### 5.1 Fabrication of the Reflective Optical Element

To generate a woodpile photonic crystal, previous works [78] used five beam interference from a top-cut prism. Instead of using a prism to generate the five-beam interference, we used a custom-made reflective optical element (ROE) consisting of a polydimethylsiloxane (PDMS) mold and silicon strips. To create the PDMS mold, the top-cut prism used in Xu et al [102] was seated into a plastic base with a window machined into it, as shown in Figure 5.1(a), and then placed into a container. The PDMS (Dow Corning® Sylgard

<sup>&</sup>lt;sup>1</sup> Parts of this chapter have been previously published, either in part or in full, from J. Lutkenhaus, F. Farro, D. George, K. Ohlinger, H. Zhang, Z. Poole, K. Chen, and Y. Lin, "Holographic fabrication of 3D photonic crystals using silicon based reflective optics element," Opt. Mater. Express 2, 1236-1241 (2012), and J. Lutkenhaus, D. George, K. Ohlinger, H. Zhang, Z. Poole, K. Chen, and Y. Lin, "Holographic fabrication of woodpile-type photonic crystal templates using silicon based single reflective optical element," Proc SPIE 8613, Advanced Fabrication Technologies for Micro/Nano Optics and Photonics VI, 86131C (2013). Reproduced with permission from OSA Publishing and from SPIE Publications, respectively.

184) pre-polymer solution requires a weight ratio of 10 parts polymer base to 1 part curing agent. 45.47g of polymer base was mixed with 4.56g of curing agent, making a weight ratio of 9.97 parts base to 1 part curing agent. After stirring the curing agent into the polymer and blowing the bubbles away, the pre-polymer solution was then poured into the container and placed onto a hot-plate to cure for 90 minutes at 130°C. After curing, the PDMS became rigid, forming the mold, as shown in Figure 5.1(b). The prism was removed, and four silicon strips were placed into each of the inner facets of the PDMS mold, completing the ROE, as shown in Figure 5.1(c). With this configuration, the ROE can generate four side beams arranged symmetrically about a central beam when a single expanded and collimated laser beam is incident upon it. To combat undesired scattering from the PDMS mold, a cross-shaped aperture, similar to that shown in Figure 5.1(d), was cut from black aluminum foil and attached to the top of the ROE. Later iterations of the ROE were 3D printed, allowing more flexibility in design of the number of generated beams, the interference angle, and better design of the aperture to minimize undesired scattering. [106-107]

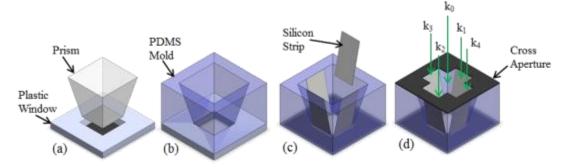


Figure 5.1. Fabrication process of the silicon-based reflective optical element. (a) The prism is seated into the plastic window. (b) The PDMS forms a mold around the prism. (c) The prism is removed and the silicon strips are placed in the inner facets of the PDMS mold. (d) The cross aperture is placed on top of the mold.

#### 5.2 Five Beam Interference from Reflective Optical Element

The laser beam was incident upon the surface of the silicon strip with an angle of 78°. The refractive index of silicon for a wavelength of 514.5 nm is 4.225. [141] The amplitude reflection coefficients, obtained from Fresnel's equations, [73] are -0.05 and -0.9 from beams with polarizations parallel with (p-polarized) and normal to (s-polarized) the incident plane, respectively. According to the above calculation, the reflected beam is s-polarized when the circularly polarized beam is incident onto silicon. The reflectance is 81% for the polarized beam normal to the incident plane and 0.25% for the polarized beam parallel to the incident plane. If the incident beam is perfectly circularly polarized, the theoretical reflectance for each side beam is 40.6%. In our experimental setup, the linearly polarized laser passed through a  $\lambda/4$ wave plate, becoming elliptically polarized with an ellipticity of 1.28. For the incident laser beam k0 propagating in z direction with the original polarization in x direction and passing the wave-plate, the measured reflectance from the silicon strips is 35.6%, 35.6%, 44.9%, and 44.9% for beams k1, k2, k3, and k4, respectively. To address the elliptical polarization of the beam and produce a perfectly circularly polarized incident beam, a polarizing beam splitter cube can be used to completely select one polarization prior to the  $\lambda/4$  wave plate.

After passing the single reflective optical element, the formed four side beams and one central beam can be written as (assuming a same initial phase for all side beams),

$$\mathbf{E}_0(\mathbf{r},t) = \mathbf{E}_{0x}\cos(k_0 \cdot \mathbf{r} - \omega t) + \mathbf{E}_{0y}\cos(k_0 \cdot \mathbf{r} - \omega t + \pi/2),\tag{5.1}$$

$$\mathbf{E}_{i}(\mathbf{r},t) = \mathbf{E}_{iy}\cos(k_{i}\cdot \mathbf{r} - \omega t + \delta), \qquad \{i = 1,2\}, \tag{5.2}$$

$$\mathbf{E}_{i}(\mathbf{r},t) = \mathbf{E}_{ix} \cos(k_{i} \cdot \mathbf{r} - \omega t + \delta), \qquad \{j = 3,4\}, \tag{5.3}$$

where k and  $\omega$  are the wave vector and angular frequency of the beam, respectively. E is the constant of the electric field strength, and  $\delta$  is the initial phase of the beam. Wave vectors of these five beams can be written as  $\{k0, k1, k2, k3, k4\} = 2\pi/\lambda\{[0, 0, 1], [\sin \theta, 0, \cos \theta], [-\sin \theta, 0, \cos \theta], [0, -\sin \theta, \cos \theta], [0, \sin \theta, \cos \theta]\}$ , where  $\lambda$  is the wavelength of the laser ( $\lambda$  = 514.5 nm) and  $\theta$  is the angle between four side beams and central beam. When these five beams overlap, an interference pattern will be formed, which is determined by the following equation:

$$I(r) = I_0 + \Delta I(r) = \langle \sum_{i=1}^{5} E_i^2(r,t) \rangle + \sum_{i< j}^{5} E_i \cdot E_j \cos[(k_i - k_j) \cdot r + (\delta_i - \delta_j)]$$
 (5.4)

As demonstrated in [93], a five beam interference pattern can be considered to be two overlapping three beam interference patterns. Due to the orthogonal polarization between beams (k1, k2) and beams (k3, k4), this five beam interference can be treated as two parallel three beam interferences. The interference part of Eq. (5.4) can be written as the sum of two terms:

$$\sum_{i< j}^{3} E_{ix} \cdot E_{jx} \cos[(k_i - k_j) \cdot r + \delta]$$
 (5.5)

$$\sum_{p < q}^{3} E_{py} \cdot E_{qy} \cos \left[ \left( k_p - k_q \right) \cdot r + \frac{\pi}{2} + \delta \right]$$
 (5.6)

Each term represents a three beam interference pattern as shown in Figure 5.2(a), but the orientation of one term is rotated by 90° with respect to the other. The phase in Eq. (6) can be written as  $(k_p-k_q)\cdot r+\frac{\pi}{2}+\delta=(k_p-k_q)\cdot (r+r_d)+\delta$ , where  $(k_p-k_q)\cdot r_d=\pi/2$ . Thus,  $r_d=(0.25~a,0,0.25c)$  is the shift of interference (among beams k<sub>0</sub>, k<sub>1</sub>, and k<sub>3</sub>) due to the

phase delay, where a and c are the lattice constants in x (or y) and z directions, respectively. The lattice constants are given by the following equations,

$$a = \frac{\lambda}{\sin \theta} , \qquad (5.7)$$

$$c = \frac{\lambda}{2\sin^2(\theta/2)} \,\,\,(5.8)$$

where  $\lambda$  is the laser wavelength, and  $\theta$  is the interference angle between the central beam and a side beam. The interference pattern due to two parallel three beam interferences is shown in Figure 5.2(b). The shift of pattern in one direction relative to the other is clearly observed and the formed pattern is a woodpile-type structure.

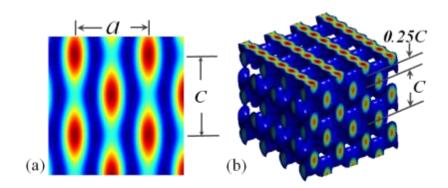


Figure 5.2. (a) Three beam interference pattern. (b) Five beam interference pattern, shifted by 0.25c due to phase delay.

### 5.3 Holographic Fabrication of Woodpile Photonic Crystal Templates

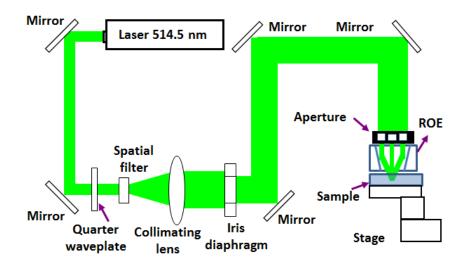


Figure 5.3. Schematic of the experimental setup for the fabrication of woodpile-like photonic crystal templates using the single silicon-based reflective optical element.

The experimental setup shown in Figure 5.3 used an Ar ion laser beam (Coherent, Inc.) at a wavelength of 514.5 nm. The beam passed through a quarter-wave plate, changing the polarization from linear to circular (elliptical, in this case). It was then passed through a spatial filter to remove unwanted intensity variations in the beam, and expanded to a diameter of 2 inches. Then the cross aperture attached to the top of the ROE blocks all of the laser beam that is not incident upon either the silicon strips or the central open part of the ROE. The central part of the beam passes through the ROE unaltered, and the four side beams are generated from the reflection of the beam from the silicon strips. The central beam and the four side beams then interfere in a region below the ROE, where a sample of photoresist mixture was placed.

The photoresist mixture consisted of the following components in the specified weight concentrations: dipentaerythritol penta/hexaacrylate (DPHPA) monomer (Aldrich, 90.36%);

rose bengal photo-initiator (0.16%); N-phenyl glycine co-initiator (0.67%); and N-vinyl pyrrolidinone (8.81%), a chain extender. The DPHPA mixture was spin-coated onto a glass slide at a speed of 600 rpm for 30 seconds. The photoresist layer on the glass slide was then placed underneath the ROE in the region where all five beams interfered. The sample was exposed to the interfering beams for a typical time of 1.2 seconds at a laser power of 200 mW. When a batch of the photoresist with half the rose bengal concentration was used, the power was increased to 260 mW. After exposure, the samples were developed in PGMEA for 3 minutes, followed by a rinse in isopropanol for one minute, and then air dried.

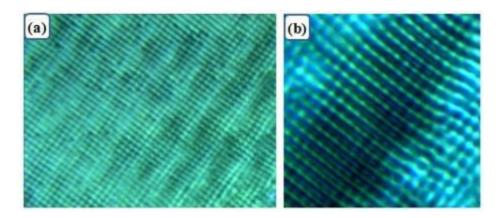


Figure 5.4. (a) Optical microscope image (40X) of 3D photonic crystal template in DPHPA fabricated using single silicon based reflective optical element. (b) Optical microscope image of close-up of an area of 3D photonic crystal template.

Figure 5.4(a) shows an image taken from a CCD camera mounted on an optical microscope of the 3D photonic crystal formed from the exposure of the DPHPA mixture to the five beam interference pattern created by the single beam and single reflective optical element. A grid pattern can clearly be seen. In Figure 5.4(b), another optical microscope image shows a

close-up of an area of the sample where the 3D structure is visible. The next layer of the woodpile structure can be seen underneath the top layer in the darker region in the middle.

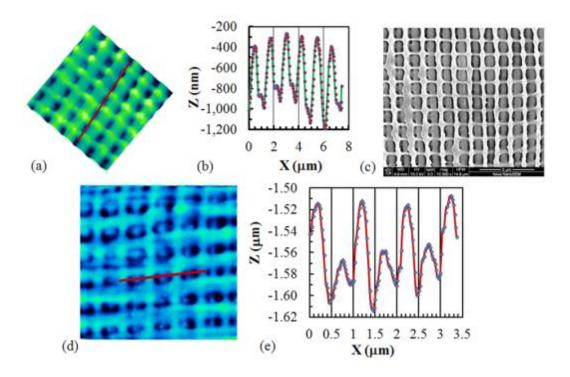


Figure 5.5. (a) AFM image of holographically fabricated 3D photonic crystal template in DPHPA with incident angle of 78°; (b) Surface profile measured along the red line in (a); (c) SEM image of woodpile-like structure in photonic crystal template in DPHPA with incident angle of 78°; (d) AFM image of photonic crystal template in DPHPA with incident angle of 74.9°; (e) Plot of surface profile measured

In Figure 5.5(a), an atomic force microscope (AFM) image of the 3D photonic crystal template formed with an incident angle of 78° shows the grid pattern that has developed in the photoresist. It looks similar to the simulated image of the woodpile structure, as seen in Figure 5.2(b). Figure 5.5(b) shows a plot of the surface profile along the red line in the AFM image. From the surface profile, the lattice period along the red line is found to be 1.232 microns. The scanning electron microscope (SEM) image in Figure 5.5(c) shows the woodpile-type structure

in greater detail than the AFM image. Based on the scale bar in the lower right of the image, the lattice period is measured to be 1.239 microns. Both measurements of the lattice period are in good agreement with a theoretical calculation of 1.248 microns, using the incident angle of 78°.

The multi-beam interference with a 78° incident angle (which is close to the Brewster angle) can only generate tetragonal photonic crystals.[142] In order to improve the crystal symmetry, thus increasing the photonic bandgap size, the incident angle needs to be changed. For the incident angle of 54.7°, the interfering angle between side beam and central beam is 70.5°; thus, a face-centered cubic crystal can be generated. When the incident angle is decreased from 78° to 54.7°, the reflectance for p-polarized beam is increased from 0.25% to 18% and for s-polarized beam the reflectance is decreased from 81% to 60%. The interference patterns are still dominated by the interference between the central, circularly-polarized beam and the side, s-polarized beam. However, a deviation from the ideal p-polarization will influence the symmetry of the PhC and the motif in the unit cell of the PhC. When the incident angle is decreased, the lattice constant c/a (c and a are lattice constant in the z and x-directions, respectively) will change.[142] A compromise among the crystal symmetry, the beam intensity ratio and the beam polarization can be made by a comprehensive calculation of bandgap sizes in various formed structures.

To demonstrate the incident angle reconfiguration, we added a piece of glass slide with a thickness of 1 mm under the silicon chips on the bottom edge of the PDMS mold in Figure 5.1(c). The incident angle was changed from 78° to 74.9°. Figure 5.5(d) shows an AFM image of a 3D photonic crystal template fabricated in DPHPA using the reconfigured reflective optical

element with a similar experimental condition to the templates fabricated using an incident angle of 78°. A woodpile-like structure can be seen. A plot of the surface profile along the red line in the AFM image in Figure 5.5(d) is shown in Figure 5.5(e). The lattice period in x-direction is measured to be 1.023 micron from the surface profile, which agrees with the theoretical value of 1.024 microns. The symmetry of the crystal is more easily observed because the AFM tip can get more information of structures in the z-direction when the lattice constant in the z-direction is decreased.

Using the top-cut prism, all five beams have the same intensity assuming the incident beam is uniform. [102,143] With the single silicon based reflective optical element we fabricated, the ratio of the central beam intensity to the side beam intensity is around 2.5. The intensity contrast in the interference pattern is improved comparing the current optical element with the top-cut prism (the best ratio is 4 for the five-beam interference).[144] The improved intensity contrast can help remove unpolymerized monomers out of the 3D polymerized interconnected structures during the development process.

#### CHAPTER 6

# DIGITALLY TUNABLE HOLOGRAPHIC LITHOGRAPHY USING A SPATIAL

# LIGHT MODULATOR AS A PROGRAMMABLE PHASE MASK<sup>2</sup>

A geometric, grayscale phase pattern displayed on the SLM was used to demonstrate the digital assignment of phase to diffracted beams. The relationship between the gray levels in the phase pattern displayed on the SLM and the phases of the individual beams was calculated. The validity of this relationship was tested by observing the change in structure in holographically fabricated compound photonic crystal templates, and comparing them to simulations of interfering beams with the assigned phases. This phase assignment method can be used to holographically produce simple spatially varying structures, which will be discussed in later chapters.

#### 6.1 Experimental Setup

The experimental setup used for all SLM results to follow is shown in Figure 6.1. A 532 nm laser beam (Cobolt Samba 50mW) is expanded and collimated before fully illuminating a phase-only SLM (Holoeye PLUTO) at an angle of 5 degrees (exaggerated in the figure for visibility). The SLM has an area of 1920x1080 pixels with an 8  $\mu$ m pixel pitch and 87% fill factor, and has a total phase retardation of  $2\pi$  across 256 gray levels. The gray levels on the SLM

<sup>&</sup>lt;sup>2</sup> Parts of this chapter have been previously published, either in part or in full, from J. Lutkenhaus, D. George, M. Moazzezi, U. Philipose, and Y. Lin, "Digitally tunable holographic lithography using a spatial light modulator as a programmable phase mask," Opt. Express 21, 26227-26235 (2013), and J. Lutkenhaus, D. George, B. Arigong, H. Zhang, U. Philipose, and Y. Lin, "Holographic fabrication of photonic crystal templates using spatial-light-modulator-based phase mask method," Proc. SPIE 8974, Advanced Fabrication Technologies for Micro/Nano Optics and Photonics VII, 897419 (2014). Reproduced with permission from OSA Publishing and from SPIE Publications.

correspond to a given phase retardation based on the gamma curve used. We used a linear gamma curve that converted gray levels from 0 to 255 to a phase level of 0 to  $2\pi$ , respectively.

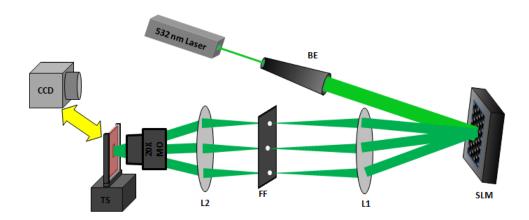


Figure 6.1. Diagram of experimental setup for the use of the SLM for holographic lithography. BE: Beam Expander, SLM: Spatial Light Modulator, L1: 1st lens (f1 = 400mm), FF: Fourier Filter, L2: 2nd lens (f2 = 200mm), MO: 20X Microscope Objective lens, TS: Translation Stage, CCD: USB camera. The CCD and sample stage were interchangeable upon the translation stage.

A geometric hexagonal phase pattern is displayed on the SLM and diffracts the single incident laser beam into multiple beams. The diffracted beams are then individually focused by the first lens (r = 50.8mm, f1 = 400mm), which is located one focal length from the SLM. At the Fourier plane, or the 2f point, located one focal length from the first lens, lies the Fourier filter, which blocks the zero order and 2nd and higher order beams, and allows passage of the 1st order beams. Located a distance f2 = 200mm from the Fourier plane is the second lens of the same radius as the first lens, with focal length f2. The interfering angle of the beams after the second lens is 1.83 degrees. The two lenses constitute a 4f imaging system. The second lens focuses all remaining beams into the microscope objective lens (20X), placed inside the focal

length of the second lens, which further de-magnifies the interference pattern and also serves to increase the interfering angle between the beams. Mounted upon the translation stage is a sample stage, which is located at the point where all desired, generated beams interfere. The sample stage was interchangeable with a CCD USB camera, which allowed digital capture of the interference pattern image at the focal plane.

# 6.2 Phase Pattern Design

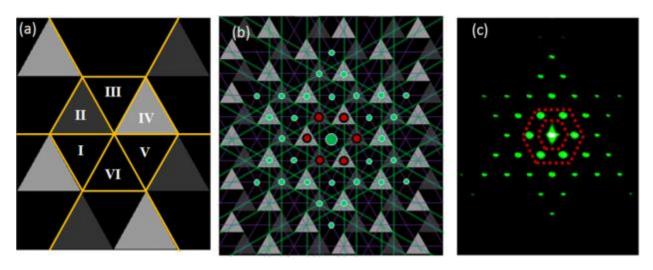


Figure 6.2. (a) A tile unit of the phase pattern displayed on the SLM. The orange lines are drawn on the pattern to assist in the viewing of the hexagons and the triangles (I thru VI) in the hexagons. The gray levels of the triangles are set digitally. (b) Enlarged view of phase pattern with a scheme showing diffraction directions and spots. (c) Photograph of diffraction pattern in Fourier plane (2f point) taken with a USB CCD camera. Diffraction spots in between the dotted red lines are the 1st order diffracted beams.

An enlarged portion of the hexagonal phase pattern is shown in Figure 6.2(a), with each hexagon consisting of six equilateral triangles. The triangles are created by drawing lines from the center of the hexagon to its vertices. The gray levels of the triangles in Figure 6.2(a) are: 0

for the black triangles, 51 for the dark gray triangles, and 153 for the light gray triangles. Each triangle in the hexagon can be digitally set to a different gray level. The length of each side of a triangle was designed to be 0.706mm at 100% zoom on the SLM display. This pattern was tiled using the native SLM software, and then zoomed to 3.12% of the size of the pattern originally displayed, making the triangle side length 22.0 $\mu$ m. The side length of the triangles is not necessary to be an integral number of the pixel pitch. The length of 22  $\mu$ m was chosen because that's the minimum value for the first-order diffracted beams to pass through the 4f image system, due to the diameter of the lenses used in the optical setup.

In Figure 6.2(b), the directions of diffraction of a laser beam incident on the SLM when the phase pattern is displayed are indicated by the thin green and purple lines. The green lines indicate diffractions that are due to periodic arrangements of dark gray, black, dark gray, black, or light gray, black, light gray, black, in the vertical direction and also in directions rotated ±60 degrees from the vertical. The purple lines indicate diffraction due to periodic arrangements of light gray, black, dark gray, light gray, black, dark gray. Where 3 lines of identical color intersect indicates the location of a diffraction spot in the Fourier plane. The large green dot in the center of Figure 6.2(b) represents the zero-order beam, the red dots surrounding it represent the 1st order beams, and all other dots indicate the location of higher order beams.

The pattern of diffraction spots in Figure 6.2(b) looks very similar to the one in Figure 6.2(c), which shows a CCD image of the diffraction pattern after the 1st lens at the 2f point (Fourier plane). The large diffraction spot in the center of the inner dotted red line overlaid upon the image is the zero-order beam. The diffraction spots located in between the inner and outer dotted red lines in Figure 6.2(c) are the diffracted 1st order beams. All diffraction spots

outside the outer dotted red line are higher order beams. A calculation of the side length of the triangles in the pattern from the diffraction pattern reveals a side length of 22.1 $\mu$ m, which agrees with the designed value.

#### 6.3 Determination of the Phases of the Diffracted Beams

In Figure 6.3(a), a slightly enlarged view of the pattern in Figure 6.2(a) is shown with a hexagonal unit cell overlaid upon it in orange, and the first order beams from Figure 6.2(b) displayed as green circles. Given the agreement between the observed and predicted diffraction patterns, we can begin to make predictions about the phases. The phase of each first order beam is determined by the average gray level inside the corresponding kite-shaped region. The phase of beam 1, for example, is determined by the gray level of the red, highlighted kite, which is shown in detail in Figure 6.3(b). The phase of beam 1 is given by

$$\delta_1 = \frac{2\pi}{255} \left( \frac{1}{3} light \ gray + \frac{8}{18} black + \frac{1}{18} black + \frac{1}{6} black \right) \tag{6.1}$$

Similarly, the phase of beam 2 is given by

$$\delta_1 = \frac{2\pi}{255} \left( \frac{1}{3} dark \ gray + \frac{8}{18} black + \frac{1}{18} black + \frac{1}{6} black \right) \tag{6.2}$$

As can be determined from Figure 6.3(b), beams 3 and 5 have phases equal to the phase of beam 1, and beams 4 and 6 have phases equal to the phase of beam 2. This is due to the average gray levels being the same. Since the gray level of black is zero, the black triangles do not contribute to the average gray level of the kites, and the phases of the beams are determined only by the gray levels of triangles II and IV from Figure 6.2(a). It should be noted that this is a special case and a more general use of Eqs. (6.1)and (6.2) will be discussed later in this chapter.

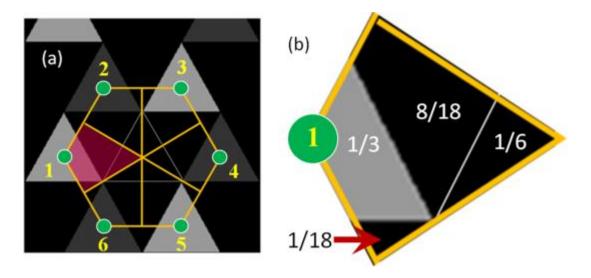


Figure 6.3. (a) Enlarged view of the pattern from Figure 6.2(a) with hexagonal unit cell overlaid in orange. Green circles indicate the beams diffracted from the pattern on the SLM. (b) Close-up of red-highlighted kite-shaped region in (a). The phases of the beams are determined by the average of the gray levels in each kite-shaped region.

In references 118-119, it was shown that six interfering beams generated from a SLM form rotationally and translationally symmetric interference patterns. To study how the gray levels of the triangles affect the phases of the beams, a beam configuration was chosen that produced interference patterns with easily visible changes due to the phase. A four-beam configuration is capable of holographically producing dual lattice structures that are visibly altered due to phase changes. By blocking beams 2 and 6 with the Fourier filter, the beam configuration needed to produce the dual lattice structures was generated. Where the four beams overlap after being focused by the second lens and passing through the microscope objective lens, there is an interference pattern at the sample plane with an intensity profile given by

$$I(r) = I_0 + \Delta I(r) = \langle \sum_{i=1}^{4} E_i^2(r,t) \rangle + \sum_{i < j}^{4} E_i \cdot E_j \cos[(k_i - k_j) \cdot r + (\delta_i - \delta_j)]$$
 (6.3)

Isolating and expanding the sum in the second term on the right hand side of the equation,

$$\Delta I(r) = E_{1}E_{3}e_{1} \cdot e_{3} \cos \left[ 2\pi \left( \frac{3}{\alpha} i - \frac{1}{\beta} j \right) (x+y) + (\delta_{3} - \delta_{1}) \right]$$

$$+ E_{1}E_{4}e_{1} \cdot e_{4} \cos \left[ 2\pi \left( \frac{4}{\alpha} i \right) (x+y) + (\delta_{4} - \delta_{1}) \right]$$

$$+ E_{1}E_{5}e_{1} \cdot e_{5} \cos \left[ 2\pi \left( \frac{3}{\alpha} i + \frac{1}{\beta} j \right) (x+y) + (\delta_{5} - \delta_{1}) \right]$$

$$+ E_{3}E_{4}e_{3} \cdot e_{4} \cos \left[ 2\pi \left( \frac{1}{\alpha} i + \frac{1}{\beta} j \right) (x+y) + (\delta_{4} - \delta_{3}) \right]$$

$$+ E_{3}E_{5}e_{3} \cdot e_{5} \cos \left[ 2\pi \left( \frac{2}{\beta} j \right) (x+y) + (\delta_{5} - \delta_{3}) \right]$$

$$+ E_{4}E_{5}e_{4} \cdot e_{5} \cos \left[ 2\pi \left( \frac{1}{\alpha} i - \frac{1}{\beta} j \right) (x+y) + (\delta_{5} - \delta_{4}) \right]$$

where  $\alpha$  and  $\beta$  are lattice constants of the interference pattern in the x and y directions, respectively, and  $\delta$ i is the phase given by Eqs. (6.1) and (6.2). Since beams 1, 3, and 5 have the same phase, and beams 2 and 6 are blocked, the only beam that has a different phase is beam 4, whose phase is determined only by the dark gray triangles. Thus, changing the gray level of the dark gray triangles (triangle IV in Figure 6.2(a)) should produce changes in the interference pattern.

In Figure 6.4, the pattern shifts due to the phase shift in beam 4 are explored. In Figure 6.4(a1), beam 4 has the same phase as beams 1, 3, and 5, with the triangle containing beam 4

having a gray level of 153. For Figure 6.4(a2) and (a3), the gray levels of the triangles containing beam 4 are 102 and 51, respectively. Simulations of the four beam interference patterns with the phases of the beams defined according to Eqs. (6.1) and (6.2) using the gray levels of the phase patterns in Figure 6.4(a1), (a2), (a3) are shown in Figure 6.4(b1), (b2), (b3), respectively.

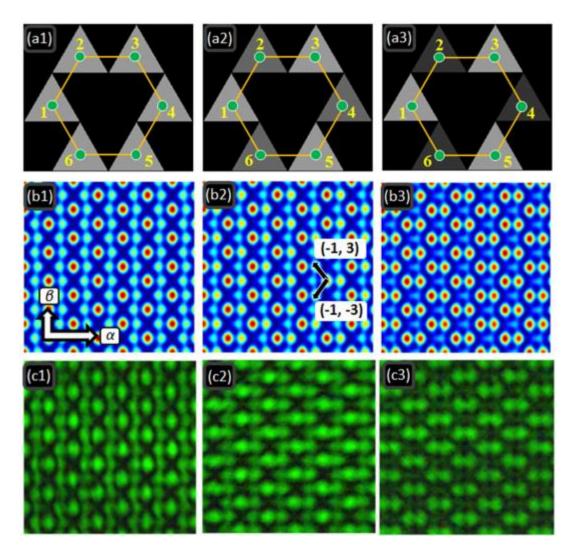


Figure 6.4. (a1, a2, a3) Hexagonal phase patterns with unit cell drawn in orange, and gray level of 153 for all gray triangles contributing to beam phases. (a2) Phase pattern with 102 gray level for dark gray triangles. (a3) Phase pattern with 51 gray level for dark gray triangles. (b1, b2, b3) Simulated four beam interference patterns for the beams with phases determined by the phase

patterns in (a1, a2, a3), respectively.  $\alpha$  and  $\beta$  in (b1) designate the lattice constants. In (b2), the black arrows show the direction that the pattern shifts due to the change in phase. (c1, c2, c3) are CCD images of the four beam interference patterns captured after the microscope objective lens, as shown in the diagram in Figure 6.1.

The shift in the intensity pattern caused by the phase shift in beam 4 is given by

$$\Delta I_4 = E_1 E_4 e_1 \cdot e_4 \cos \left[ 2\pi \left( \frac{4}{\alpha} i \right) (x+y) - m\pi \right]$$

$$+ E_3 E_4 e_3 \cdot e_4 \cos \left[ 2\pi \left( \frac{1}{\alpha} i + \frac{1}{\beta} j \right) (x+y) - m\pi \right]$$

$$+ E_4 E_5 e_4 \cdot e_5 \cos \left[ 2\pi \left( \frac{1}{\alpha} i - \frac{1}{\beta} j \right) (x+y) - m\pi \right]$$

$$= E_1 E_4 e_1 \cdot e_4 \cos \left[ 2\pi \left( \frac{4}{\alpha} i \right) (x+y-m\left( -\frac{1}{8}\alpha \pm \frac{3}{8}\beta \right) \right) \right]$$

$$+ E_3 E_4 e_3 \cdot e_4 \cos \left[ 2\pi \left( \frac{1}{\alpha} i + \frac{1}{\beta} j \right) (x+y-m\left( -\frac{1}{8}\alpha - \frac{3}{8}\beta \right) \right) \right]$$

$$+ E_4 E_5 e_4 \cdot e_5 \cos \left[ 2\pi \left( \frac{1}{\alpha} i - \frac{1}{\beta} j \right) (x+y-m\left( -\frac{1}{8}\alpha + \frac{3}{8}\beta \right) \right) \right]$$

, where  $m=(\delta_i-\delta_j)/\pi$ . From Eqs. (6.1) and (6.2) and the expression for m, we find that the relative phase shift in beam 4 for the phase pattern in Figure 6.4(a2) is  $0.13\pi$  and for the one in Figure 6.4(a3) is  $0.27\pi$ . The lattice constants,  $\alpha$  and  $\beta$ , are shown in Figure 6.4(b1). Based on Eq. (6.5), the pattern shifts in the (-1, +3) or (-1,-3) directions when the phase of beam 4 is changed. This is seen in the simulations in Figure 6.4(b1), (b2), (b3), and also in the corresponding recorded CCD images shown in Figure 6.4(c1), (c2), (c3). The structures in the simulations and the CCD images change from a fenced-in cylinders pattern to weakly linked dumbbells when the gray level of the triangles changes. The CCD images agree closely with the simulations, with the

change in the interference pattern clearly visible with the change in the gray level of the triangles, validating this method of controlling the phase of generated beams by use of the SLM as a phase mask.

#### 6.4 Holographic Fabrication

To demonstrate this method of phase assignment to generated beams, we holographically fabricated photonic crystal templates in a photoresist using the phase pattern in Figure 6.4(a1). The photoresist mixture was made from the following components in the specified weight concentrations: dipentaerythritol penta/hexaacrylate (DPHPA) monomer (Aldrich, 90.36%); rose bengal photo-initiator (0.11%); N-phenyl glycine co-initiator (0.65%); and N-vinyl pyrrolidinone (8.88%), a chain extender. The photoresist mixture was spin-coated onto a glass slide at a speed of 3000rpm for 30 seconds, resulting in a film thickness of approximately 3.17µm. The glass slide with photoresist thin-film was then placed on the sample stage after the microscope objective lens (Figure 6.1), and exposed to the interference pattern for 2 seconds. The sample was then immersed in propylene glycol methyl ether acetate (PGMEA) developer for 3 minutes, rinsed with isopropanol, and then allowed to air dry.

Figure 6.5(a) shows an image recorded from a CCD camera mounted on an optical microscope of a 2D compound photonic crystal template formed from the exposure of DPHPA to the interference pattern in Figure 6.4(b1, c1). A scanning electron microscope (SEM) image of another sample holographically fabricated in DPHPA using the phase pattern in Figure 6.4(a1) is shown in Figure 6.5(b), and a close up view of that SEM image is shown in the SEM image in Figure 6.5(c). In Figure 6.5(a, b, c), the fenced-in cylinder structure from Figure 6.4(b1, c1) is clearly visible. An atomic force microscope (AFM) image of the fabricated structures is shown in

Figure 6.5(d), with the orange line indicating the location of the surface profile shown in Figure 6.5(e). The lattice period according to the surface profile along the orange line is  $4.07\mu m$ , which matches closely with a theoretical calculation of  $4.06\mu m$ 

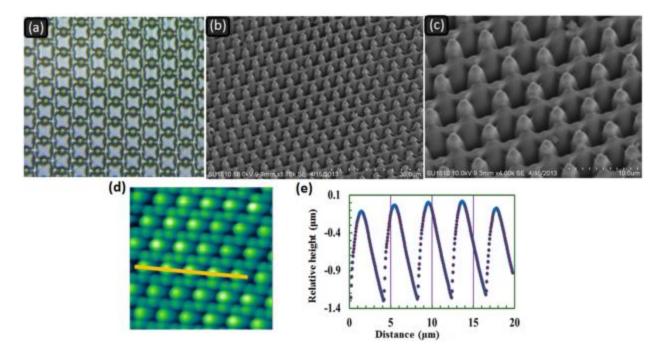


Figure 6.5. (a) Optical microscope image (40X) of 2D photonic crystal template in DPHPA, holographically fabricated using the phase pattern in Figure 6.4(a1) displayed on the SLM. (b) SEM image of fenced-in cylinder structures fabricated in DPHPA. (c) Close-up view from the sample seen in the SEM image in (b). (d) AFM image of photonic crystal template in DPHPA. (e) Plot of surface profile along orange line in (d).

#### 6.5 Further Discussion

In previous sections, the phase pattern used was relatively simple, since only two triangles in the base hexagon shown in Figure 6.2(a) were not black. A more complicated case would be a hexagonal phase pattern with all of the triangles set to different gray levels. In

Figure 6.6(a), a tile unit of a phase pattern is shown with the gray levels of the triangles in the hexagon set to 255, 202, 150, 99, 49, and 0, for triangles I-VI, respectively.

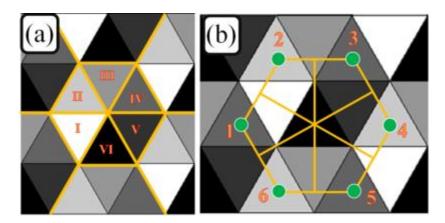


Figure 6.6. (a) Tile unit of a phase pattern with triangles (I-VI) all set to different gray levels. (b) Enlarged view of the pattern from (a) with hexagonal unit cell overlaid in orange. Green circles indicate the beams diffracted from the pattern on the SLM.

Figure 6.6(b) shows the hexagonal unit cell overlaid in orange on the pattern. The phases for the beams are, again, determined by the average of the gray levels inside the orange outlined kite-shaped regions, given by the equations,

$$\delta_1 = \frac{2\pi}{255} \left( \frac{1}{3} (IV) + \frac{8}{18} (I) + \frac{1}{18} (V) + \frac{1}{6} (VI) \right)$$
 (6.6)

$$\delta_2 = \frac{2\pi}{255} \left( \frac{1}{3} (II) + \frac{8}{18} (I) + \frac{1}{18} (III) + \frac{1}{6} (VI) \right)$$
 (6.7)

$$\delta_3 = \frac{2\pi}{255} \left( \frac{1}{3} (IV) + \frac{8}{18} (V) + \frac{1}{18} (III) + \frac{1}{6} (VI) \right)$$
 (6.8)

$$\delta_4 = \frac{2\pi}{255} \left( \frac{1}{3} (II) + \frac{8}{18} (V) + \frac{1}{18} (I) + \frac{1}{6} (VI) \right)$$
 (6.9)

$$\delta_5 = \frac{2\pi}{255} \left( \frac{1}{3} (IV) + \frac{8}{18} (III) + \frac{1}{18} (I) + \frac{1}{6} (VI) \right)$$
 (6.10)

$$\delta_6 = \frac{2\pi}{255} \left( \frac{1}{3} (II) + \frac{8}{18} (III) + \frac{1}{18} (V) + \frac{1}{6} (VI) \right)$$
 (6.11)

where the Roman numerals indicate the gray level of the corresponding triangle in Figure 6.6(a). Figure 6.7(a) shows a simulated four beam interference pattern using beams 1, 3, 4, and 5 with phases of  $1.17\pi$ ,  $0.49\pi$ ,  $0.81\pi$ ,  $0.89\pi$ , respectively, determined using Eqs. (6.6)-(6.11) for the phase pattern in Figure 6.6(a). A recorded CCD image of the four beam interference pattern is shown in Figure 6.7(b), and an SEM image of the 2D holographically fabricated photonic crystal template in DPHPA is shown in Figure 6.7(c). The simulation, CCD and SEM images all agree very closely, with the dual lattice structures clearly visible in all three images, further validating this method.

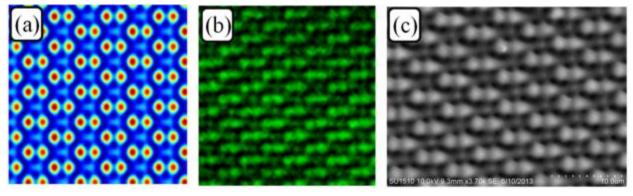


Figure 6.7. (a) Simulated four beam interference pattern for beams (1, 3, 4, 5) from Figure 6.6(b) generated by the phase pattern in Figure 6.6 (a) with phases determined by Eqs.(6.6)-(6.11). (b) CCD image of four beam interference pattern generated with the phase pattern in (a). (c) SEM image of holographically fabricated 2D photonic crystal templates.

This method of controlling the phase of generated beams is similar to the use of computer-generated holograms with a SLM, but while the generation of an arbitrary number of 1st order beams is not impossible, it is not practical. Computer generated phase holograms displayed on SLMs have proven successful in generating non-diffracting beams [119,] and

multiple beam interference patterns with up to 32-fold symmetry. [118,122,145] However, the strength of pixelating the phase pattern into triangles is that the gray levels of triangles in specific locations in the overall pattern can be changed to different values than the rest of the pattern, creating spatial variations in the phase. The spatially varying phase pattern can be used to fabricate photonic crystal templates that contain local variations in the filling fraction, and subsequently, the effective refractive index.

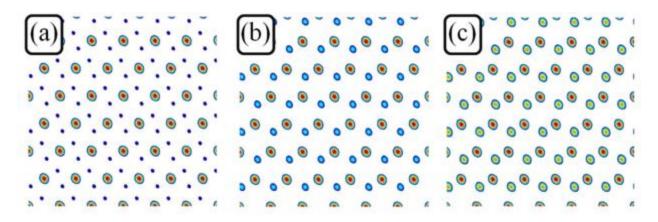


Figure 6.8. (a, b, c) Simulated four-beam interference patterns formed from beams 1, 3, 4, and 5, with phases of the beams assigned by the gray levels in the phase patterns in Figure 6.4(a1, a2, a3), respectively.

Figure 6.8 (a), (b), and (c) show simulated four-beam interference patterns formed by beams 1, 3, 4 and 5 with phases assignments from the gray levels shown in Figure 6.4 (a1, a2, a3), respectively. The patterns were obtained by setting the iso-intensity surface to be half of the maximum intensity. If a negative photoresist is exposed to these interference patterns, the high intensity region becomes polymerized. The filling fractions of dielectric materials versus the whole volume are 0.123, 0.143, and 0.176 in the patterns of Figure 6.8 (a), (b), and (c), respectively. The effective refractive index is 1.09, 1.11, and 1.13, respectively, assuming a

refractive index of 1.6 for DPHPA. By spatially varying the filling fraction and consequently the effective refractive index, gradient index devices can be fabricated [128,137,146-147].

#### CHAPTER 7

# HOLOGRAPHIC FABRICATION OF FUNCTIONALLY GRADED PHOTONIC LATTICES THROUGH SPATIALLY SPECIFIED PHASE PATTERNS<sup>3</sup>

#### 7.1 Background Phase Pattern

A detail design of the background phase pattern consisting of hexagons is enlarged and shown in Figure 7.1(a), which is an expanded view of the phase pattern in Figure 6.6(a). The gray levels of six equilateral triangles inside the hexagon are assigned to be 0, 51, 102, 153, 204, and 255, with 0 at the bottom and increasing by 51 in the counterclockwise direction. Figure 7.1(b) shows a diffraction pattern at the Fourier plane of the laser beams by the phase pattern on the SLM. The pattern was recorded by a CCD camera. Surrounding the 0th-order diffraction in the center, the six first-order diffractions (labeled 1, 2, 3, 4, 5, and 6) form a pattern that has a hexagonal symmetry as shown in Figure 7.1(b). These diffractions were formed due to the periodic arrangements of triangles in the vertical direction and in directions rotated from the vertical direction by ±60° 33, and are shown as white circles in Figure 7.1(a). The orientation of diffraction patterns in Figure 7.1(b) can be explained by the red hexagon in Figure 7.1(a), where the labels 1–6 correspond to the numerical labels in the diffraction pattern, respectively. The phases of these diffracted beams were determined by the gray levels inside the unit cell, indicated as a red hexagon in Figure 7.1(a) [89,128]. The hexagon was divided into six equal areas, and each area formed a kite-type four-sided polygon with the same area as a triangle in

<sup>&</sup>lt;sup>3</sup> Parts of this chapter have been previously published, either in part or in full, from J. Lutkenhaus, D. George, B. Arigong, H. Zhang, U. Philipose, and Y. Lin, "Holographic fabrication of functionally graded photonic lattices through spatially specified phase patterns," Appl. Opt. 53, 2548-2555 (2014). Reproduced with permission from OSA Publishing.

the figure. The phases of first-order diffracted beams located at the head of each kite were determined by the average gray level covered by the kite according to Eqs. (6.6)-(6.11).

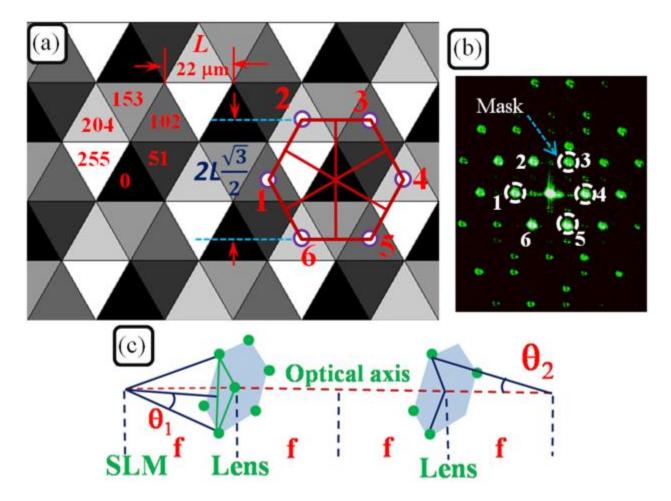


Figure 7.1. (a) Detailed schematic of background phase pattern displayed on the SLM. (b) CCD image of Fourier plane diffraction pattern from the laser diffracting from the phase pattern in (a) displayed on the SLM. (c) Diagram of 4f setup showing diffraction angles ( $\theta_1$ ) and interference angles ( $\theta_2$ ).

The average gray levels that determine the phase for beam 3, 4, 5, and 6 can be calculated with Eq. (6.6-(6.11). Using a linear gamma curve, a gray level of 0 is converted to a phase of  $0\pi$  and a gray level of 255 to a phase of  $2\pi$ . Digital potentiometer values of 2.38 and 1.36 V were used for the SLM's bright and dark voltages, respectively. The relative phases of

beams from 1 to 6 are therefore  $1.18\pi$ ,  $1.49\pi$ ,  $0.49\pi$ ,  $0.89\pi$ , and  $1.07\pi$ , respectively. A Fourier filter blocked all other beams while allowing only beams 1, 3, 4, and 5 to pass through, as shown in Figure 7.1(b). After going through the Fourier filter, these four beams (1, 3, 4, and 5) form an interference pattern where the beam intensity I(r) is determined by Eq. (6.3).

#### 7.2 Missing Lattices in Periodic Photonic Lattices

The simulated interference pattern is shown in Figure 7.2(a). In the simulation, the same linear polarization as the laser beam was used. It should be noted that the Fourier filtering effect on the trench boundary was not included in the simulation. The cross section of the simulated intensity profile shows sharp trench boundaries while the atomic force microscope image in Figure 7.2(c) shows noticeable effects around the trench boundaries. The lattice constant  $\Lambda$  in Figure 7.2(a) is related to the side length L of the equilateral triangle in Figure 7.1(a), as calculated in Eqs.(7.1)-(7.4). As shown in Figure 7.1(c), the Bragg diffraction due to the periodic structures in vertical direction can be written as in the following equation:

$$\lambda = (2L) \left(\frac{\sqrt{3}}{2}\right) \sin \theta_1 \tag{7.1}$$

where  $\lambda$  is the laser wavelength and  $\theta_1$  the diffraction angle. Assuming the same focal length f in 4f imaging system, the interference angle  $\theta_2$  [as shown in Figure 7.1(c)] relative to the zero-order diffraction direction passing through the center of hexagon in Figure 7.1(a) is determined by:

$$\sin \theta_2 = f \sin \theta_1 / \left(\frac{\sqrt{3}}{2}\right) / f \tag{7.2}$$

The lattice constant  $\Lambda$  in Figure 7.2(a) in the interference pattern due to the four-beam interference is determined by:

$$\Lambda = \frac{\lambda}{\sin \theta_2 \sin 60} = \frac{\lambda}{\left(\left(\frac{\sqrt{3}}{2}\right) \sin \theta_2\right)} = L\sqrt{3}$$
(7.3)

After considering the magnification due to the 4f image system and objective lens, the lattice constant  $\Lambda$  in the interference pattern is related to the side length L of the equilateral triangle by:

$$\Lambda = \frac{L\sqrt{3}}{demagnification \ of \ 4f \ imaging \ system \ and \ microscope \ objective \ lens} \tag{7.4}$$

The interference pattern was recorded in a photoresist. The photoresist was photosensitized to 532 nm by preparing a mixture with the following components in the specified weight concentrations: dipentaerythritol penta/hexaacrylate (DPHPA) monomer (Aldrich, 90.36%), a photo initiator rose bengal (0.11%), co-initiator N- phenyl glycine (NPG, 0.65%), and chain extender N-vinyl pyrrolidinone (NVP, 8.88%). The mixture was spin-coated on a glass slide with a speed of 3000 rpm for 30 seconds. The exposed sample was developed in PGMEA for 3 minutes, rinsed by isopropanol for one minute and left to dry in air.

A gray level of 0 (zero) was assigned to the dark line in the phase pattern in Figure 7.2(a). In the first-order diffracted beam containing the spatial frequency information of the dark line [see Figure 7.1(b)], the direction of the diffractions is off axis by an angle of  $\theta_1 = 0.8^{\circ}$ . As a result, the amplitude patterns associated with each first-order diffracted beam are shifted in spatial frequency from the origin by an amount of  $\sin \theta_1 / \lambda = 1/(2L \sin 60^{\circ})$ , as calculated by Eq. (7.1).  $\sin \theta_1 / \lambda$  is calculated to be 26.2 mm<sup>-1</sup>. Thus, each off-axis beam creates a unique complex electric field. The electric field amplitude for each beam is then the magnitude of the complex electric field.

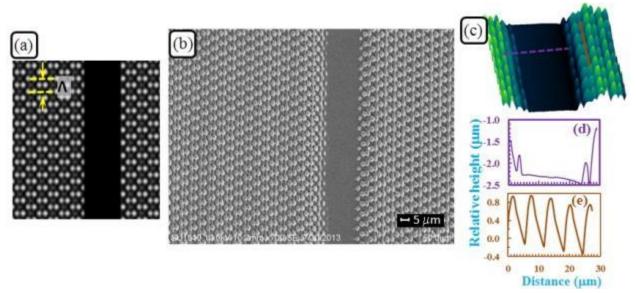


Figure 7.2. (a) Simulated interference pattern with missing lattice line defect (dark line). (b) SEM image of holographically fabricated structures in DPHPA photoresist with the designed missing lattice line defect. (c) AFM image of the missing lattice line in the fabricated structures. (d) AFM profile along the purple line crossing the dark line defect. (e) AFM profile along the orange line running parallel to the dark line defect.

Figure 7.2 (b) shows an SEM image of the fabricated missing-lattice (dark line) photonic structures. The photoresist was exposed to the interference pattern for a typical exposure time of 2 seconds. The fabricated photonic structures look very similar to the simulated pattern in Figure 7.2 (a). Figure 7.2 (c) shows an atomic force microscope (AFM) image of the fabricated dark lines (missing lattice region). The lattice position or periodicity of these structures in close proximity to the dark line remains unchanged. However, the projected dark line has a noticeable effect on the photonic crystal motifs immediately surrounding the dark lines. Based on the designed structural parameters in Figure 7.1 and Figure 7.2(a), the width of the dark line is 4.91 L. For the dark line, the image will be demagnified only by the 4f lens system and the objective lens. Based on Eq. (7.4), the period  $\Lambda$  of interference pattern is modified by  $\sqrt{3}$ 

besides the demagnification by the 4f lens system and the objective. Thus, we predict that the ratio of the width of dark line over the period  $\Lambda$  of interference pattern in Figure 7.2(a) and Figure 7.2(b) can be calculated by  $4.91L/(\sqrt{3}) = 2.86$ . Figure 7.2(d) and Figure 7.2(e) are AFM profiles measured along the purple and orange lines, respectively. The width of the dark line is measured to 18.46  $\mu$ m, and the lattice period  $\Lambda$  is 6.26  $\mu$ m. Thus the ratio of the width of dark line over  $\Lambda$  is measured to be 2.95, which is close to the predicted value of 2.86.

If the Oth-order diffracted beam is allowed to pass through the Fourier filter and interfere with these four first-order diffracted beams, 3D photonic structures and a positive defect line will be formed. However, SU-8 photoresist [148] should be used for the fabrication of 3D structures instead of using DPHPA. If a positive defect line is formed inside the 3D photonic crystal, the defect line can function as a waveguide, and optical transmission along the waveguide can be measured.

#### 7.3 Embedding Single Motif Lattices in Dual Lattice Photonic Structures

In this section, the SLM was used as a spatially variant phase mask for the holographic fabrication of spatially graded photonic lattices. Figure 7.3(a) shows an enlarged view of a spatially specified phase pattern for the above purpose. The phase pattern has a unit cell (or pixel) of hexagon, as shown in Figure 7.3(b1). The hexagon consists of six equilateral triangles with gray levels of 153, 5, 51, 5, 5, and 5 in a clockwise direction with 153 at the top right. The majority of the phase pattern was formed by such hexagons. The spatially variant phase pattern was produced by embedding 33 hexagon pixels with gray levels 153, 5, 153, 5, 5, and 5 in a clockwise direction with 153 at the top right and bottom right. The designed phase patterns can generate six first order diffracted beams. The phase of the diffracted beams is determined by

the average gray level of kites inside the hexagon, as shown in Figure 7.3(b2). In Figure 7.3(b2), the triangles with a gray level of 5 are not shown for the purpose of neatness. For the majority of the phase pattern, the phase of diffracted beams 1, 3, and 5 is determined by Eq. (7.5), while for diffracted beam 2, 4, and 6, it is determined by Eq. (7.6):

$$\left(\frac{1}{3} \times 51 + \frac{8}{18} \times 5 + \frac{1}{18} \times 5 + \frac{1}{6} \times 5\right) \times \frac{2\pi}{255}$$
 (7.5)

$$\left(\frac{1}{3} \times 153 + \frac{8}{18} \times 5 + \frac{1}{18} \times 5 + \frac{1}{6} \times 5\right) \times \frac{2\pi}{255}$$
 (7.6)

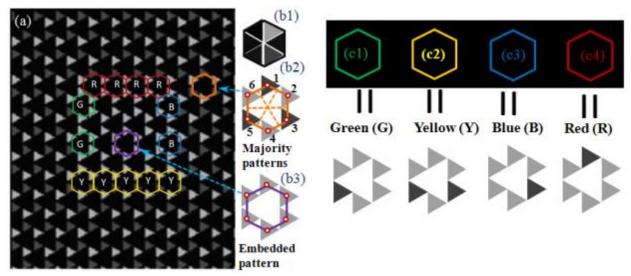


Figure 7.3. (a) Enlarged view of embedded phase pattern in the majority phase pattern for single lattice defects in dual-lattice bulk structure. The red, green, blue, and yellow hexagons represent the boundary of the defect region. (b1) Basic hexagonal unit cell with different gray levels in the six equilateral triangles that compose it. (b2) Orange hexagonal unit cell indicates diffraction orientation and phase determined by gray levels in the majority background pattern. (b3) Purple hexagonal unit cell indicates diffraction orientation and phase determined by gray levels in the embedded defect region. (c) Different gray levels in the six triangles linked by (c1)

green, (c2) yellow, (c3) blue, and (c4) red hexagons corresponding to the hexagons of the same color in (a).

The phase of the diffracted beams from the center of the embedded phase pattern is determined by the gray level surrounded by the hexagon in Figure 7.3(b3) using Eq. (7.6) for all beams. Around the boundary of the majority phase pattern and the embedded one, we identified four types of hexagonal structures formed by six triangles, as shown in Figure 7.3(c1–c4), that can be used to determine the phase of diffracted beams. Again, the triangles with gray level of 5 were not shown in the hexagonal structures at the bottom of Figure 7.3(c) for the purpose of neatness. In Figure 7.3(a), the upper boundary is indicated by four red hexagons and labeled by R. The phase of diffracted beams is determined by the gray levels of six triangles at the vertices of the hexagon as shown in Figure 7.3(c4). All triangles have a gray level of 153 except the top one. The bottom, left, and right boundaries are indicated by yellow (Y), green (G), and blue (B) hexagons, respectively. The phases of the diffracted beams are related to the gray level in six triangles that form hexagons, as shown at the bottom of Figure 7.3(c1, c2, c3) for green, yellow, and blue patterns around the boundary, respectively.

Figure 7.4(a) shows a CCD recorded diffraction in the Fourier plane by a 532 nm laser from the phase pattern of Figure 7.3(a) displayed on the SLM. Six first-order diffracted beams in Figure 7.4(a) are labeled from 1 to 6, which correspond to labels 1 to 6 in Figure 7.3(b2), respectively. Again, the Fourier filter lets beams 1, 3, 4, and 5 pass through, and they form interference patterns as recorded by the CCD camera in Figure 7.4(b). A white dashed square indicates the interference region of the embedded pattern, which is in good agreement with the simulated interference pattern in Figure 7.4(c1) based on the gray level of the triangle in

the hexagon in Figure 7.3(b3). Outside the white dashed square in Figure 7.4(b), the interference pattern shows dual lattices that can be simulated, as shown in Figure 7.4(c2) by four-beam interference, where the phases of the interfering beams are calculated by Eqs.(7.5) and (7.6), and the gray level of the triangles is shown in Figure 7.3(b2). Figure 7.4(d) shows the SEM of a fabricated sample with embedded patterns made by exposing the DPHPA photosensitive mixture to the interference pattern in Figure 7.4(b). The exposure time was 0.8 s. From the SEM, we can see that the embedded single- lattice structures are surrounded by dual-lattice photonic structures. Both single-lattice and dual lattice structures are in good agreement with the simulated structures in Figure 7.4(c1, c2).

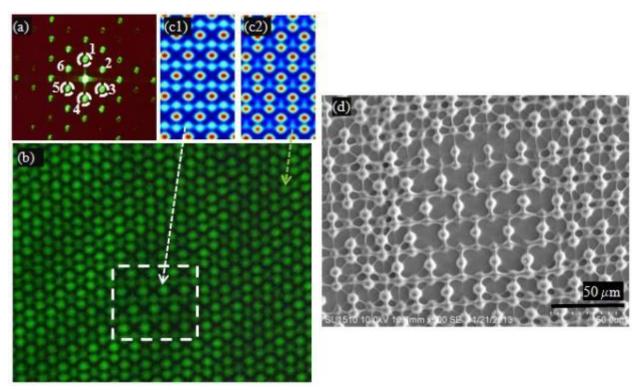


Figure 7.4. (a) Diffraction pattern from the spatially variant phase pattern in Figure 7.3(a). (b) CCD image of interference pattern in 4f region. (c) Simulated interference pattern for (c1) single and (c2) dual lattice regions. (d) SEM image of holographically fabricated structures with single lattice defect embedded in a dual lattice background.

Figure 7.5(a) shows an SEM of a fabricated sample recorded at a location that was slightly longitudinally translated along the z direction (the propagation direction of the zero-order beam). Comparing Figure 7.4(d) with Figure 7.5(a), no changes are observed in recorded structures, as the interference pattern is a two-dimensional structure. Both of them clearly show the single-lattice structures surrounded by the dual-lattice ones.

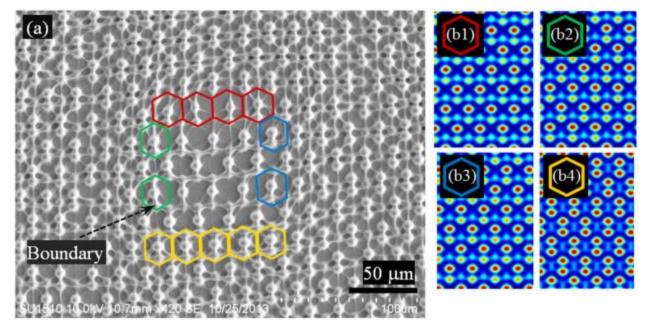


Figure 7.5. (a) SEM image of fabricated photonic structures with defect boundary marked by red, green, blue, and yellow hexagons. (b) Simulated interference patterns for the boundary regions indicated by (b1) red, (b2) green, (b3) blue, and (b4) yellow.

Figure 7.5(b1, b2, b3, b4) shows the simulated interference patterns, where the phases of interfering beams were obtained from the gray level of the triangles in Figure 7.3(c), for the upper, left, right, and bottom boundaries of embedded structures in Figure 7.5(a), respectively. From the simulations and SEM, we can see that the photonic structures along the boundary in Figure 7.4(d) and Figure 7.5(a) are in a transition from the dual-lattice to the single-lattice structures. The central region in the embedded structures has a circular dot-like structure

symmetrically supported by the chain-like structures. Along the upper, left, and right boundaries, the intensity of weak dots just below the red-dots in the interference pattern in Figure 7.5(b1, b2, and b3) is stronger than that in the central region of the embedded structures, as shown in Figure 7.4(c1). The agreement between the SEM and simulated structure is very good. Along the bottom boundary, simulations in Figure 7.5(b4) show dual-lattice structures, in good agreement with the SEM in Figure 7.4(d) and Figure 7.5(a). Our results indicate that it is possible to use a spatially variant phase mask for the fabrication of graded photonic lattices. In Figure 7.4(d) and Figure 7.5(a), the filling fraction of dielectric materials in regions of dual-lattice structures is higher than in single-lattice regions. Thus, the effective refractive index in dual-lattice regions is higher than the single-lattice regions. The local control of refractive index by the filling fraction can lead toward graded photonic crystals [131,133,137-140,149] or transformation optics devices [146-147,150], if a coordinate transformation-based phase pattern can be designed.

## **CHAPTER 8**

## GRADIENT INDEX STRUCTURES THROUGH SPATIAL LIGHT

## MODULATOR BASED HOLOGRAPHIC LITHOGRAPHY4

In Chapter 6, a phase pattern constructed from equilateral triangles with varying gray levels was introduced. When the phase pattern was displayed on the SLM, diffracted beams with defined phases were generated and interfered to fabricate photonic crystal lattices. In Chapter 7, functionally graded lattices were fabricated from triangle-pixelated phase patterns with locally defined gray levels for specific triangles. The advantage of using a geometric pixelated phase pattern is that spatial variation of the phase and subsequent variation of filling fraction in holographic structures is easy to accomplish by altering individual pixels or groups of pixels. The disadvantage of using triangles as the base pixels in the phase pattern is that each triangle consists of several SLM pixels, which limits the separation distance of the beams in the Fourier plane, thus limiting the interference angle and how small the periodicity in the photonic crystal templates can be. To take advantage of the full capability of the SLM, a phase pattern with base pixels consisting of single SLM pixels needs to be used.

<sup>&</sup>lt;sup>4</sup> Parts of this chapter have been previously published, either in part or in full, from K. Ohlinger, J. Lutkenhaus, B. Arigong, H. Zhang, Y. Lin, "Spatially addressable design of gradient index structures through spatial light modulator based holographic lithography," Journal of Applied Physics, 114, 213102 (2013), from J. Lutkenhaus, D. George, B. Arigong, H. Zhang, U. Philipose, and Y. Lin, "Holographic fabrication of photonic crystal templates using spatial-light-modulator-based phase mask method," Proc. SPIE 8974, Advanced Fabrication Technologies for Micro/Nano Optics and Photonics VII, 897419 (2014), and J. Lutkenhaus, D. George, H. Zhang, U. Philipose, and Y. Lin, "Spatial light modulator based holographic fabrication of 3D spatially varying photonic crystal templates," Proc. SPIE 9374, Advanced Fabrication Technologies for Micro/Nano Optics and Photonics VIII, 93740V (2015). Reproduced with permission from American Institute of Physics, and from SPIE Publications.

# 8.1 Pixel-by-Pixel Phase Engineering

A checkerboard phase pattern was chosen, an enlarged view of which is shown in Figure 8.1(a), consisting of 2 pixel  $\times$  2 pixel square cells tiled across the SLM's entire 1920  $\times$  1080 pixel area. The square tile cell is outlined by the orange box in Figure 8.1(a). Each square pixel within the pattern measures  $8\mu m \times 8\mu m$ , the same size as the pixels of the SLM. The gray level of each of the 4 pixels in the cell can be changed at will. The checkerboard pattern used is the simplest pattern that allows variation in gray level and also maximizes the distance between the beams in the Fourier plane by increasing the spatial frequency of the gray levels displayed on the SLM. When the laser beam is incident on the SLM while this pattern is displayed, the diffraction directions are in the horizontal and vertical directions through the centers of the pixels. Four diffracted first order beams and a central zero-order beam are generated by the SLM, as indicated by the green circles in Figure 8.1(b) and shown in the CCD image taken at the Fourier plane in Figure 8.1(c). The diffraction angle from the pixels was 1.90 degrees, resulting in a distance of 18.82 mm between the zero-order and first order beams at the Fourier plane.

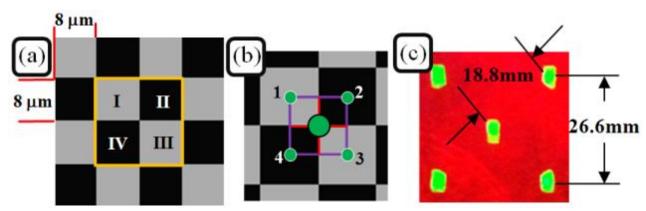


Figure 8.1. (a) An enlarged portion of the phase pattern displayed on the SLM for the generation of four 1st order beams. Each dark gray or light gray square is a single pixel measuring  $8\times8~\mu m$  in size. The orange box is drawn on the phase pattern to indicate the tile

unit of  $2 \times 2$  pixels that is repeated to create the phase pattern. (b) Close up view of the pattern from (a) with square unit cell overlaid in purple. Green circles indicate the beams diffracted from the pattern on the SLM. (c) Photograph in Fourier plane of diffraction pattern generated by the phase pattern in (a).

The purple square overlaid upon the pattern in Figure 8.1(b) represents the unit cell, with the red lines dividing the cell into blocks that determine the phase of each individual beam at the respective corners of the unit cell. The phases of the first order beams are determined from the following equations,

$$\delta_1 = \frac{2\pi}{255} \left( \frac{1}{4} \mathbf{I} \right) \tag{8.1}$$

$$\delta_2 = \frac{2\pi}{255} \left( \frac{1}{4} II \right) \tag{8.2}$$

$$\delta_3 = \frac{2\pi}{255} \left( \frac{1}{4} III \right) \tag{8.3}$$

$$\delta_4 = \frac{2\pi}{255} \left( \frac{1}{4} IV \right) \tag{8.4}$$

where, in a similar fashion to Eqs. (6.6)-(6.11), the Roman numerals indicate the gray level of the corresponding pixel in Figure 8.1(a). But with Eqs. (8.1)-(8.4), the fraction of the unit cell contributing to the average gray level (and hence, the phase) is 1/4 the area of the pixel. As in previous sections, changing the gray level of the block corresponding to the beam in that block's corner changes the phase of that particular beam.

To demonstrate that these equations are valid, and that the area ratio factor is needed, we present two test cases. In both cases, the gray level of pixels 1 and 3 is 30 (dark gray). In the first case, the gray level of pixels 2 and 4 is 94 (lighter gray), as shown in Figure 8.2(a1). If

the light were simply reflected from the checkerboard phase pattern on the SLM, the phase of beams 1 and 3 would be  $0.24\pi$ , and the phase of beams 2 and 4 would be  $0.24\pi$ +0.5 $\pi$ . With two beams being phase shifted by  $\pi/2$  relative to the other two, a woodpile structure can be formed from the interference of the four first order beams and the zero order beam. However, since the beams are diffracted from the phase pattern on the SLM, the actual phase for beams 1 and 3 is  $0.06\pi$ , and the phase for beams 2 and 4 is  $0.06\pi+0.125\pi$ . Since the phase difference between two beams relative to the other two is only  $\pi/8$ , the interference of the four side beams with the central zero order beam will result in isolated, non-connected structures. This is demonstrated in the CCD image of the interference pattern of the five beams in Figure 8.2(a2). Figure 8.2(a3) shows a simulated unit cell of structures that can be formed from this interference pattern. By moving the CCD on the translation stage in the zero-order propagation direction, we observed the 3D interference pattern to change. The maxima light spots disappeared and new maxima appeared in the center of four maxima from the previous image. Moving the CCD further resulted in the pattern from the first image re-emerging. The changes occurred in half lattice constant steps in the zero-order propagation direction, consistent with the simulated 3D unit cell of the interference pattern shown in Figure 8.2(a3).

In the second case, the gray level of pixels 2 and 4 is 255, as shown in Figure 8.2(b1). The phase of beams 1 and 3 is the same as the previous case, but the phase for beams 2 and 4 is  $0.06\pi+0.5\pi$ . With the  $\pi/2$  phase difference of beams 2 and 4 relative to beams 1 and 3, the interference of these four beams with the zero order beam can be expected to produce a woodpile structure, which can be seen in the CCD image of the interference pattern in Figure 8.2(b2), and in the simulated unit cell of structures formed from the five beam interference in

Figure 8.2(b3). The 3D woodpile structure of the interference pattern in Figure 8.2(b2) was verified by moving the CCD on the translation stage along the zero-order propagation direction and observing the pattern changing. When the CCD moved in the propagation direction, the orientation of the pattern changed by 90 degrees, then changed back, but shifted by a half lattice constant. When the CCD moved further, the pattern then changed back to the orientation of the second image, but shifted by a half lattice constant relative to the second image. Moving even further with the CCD, we observed the pattern to return to the first image. Each of the changes occurred in quarter lattice constant steps in the propagation direction.

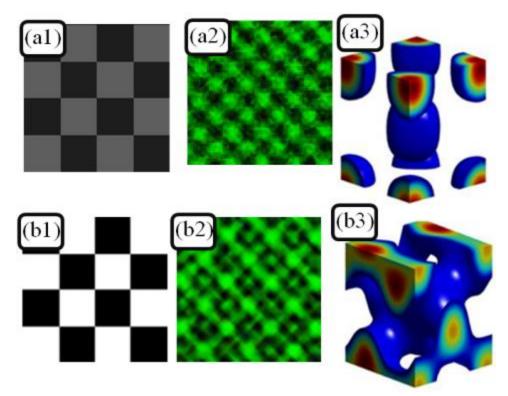


Figure 8.2. (a1) Enlarged portion of phase pattern with pixels I and III having a gray level of 30, and pixels II and IV having a gray level of 94. (a2) CCD image of interference pattern formed from beams generated by laser incident on SLM displaying pattern in (a1). (a3) Simulated isointensity surfaces of unit cell of interference pattern in (a2). (b1) Enlarged portion of phase

pattern with pixels I and III having a gray level of 30, and pixels II and IV having a gray level of 255. (b2) CCD image of interference pattern from phase pattern in (b1). (b3) Simulated iso-intensity surfaces of unit cell of interference pattern in (b2).

Using the optical setup in Figure 6.1, a DPHPA photoresist mixture was exposed to the interference pattern in Figure 8.2(b2). The photoresist was spin-coated onto a 1" glass slide at 3000 rpm for 30s. The thin-film was exposed to the interference pattern for 1 to 1.5s, immersed in propylene glycol methyl ether acetate (PGMEA) for 11 minutes, rinsed in isopropanol for 1 minute, and air dried. Figure 8.3(a) shows a scanning electron microscope (SEM) image of the resulting photonic crystal template formed in DPHPA. It very clearly has a woodpile structure, which is verified by the atomic force microscope (AFM) image in Figure 8.3(b) and the surface profiles in Figure 8.3(c1) and (c2) taken along the red and green lines, respectively, in Figure 8.3(b).

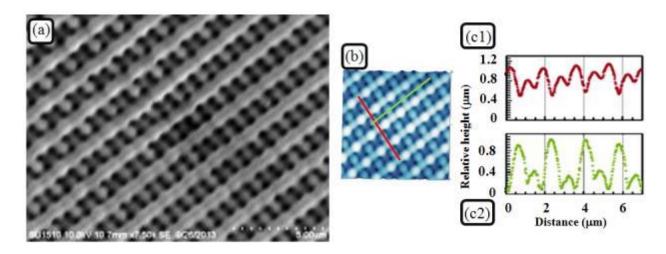


Figure 8.3. (a) SEM image of fabricated woodpile photonic crystal template in DPHPA photoresist mixture. (b) AFM image of woodpile template. (c1) Surface profile along the red line in (b). (c2) Surface profile along green line in (b).

By using the method of phase assignment to the beams diffracted from the pattern on the SLM, we can arrange pixels of different gray levels to construct a phase pattern. By rearranging Eqs. (8.1)-(8.4) into the form,

$$Gray \ Level = 255 \times \left(\frac{\delta}{\pi/2}\right) \tag{8.5}$$

we can calculate the gray levels of each pixel based on a desired phase to be assigned to a particular beam. However, as can be seen in Eq. (8.5), the maximum phase that can be assigned to any beam is  $\pi/2$ . With an SLM capable of higher phase shift and smaller pixels, such as the Holoeye LETO SLM, which has a pixel pitch of 6.4  $\mu$ m and a maximum phase shift of 6.2 $\pi$  at 405nm wavelength, even smaller periodicity and higher phase shifts assigned to the beams are possible.

With the knowledge that specific phases can be assigned to beams generated by simple geometric phase patterns displayed on the SLM, and knowing the relationship between the gray level distribution in the phase pattern and the phases assigned to the beams, these phase patterns can be used to design a phase mask for the fabrication of specified pattern defects or spatially varying, gradient index structures.

## 8.2 Effective Refractive Index of Holographically Fabricated Structures

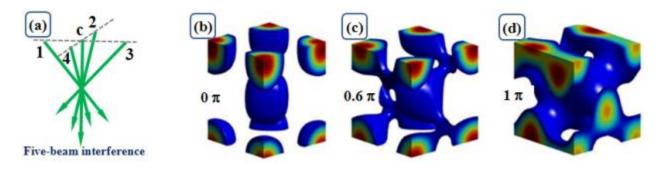


Figure 8.4. (a) Schematic of a 5 beam interference. Iso-intensity surfaces of the unit cells of the periodic five-beam interference pattern with one beam phase shifted by  $0\pi$  (b),  $0.6\pi$  (c), and  $1\pi$  (d).

Figure 8.4(a) shows the schematic beam arrangement for a five-beam interference. The four side beams are arranged symmetrically around the central one and tilted at an angle relative to the central beam, forming a five-beam interference. The five-beam interference pattern is determined by the individual beam intensity, polarization, phase, and propagation direction. The intensity profile of a five-beam interference pattern can be calculated as,

$$I(r) = I_0 + \Delta I(r) = \langle \sum_{i=1}^{5} E_i^2(r,t) \rangle + \sum_{i < j}^{5} E_i \cdot E_j \cos[(k_i - k_j) \cdot r + \Delta \delta_{ij}]$$
 (8.6)

where  $E_i$  is electric field strength,  $k_i$  is wave number,  $E_i \cdot E_j$  is related to beam polarization, and  $\Delta \delta_{ij} = \delta_i - \delta_j$  is initial phase difference. The calculated interference pattern based on Eq. (8.6) is shown in Figure 8.4(b-d). The iso-intensity surfaces are illustrated by different colors. After the photoresist receives a laser exposure and the exposed photoresist is developed, a 3D pattern corresponding to a certain iso-intensity surface ( $I_{iso}$ ) is formed. The volume fill fraction f of the polymerized region (also the effective permittivity) is determined by the step functions:

$$\varepsilon(r)_1 = 1 \text{ when } I(r) < I_{iso} \tag{8.7}$$

$$\varepsilon(\mathbf{r})_2 = n^2 \text{ when } I(r) > I_{iso} \tag{8.8}$$

where  $\epsilon$  is the dielectric constant, and n is the refractive index of the polymerized photoresist. In the regions with  $\epsilon$ 1, the photoresist is developed out and occupied by air, and in the regions with  $\epsilon$ 2, photoresist is polymerized. As shown in Figure 8.4(b-d), if one side beam is phase shifted from 0 to  $0.6\pi$  and to  $1\pi$  relative to the others, the unit cell of the five beam

interference pattern changes from isolated ellipsoids to an interconnected woodpile. Thus, the filling fraction of polymer will be phase-dependent. Based on the effective medium theory,[151-152] the effective refractive index can be calculated by the equation:

$$n_{eff}(\mathbf{r}) = \sqrt{\varepsilon(\mathbf{r})} = \sqrt{(1 - f)\varepsilon_1(\mathbf{r}) + f\varepsilon_2(\mathbf{r})},$$
 (8.9)

From this equation, it can be seen that the effective refractive index of the holographically fabricated structure, given by  $n_{\text{eff}}$ , is dependent on the filling fraction of the polymer and of the air, which is, in turn, dependent upon the phases of the interfering beams.

## 8.3 Demonstration of Simple Gradient Index Structures using the SLM

As shown in the previous chapters, geometric phase patterns displayed on the SLM are capable of assigning specific phases to the generated diffracted beams, which can change the fill fraction of the structures formed from the exposure of the thin-film photoresist to the interference pattern. The checkerboard phase pattern in Figure 8.1(a) was shown to generate four 1st order side beams with phases determined by Eqs. (8.1)-(8.4) and a 0th order central beam. This pattern changes gray levels pixel-by-pixel; however, manually setting the gray level of each of the 1920 x 1080 pixels to achieve spatial variance is impractical. The 4 pixel unit cell tile is capable of producing a large area uniform interference pattern, but cannot generate spatially varying patterns alone. Increasing the size of the unit cell tile to a larger number of pixels would allow greater variation in the pattern.

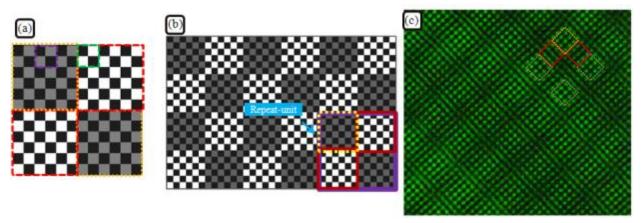


Figure 8.5. (a) Supercell phase tile assembled from unit cell tiles from Fig. 12(a1) & (b1). (b) View of portion of phase pattern made from supercell phase tile in (a); repeat unit indicated. (c) CCD image of the interference pattern in the 4f region, generated by tiling the supercell phase tile in (a) across the entire SLM, and interfering the diffracted 0th order and four 1st order beams.

For example, the large supercell phase tile in Figure 8.5(a) is composed of 4 super pixels which in turn consist of 3 x 3 of the 2 pixel x 2 pixel unit cells. The gray levels of the unit cell in the purple square in Figure 8.5(a) correspond to the phase pattern in Figure 8.2(a1) with gray levels of  $\{30,94,30,94\}$ ; gray levels in the unit cell in the green square in Figure 8.5(a) correspond to the phase pattern in Figure 8.2(b1) with gray levels of  $\{30,255,30,255\}$ . As shown in the previous chapter, the phases of beams in the purple square are  $0.06\pi$  for beams 1 and 3 and  $0.06\pi+0.125\pi$  for beams 2 and 4; for the green square, the phases of the beams are  $0.06\pi$  for beams 1 and 3 and  $0.06\pi+0.5\pi$  for beams 2 and 4. The interference of the four beams plus the central beam generated by the phase pattern in Figure 8.2(a1) produces non-bi-continuous structures, whereas the interference of the 4+1 beams produced by the phase pattern in Figure 8.2(b1) results in a connected woodpile structure. Figure 8.5(b) shows a portion of the overall phase pattern made from repeating the phase tile in Figure 8.5(a). In Figure 8.5(c), a CCD image

showing the interference pattern produced by the phase pattern made from the composite tile in Figure 8.5(a) can be seen. A small periodicity and a larger periodicity to the pattern can be seen, and squares with the same color indicate structures with the same patterns.

Extending this method to a larger composite tile allows larger areas with the same pattern to be produced. From the results in Figure 8.5, we can see that the area with the pattern from Figure 8.2(a1) produces an isolated structure, while the area with the pattern from Figure 8.2(b1) produces a woodpile structure. Using the phase pattern with the composite tile can produce an interference pattern with areas containing both structures. A larger composite tile (supercell) is shown in Figure 8.6(a) that was made for this purpose, consisting of 4 super-pixels, which are each composed of 6x6 unit cell tiles, with each unit cell tile made of 2x2 SLM pixels. The supercell is tiled across the SLM, just as the original unit cell was. A photograph of the Fourier plane is shown in Figure 8.6(b). The diffraction pattern is complex, with the 1st order beams related to the periodicity of the individual pixels shown with small red circles around them, and the 1st order beams related to the periodicity of the superpixels shown with a large red circle in the center around them. In fact, the supercell-tiled phase pattern can be considered as the addition of two checkerboard phase patterns: one with a 2 pixel periodicity (16μm), and one with a 24 pixel periodicity (192μm). This can be demonstrated in Figure 8.6(c), which shows two checkerboard phase patterns with the periodicities just mentioned, and in Figure 8.6(d), which shows photographs of their respective Fourier planes, with respective 1st order diffractions spots circled in red. In the Fourier plane photograph in Figure 8.6(b), the circled beams are allowed to pass through the Fourier filter, and all other orders are blocked.

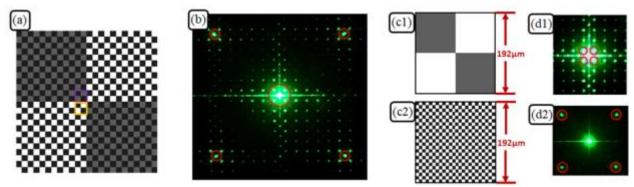


Figure 8.6. (a) Composite phase tile constructed from smaller phase tiles, which is repeated across the SLM to produce a total phase pattern. (b) Photograph of diffraction pattern in the Fourier plane generated by the phase pattern in (a); beams allowed to pass through the Fourier filter are circled in red. (c) Phase tile with (1) 24 pixel period and (2) single pixel period. (d) Fourier plane photographs of diffraction pattern from the phase pattern using the (1) (c1) tile, and (2) the (c2) tile.

The beams diffracted from the larger 192µm period pattern are only 1.87mm from the optical axis, while the outer beams diffracted from the 16µm period pattern are 18.82mm from the optical axis. The electric field in the interference region at the 4f point due to the beams allowed to pass through the Fourier filter, with phases assigned to the beams according to the gray levels of the pixels in the phase pattern, is described by the following equation:

$$E(\mathbf{r},t) = E_0 \exp[i(\mathbf{k}_0 \cdot \mathbf{r} - \omega t)] + \sum_{n=1}^4 E_n \exp[i(\mathbf{k}_n \cdot \mathbf{r} - \omega t + \delta_n)]$$

$$+ \sum_{m=1}^4 E_m \exp[i(\mathbf{k}_m \cdot \mathbf{r} - \omega t + \delta_m)]$$
(8.10)

The 1st term in Eq. (8.10) represents the zero-order beam; the second term represents the outer 1st order beams; and the final term represents the inner 1st order beams. The

interference pattern of the four outer 1st order beams plus four inner 1st order beams plus the central zero-order beam is given by:

$$I(r) = I_0 + \Delta I(r) = \langle \sum_{i=1}^{9} E_i^2(r,t) \rangle + \sum_{i< j}^{9} E_i \cdot E_j \cos[(k_i - k_j) \cdot r + (\delta_i - \delta_j)]$$
 (8.11)

Figure 8.7(a) shows simulations of two transverse planes of the interference pattern generated by the superposition of the allowed beams in Figure 8.6(b). Figure 8.7(b) shows a CCD image from the 4f point where all the allowed beams interfere together. The pattern in the CCD image resembles the simulated interference patterns in Figure 8.7(a). The interference pattern has some regions with a bright, interconnected structure, and other regions having a dimmer, more isolated structure.

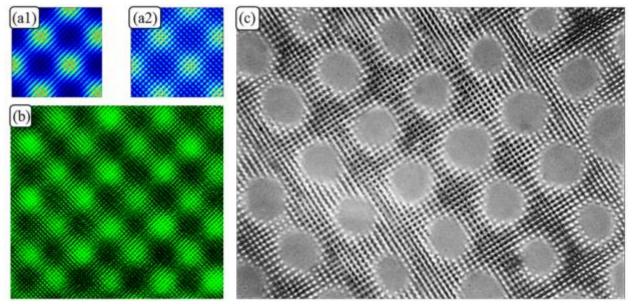


Figure 8.7. (a) Two 2D intensity profiles taken at different planes in the axial direction, showing the change in the interference pattern produced by the allowed beams in Figure 8.6(b). (b) CCD image of the interference pattern produced by the superposition of the allowed beams in Figure 8.6(b) at the 4f point. (c) Optical microscope image (40X) of holographically fabricated structures in DPHPA.

Holographic structures were fabricated by exposing a photoresist mixture to the interference pattern shown in Figure 8.7(b). The mixture was made from the following components in the specified weight concentrations: dipentaerythritol penta/hexaacrylate (DPHPA) monomer (Aldrich, 89.75%), rose bengal photoinitiator (0.014%), N-vinyl pyrrolidinone chain extender (9.6%), N-phenyl glycine co-initiator (0.58%), and triethylamine (0.055%). The DPHPA mixture was spincoated onto a glass slide at 3000rpm for 30s. The thin film was then exposed to the interference pattern for a typical time of 3.2-3.6s, developed in propylene glycol methyl ether acetate (PGMEA) for 10 minutes, and rinsed in isopropanol and allowed to air dry.

Figure 8.7(c) shows an optical microscope image of a holographically fabricated sample in DPHPA. There is a composite structure comprised of a large period square lattice with a smaller woodpile structure within. The period of the larger structure is 22.22μm, and the period of the smaller structure is 1.71μm, measured using comparison to a 3μm period AFM calibration sample. It should be noted that the exposure condition for the structure shown in Figure 8.7(c) is very strict. As seen in the CCD image in Figure 8.7(b), the darker regions of the interference pattern have a non-zero field. If the exposure time is too long, or the development time too short, the void regions in Figure 8.7(c) will be filled in with polymerized photoresist. While the fabricated lattices have a simple spatially varying structure, that structure is periodic over the entire sample. One of the advantages of using the geometric phase patterns is the ability to locally define a small region in the phase pattern to create local, non-periodic designed defects in the fabricated structures, which will be explored further in the following chapters.

## CHAPTER 9

# REGISTERING FUNCTIONAL DEFECTS INTO PERIODIC HOLOGRAPHIC STRUCTURES<sup>5</sup>

In this chapter, we present methods for registering two types of defects in periodic structures using SLM-based holographic lithography. For the fabrication of structures with different fill fractions, different diffraction efficiencies were locally designed in the phase pattern, which was displayed on the SLM. The fill fraction of local dielectrics in the holographic structures was not only controlled, these local defects were registered in the background lattice. Filling fraction control in holographic structures can lead toward the fabrication of isotropic gradient refractive index photonic crystals for electromagnetic field control. We also present the design and fabrication of a variant lattice of a 90° bend registered in a periodic background lattice.

## 9.1 Design and Fabrication of Desired Defects with Different Filling Fractions

Figure 9.1(a) shows an enlarged view of the phase pattern displayed on the SLM. The pattern consists of triangles arranged in hexagonal unit cells, one of which is indicated by the purple hexagon in Figure 9.1(a). Six 1st order beams are diffracted from the phase pattern when it is displayed on the SLM and illuminated by the laser beam, indicated by the green circles in the triangles in Figure 9.1(a) and labeled 1-6 in Figure 9.1(a) and in Figure 9.1(b). The phases of the diffracted beams are determined by the average of the gray levels; [89] for

<sup>&</sup>lt;sup>5</sup> Parts of this chapter have been previously published, either in part or in full, from J. Lutkenhaus, D. George, D. Lowell, B. Arigong, H. Zhang, U. Philipose, and Y. Lin, "Registering functional defects into periodic holographic structures," App. Opt. 54, 7007-7012 (2015), and from J. Lutkenhaus, D. George, H. Zhang, U. Philipose, and Y. Lin, "Spatial light modulator based holographic fabrication of 3D spatially varying photonic crystal templates," Proc. SPIE 9374, Advanced Fabrication Technologies for Micro/Nano Optics and Photonics VIII, 93740V (2015). Reproduced with permission from OSA Publishing, and from SPIE Publications.

example, the phase of beam 1 is determined by the average of the gray levels inside the red kite shape in Figure 9.1(a). Figure 9.1(b) shows the diffraction pattern formed from the phase pattern in the 2f plane with the 1st order beams allowed through the Fourier filter indicated by the large, green circles. Beams 1, 3, 4, & 6 were chosen because a change in the phase of beam 4 will create an easily noticeable change in the interference pattern. [89]

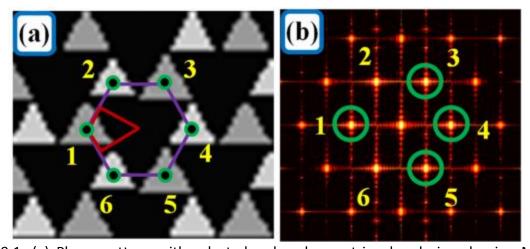


Figure 9.1. (a) Phase pattern with selected reduced area triangles designed using MATLAB program. The purple hexagon indicates the unit cell of phase pattern. Adjustable gray level and area of triangles labeled 1-6: the area of triangles 2, 4, & 6 were reduced to 75% of the size of triangles 1, 3, & 5. Beam 1 phase determined by the average gray level in the kite shaped area with red border in (a). (b) Simulated Fourier plane diffraction with 1st order diffracted beams labeled 1-6. Green circles indicate holes in the Fourier filter that allow first order diffracted beams 1, 3, 4, & 5 and block all other orders of beams.

The filling fraction of the holographically formed structures is controlled by the diffraction efficiency of the beams diffracted from the phase pattern on the SLM. The diffraction efficiency is affected by changes in the period, gray levels, and cycle in the phase pattern. The period of the pattern is fixed, so the diffraction efficiency will depend on only the

gray levels and cycle of the phase pattern. Since the gray levels of the triangles in the pattern determine the phases of the diffracted beams, this leaves changing the cycle (size of triangles/period) as the means of controlling the diffraction efficiency. To rule out the effect of the phase changing the interference pattern and study the effect on the filling fraction, we used the four beams selected in Figure 9.1(b) because of the sensitivity of the interference pattern of those four beams to small phase changes, which are easily seen. The intensity of the four interfering beams is given by:

$$I(r) = I_0 + \Delta I(r) = \langle \sum_{i=1}^4 E_i^2(r,t) \rangle + \sum_{i \le i}^4 E_i \cdot E_j e_i \cdot e_j \cos[(k_i - k_j) \cdot r + (\delta_i - \delta_j)]$$
(9.1)

where k is a wave vector,  $\delta$  the initial phase, E and e the constant of electric field strength and electrical field polarization direction, respectively. A lattice shift of m×a+n×b (a and b are lattice constants in x and y directions, respectively) in the interference pattern is observed when the phase of the beams is changed by  $\phi$ ,

$$\sum_{i < j}^{4} E_i \cdot E_j \ e_i \cdot e_j \cos[(k_i - k_j) \cdot r + (\delta_i - \delta_j) + \varphi]$$

$$= \sum_{i < j}^{4} E_i \cdot E_j \ e_i \cdot e_j \cos[(k_i - k_j) \cdot (xi + yj + ma + nb) + (\delta_i - \delta_j)]$$
(9.2)

where  $(kj-ki) \cdot (m\times a+n\times b)=\phi$ .

We performed two studies to investigate the effects of changes in diffraction efficiency on filling fraction: the first study included both phase and filling fraction effects; and the second study excluded the influence of phase on the filling fraction. Figure 9.2 shows the phase pattern generated by MATLAB using hexagonal unit cells similar to the one shown in Figure

9.1(a) with 3 distinct regions, labeled 1, 2, & 3. Region 1 is the background phase pattern with gray levels for triangles  $\{1, 2, 3, 4, 5, 6\}$  being  $\{153, 51, 153, 51, 153, 51\}$ , respectively. Region 3 is similar to the background phase pattern, but all of the triangles have gray levels of 153. In Region 2, the area of triangles  $\{2, 4, \& 6\}$  is reduced to 75% of the area of triangles  $\{1, 3, \& 5\}$ . Since the area of the triangles was reduced, the average gray level in the kite-shaped area, and subsequently, the phases of the beams were changed as well. To attempt to keep the phase of the beams in Region 2 to be the same as in Region 3, the gray level of triangles  $\{2, 4, \& 6\}$  were increased by a factor of 1/(75%)=(4/3), so that the gray levels of triangles  $\{1, 2, 3, 4, 5, 6\}$  in region 2 were  $\{153, 204, 153, 204, 153, 204\}$ , respectively.

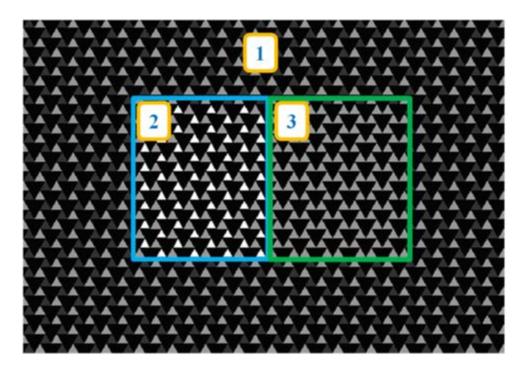


Figure 9.2. Enlarged view of phase pattern with defect area. Region 1 triangle gray levels were {153,51,153,51,153,51}. Region 3 triangle gray levels were all 153. Region 2 triangle gray levels were {204,153,204,153,204,153}. The areas of the triangles in region 2 with gray levels of 204 were 75% of those with gray levels of 153.

To measure the diffraction efficiency of each region, three phase patterns were generated using unit cells from each region. The three defect-free phase patterns, with gray levels, periods, and triangle areas kept the same as the regions described above, were each displayed on the SLM separately with a linear gamma curve (0 gray level for 0 phase to 255 gray level for  $2\pi$  phase) in use. The ratio of the measured power of beam 5 over the measured power of the zero order beam, or the diffraction efficiency, was recorded for each case. For the phase pattern made from unit cells in region 1, the diffraction efficiency was measured to be 1.28%. For region 3, it was 0.41%. For the phase pattern made from the unit cell in region 2 with the triangles with 75% of the original area, the diffraction efficiency was measured to be 3.49%. Phase patterns similar to region 2 were created with triangles reduced to n% of the original area and the gray level increased to 1/ (n%). The diffraction efficiency of the phase patterns with triangles {2, 4, & 6} reduced to 90%, 80%, & 70% of the original area was measured to be 1.08%, 2.41%, and 4.42%, respectively.

Theoretically, the phases of the diffracted beams in regions 2 and 3 should be identical. But due to the fact that the triangles in the phase pattern are represented using the square pixels of the SLM and that the base of the original triangle is only 12 pixels, the calculation of the phases may not yield exactly the same phase for the beams in region 2 and the beams in region 3. This would mean that simulation of the interference pattern using equations (1) and (2) may not yield the correct interference patterns. To simulate the interference patterns of the phase patterns with the embedded defects, fast Fourier transform (FFT) simulations were performed in MATLAB using the phase pattern in Figure 9.2 as input. The first FFT simulation gave the simulated Fourier plane (2f). A filtering operation was performed to simulate the

Fourier filter that exists in the optical setup (as seen in Figure 6.1). Then an inverse FFT gave the intensity pattern seen in Figure 9.3(a). This simulated intensity pattern in Figure 9.3(a) matches closely with the optical microscope image of the holographically formed structures in DPHPA in Figure 9.3(b).

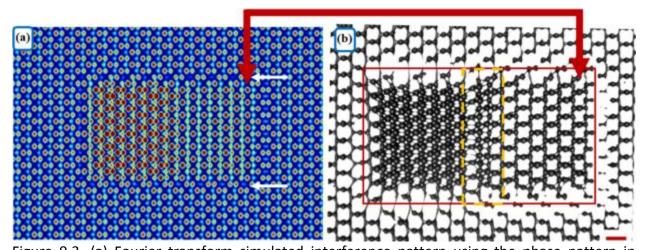


Figure 9.3. (a) Fourier transform simulated interference pattern using the phase pattern in Figure 9.2 with a linear gamma curve. The red and white arrows point to boundaries between the defect region and the background. (b) Optical microscope image of fabricated structures in DPHPA. The red rectangle indicates the location of the defect produced from the interference region corresponding to regions 2 and 3 in the phase pattern. The orange dotted line indicates the boundary lattice between regions 2 and 3. The red arrow points to the right edge of the defect boundary. Red scale bar is 100μm.

Theoretically, the phase of beam 4 in the designed defect regions 2 & 3 was shifted relative to the phase of beam 4 in the background region 1. Then, a lattice shift in the defect regions in the horizontal direction, relative to the background lattice, is expected, which is what is clearly observed in both the simulated interference pattern in Figure 9.3(a) and in the fabricated structures shown in Figure 9.3(b). The shift of the lattice in region 2 of the fabricated

structure in Figure 9.3(b) is smaller than the shift in region 3. This may be due to the fact that the triangles are displayed using the square pixels of the SLM and the phase from the average gray levels from the shrunken triangles may differ between regions 2 & 3. Another phase effect that can be seen is that of the boundary lattices formed between regions, indicated by white and red arrows in Figure 9.3(a) and (b). Because of the boundary lattices and the lattice shifting between the defect regions and the background region due to the phase differences in the interfering beams, the defect regions are not registered within the background lattice in the fabricated structures in Figure 9.3(b). Also easily observed is that the fill fraction in the fabricated structures corresponding to region 2 in the phase pattern is much higher than that corresponding to region 3. The higher diffraction efficiency of region 2 is the cause of the higher filling fraction in the corresponding region in the fabricated structures. diffraction efficiency for region 3 was lower than the measured efficiency for region 1, but in the fabricated structures, the filling fraction is higher in the area corresponding to region 3 in the phase pattern than in the area corresponding to region 1. The higher filling fraction in region 3 is explained by phase-shifting-induced intensity redistribution.

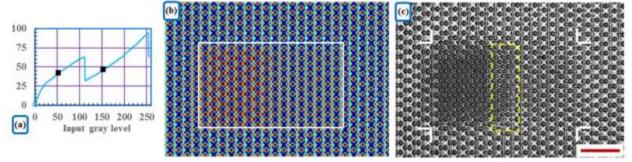


Figure 9.4. (a) Non-linear gamma curve provided by HoloEye. The two black squares represent the gray levels of 51 and 53. (b) Simulated interference pattern using the non-linear gamma curve. White rectangle indicates the location of the defect region corresponding to regions 2

and 3 in the phase pattern from Figure 9.2. (c) Optical microscope image of structures holographically fabricated in DPHPA using the phase pattern from Figure 9.2 and the gamma curve in (a). White lines indicate the corners of the defect region, and the yellow dotted line indicates the boundary region between regions 2 and 3.

To reduce the phase effects in the interference pattern and study the effects of the diffraction efficiency change from the reduction in area of the triangles in region 2 of the phase pattern, a gamma curve provided by HoloEye was used with the phase pattern displayed on the SLM. This curve is shown in Figure 9.4(a). Gray levels 51 and 153 are labeled with black squares on the curve. Due to the non-linear shape of the curve, the two gray levels are almost the same. In fact, with this curve in use, the phases of all of the first order beams are nearly equal. Recalling that the gray level scheme of region 1 was {153, 51, 153, 51, 153, 51}, the scheme of region 3 was all 153, the gray level scheme of region 2 was {153, 75% of 204, 153, 75% of 204, 153, 75% of 204}, and 51 and 153 are almost the same using this curve, we see that the phases do not vary much across the diffracted beams. Thus, we predict no lattice shifting in the interference pattern. Figure 9.4(b) shows the simulated interference pattern in the 4f plane using the HoloEye gamma curve and the designed phase pattern shown in Figure 9.2. As predicted, no lattice shifting is seen in the simulated interference pattern in Figure 9.4(b). The white box in Figure 9.4(b) demarcates the boundary of the defect region containing regions 2 and 3. Figure 9.4(c) shows the holographically fabricated structures in DPHPA. There is no lattice shifting between the different regions, as predicted and seen in Figure 9.4(b), and the defect regions are very well registered into the background lattice.

The measured diffraction efficiencies for regions 1, 2, & 3 using the non-linear gamma curve were 2.81%, 13.01%, and 4.68%, respectively. These values are higher than those with the linear curve, with region 2's diffraction efficiency being over three times higher. These higher diffraction efficiencies caused the higher filling fractions observed in the fabricated structures in Figure 9.4(c), with the filling fraction in region 2 being visibly much higher than in regions 1 or 3. These results show that the diffraction efficiency of phase patterns displayed on the SLM can be locally altered for the purpose of locally controlling the filling fraction in the holographically fabricated structures, and that the designed defects are registered into the background. This translates to local control over the index of refraction, which sets the stage for a single exposure fabrication of gradient index structures such as photonic crystal GRIN lenses [36-38] or cloaking applications. [39-41]

## 9.2 Registering Desired Defects with 90° Bend with Periodic Structures

In order to reduce the size of optical components for the integration of optical circuits, it is important to have optically functional structures with the capability to flow a light beam through a 90 degree bend. [6, 131,134,137-140] Spatially variant lattices have been synthesized for 90 degree bending of light beams by simultaneously varying the lattice orientation, spacing, and fill fraction. [131,134,137-140] These functional structures have been fabricated, but have not been integrated with background periodic structures. [131,134,137-140] We used two methods to register such functional defects into background periodic structures. This was achieved by first establishing a uniform lattice, then defining the spatial variance parameters, followed by the construction of a spatially variant wave vector field. From the spatially variant

wave vector field, a grating phase function was calculated through a gradient function, a relationship realized by:

$$\mathbf{k}_i = \nabla \varphi_i \tag{9.3}$$

where  $k_i$  is the wave vector field for the ith beam, and  $\varphi_i$  is the phase of the ith beam. This was accomplished by approximating the gradient function by central finite difference method, then solving the set of equations for the phase using the least squares method. In Ref. 43, the calculated phase function was used with a SLM to generate a 2D spatially variant wave field. We further expanded on this method by introducing spatially variant defect structures within a uniform lattice.

To generate the spatially varying phase pattern, we first chose the number of beams, the initial phases of those beams, and the interference angle, which controls the periodicity, in order to set up the initial uniform lattice. For the phase pattern in Figure 9.5(a), 4 beams were specified, with the initial phases of those beams being set to zero. Then, the spatial variance parameters are chosen. A MATLAB program is used to approximate the derivatives via finite difference calculations, and numerically solve the set of equations for the phase functions of the different beams. The phase functions are then used as the phases for the electric fields of the beams, and the electric fields are summed. The phase of the total electric field is extracted and used as a phase pattern on the SLM.

For the phase pattern for the pure desired defect region in Figure 9.5(b), the lattice spacing parameter was held constant, and the lattice orientation parameter was chosen as

$$\Theta(x,y) = \left(\frac{\pi}{2}\right) \frac{\sqrt{(x^2 + y^2)}}{\sqrt{(x_{max}^2 + y_{max}^2)}},$$
(9.4)

where  $x_{max}$  and  $y_{max}$  represent the size of the defect region. The orientation parameter only exists in the defect region defined by  $x_{max}$  and  $y_{max}$ . Outside of the defect region, the orientation parameter is zero.

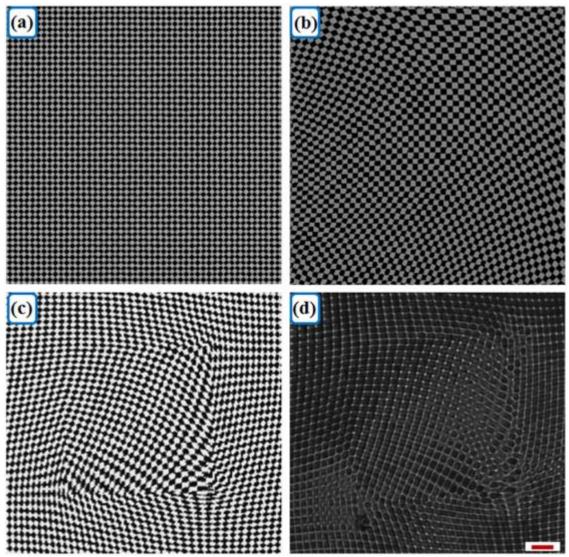


Figure 9.5. (a) Background phase pattern of a periodic square lattice where a desired defect will be registered. (b) Enlarged view of the phase pattern of desired defects with a 90° bend (c) Enlarged view of phase pattern with phase of defect region and background calculated

simultaneously. (d) Optical microscope image of fabricated thin-film sample using the phase pattern in (c). Scale bar measures 20  $\mu$ m.

Initially, we calculated the phase function of the entire pattern all at once. This phase pattern can be seen in Figure 9.5(c). The top left of the desired defect lattice was well registered into the background lattice. However, this resulted in distortion near the other edges of the defect region, as seen in Figure 9.5(c), and distortions throughout the phase pattern. This carried over into the exposure of the thin-film samples, as seen in Figure 9.5(d), where the lattice distortions are clearly observed. To address the distortion issue, the calculation of the phase pattern was broken up into two steps. The first step was to calculate the uniform lattice with constant lattice spacing, seen in Figure 9.5(a), and no lattice orientation parameter specified. Then a second calculation was performed to find the phase of the defect region, seen in Figure 9.5(b). Then the phase of the defect region was inserted into the uniform lattice phase. The complete phase pattern, shown in Figure 9.6(a), was then displayed on the SLM.

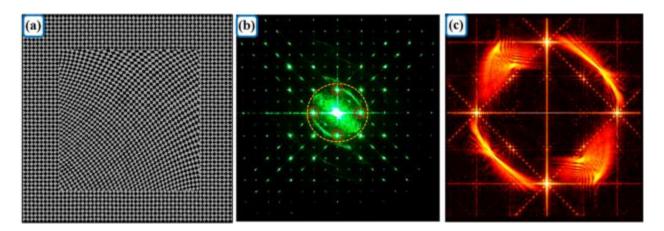


Figure 9.6. (a) Enlarged view of the phase pattern with a 90° bend defect embedded in a uniform background phase with defect region and background phase calculated separately. (b)

Photograph of diffraction pattern in Fourier plane produced by phase pattern in (a). (c) Simulation of Fourier plane from Fourier transform of the phase pattern in (a).

Figure 9.6(b) shows the diffraction pattern in the 2f plane generated by the laser beam diffracting from the phase pattern in Figure 9.6(a) on the SLM. The four 1st order diffraction spots are circled in red. The ring of light connecting the 1st order spots is due to the spatially varying defect. The Fourier filter blocked all higher order spots outside of the area indicated by the yellow circle in Figure 9.6(b). The light inside the area of the yellow circle was allowed to pass through the Fourier filter, which included the 1st order beams, the ring of light, and the central 0th order beam. A Fourier transform (FT) simulation in MATLAB of the 2f plane can be seen in Figure 9.6(c). The first order region in the simulated image closely resembles the photograph of the diffraction pattern, with the first order spots and the ring of light apparent.

The diffracted beams allowed through the Fourier filter are interfered at the 4f point after the second lens in the optical setup (seen in Figure 6.1). A subsequent FT of the simulated 2f plane in Figure 9.6(c) produces a simulation of the 4f plane, as seen in Figure 9.7(a), which shows an interconnected structure and the 90° bend in the lattice orientation. If the desired defect region is used to turn light by 90°, the light input and output directions are marked by the arrows in Figure 9.7(a). In these two directions, the lattices in the desired defect region were registered with the background lattice. Figure 9.7(b) shows a FT simulation of the 4f plane if the zero order region is blocked by the Fourier filter. By blocking the zero-order region, small voids appear around the edges of the defect, and the overall intensity in the 4f plane decreases. If a thin-film photoresist is exposed to the interference pattern in Figure 9.7(b), the small voids have the potential to cause the defect region to detach from the rest of the polymerized

photoresist during the development process, resulting in a void instead of a spatially varying defect. In comparison to the intensity pattern in Figure 9.7(b), the simulated intensity in Figure 9.7(a) does not have these voids around the edges of the defect. For this reason, the zero-order beam was allowed to pass through the Fourier filter and interfere with the other beams.

Photonic crystal templates were holographically fabricated in photoresist by exposure to the interference of the allowed beams shown in Figure 9.6(b). The photoresist was made from the following components in specified weight concentrations: DPHPA monomer (Aldrich, 90.25%); rose bengal photoinitiator (0.045%); NPG co-initiator (0.67%); NVP chain extender (8.92%); and triethylamine (0.12%). The mixture was spincoated onto a glass slide at a speed of 7500 rpm for 30s. The thin film on the glass slide was then exposed to the interference pattern at the 4f plane for a typical time of 0.05-0.1s. Then, the exposed samples were immersed in PGMEA developer for 10 minutes, followed by an isopropanol rinse. In the optical microscope photograph in Figure 9.7(c), the holographically fabricated structure in DPHPA with a 90° bend defect in a background pattern can be seen. The fabricated lattices along the left and bottom edges of the desired defect region were registered with the background better than those along the top and right edges. That is the desired result because the left and bottom edges of the defect region will be used for coupling light beams, as shown in Figure 9.7(a).

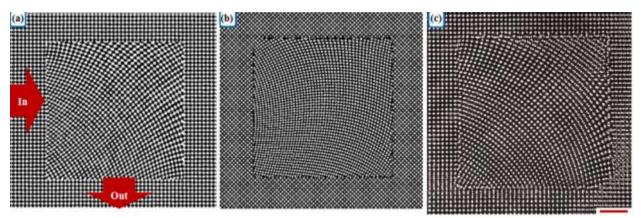


Figure 9.7. (a) Simulation of 4f interference pattern using Fourier transform of light allowed to pass through the Fourier filter as indicated in Figure 9.6(b). (b) Simulation of 4f interference pattern if the zero-order diffraction spot is blocked. (c) Optical microscope image (25X) showing a fabricated spatially variant 2D photonic crystal template with a 90° bend defect in a uniform background lattice. Scale bar measures 50 μm.

The period in the fabricated holographic structures was in the micrometer range. The period of the background pattern in Figure 9.7(c) is 7.8 $\mu$ m, measured using comparison to a 3 $\mu$ m AFM standard sample. These structures can be used to control mid-infrared light. [18 from registered defect paper] To produce structures that can control light in the visible range, the period of the fabricated structures will need to be reduced. Further reduction of the period can be achieved by demagnification of the 4f imaging system ( $f_1/f_2$ ), using an objective lens with a high magnification and using an SLM with a smaller pixel size.

## **CHAPTER 10**

# HOLOGRAPHIC FABRICATION OF DESIGNED FUNCTIONAL DEFECT LINES IN PHOTONIC CRYSTAL LATTICES USING A SPATIAL LIGHT MODULATOR<sup>6</sup>

In this chapter, we realize direct imaging of functional defect lines in PhCs through holographic lithography by assigning one gray level for each pixel in the SLM. Because the functional defects are integrated in the phase pattern, the interfering beams not only carry the defect's content, but also the defect related phase information. The phase shift of interfering beams near the functional defects modifies the photonic lattice near the defects. The phase-related lattice shift was studied in five beam and in three beam interference patterns, and this knowledge was used to design and fabricate functional defects registered into the photonic lattices.

## 10.1 Theory

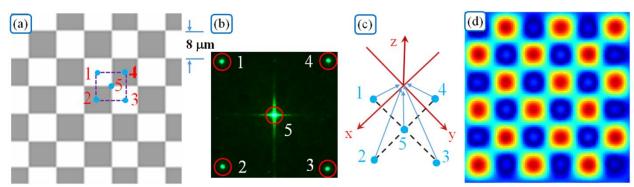


Figure 10.1. (a) An enlarged view of the checkerboard phase pattern displayed on the SLM. The dashed purple square indicates the size of one unit cell of 8 x 8  $\mu$ m<sup>2</sup>. (b) CCD image of the diffraction pattern at the Fourier plane. The red circles indicate beams passing through the

<sup>&</sup>lt;sup>6</sup> Parts of this chapter have been previously published, either in part or in full, from J. Lutkenhaus, D. George, D. Lowell, H. Zhang, Y. Lin, "Holographic fabrication of designed functional defect lines in photonic crystal lattice using a spatial light modulator," Micromachines 7, 59 (2016). Reproduced with permission from Multidisciplinary Digital Publishing Institute.

Fourier filter. (c) Scheme of the five beam interference arranged four-fold symmetrically. Beam 5 propagates along the z-axis. (d) Simulated intensity distribution for the interference of the four first order beams with the central zero order beam.

Figure 10.1(a) shows an enlarged view of a square checkerboard phase pattern comprised of 2 pixel  $\times$  2 pixel square cells tiled across the SLM's entire 1920  $\times$  1080 pixel area. The purple square indicates one of the unit cells with the direction of periodicity at 45 degrees with respect to horizontal and vertical directions. The size of the unit cell is  $8 \times 8 \ \mu m^2$ , which is also the size of one pixel in the SLM. The gray level of each pixel in the unit cell can be individually set to desired values. When the checkerboard pattern is displayed on the SLM and then illuminated by the expanded and collimated 532nm laser beam, four first order beams, labeled (1, 2, 3, 4) in Figure 10.1(a), and a central zero order beam (labeled 5 in Figure 10.1(a)) are diffracted from the SLM. The phases of the diffracted beams (1, 2, 3, 4) are determined by the formula

$$\phi = (2\pi/255) * (Gray Level/4). \tag{10.1}$$

The factor of 4 in the formula is due to the fact that a quarter of each pixel is included in the dashed purple unit cell in Figure 10.1(a). Figure 10.1(b) shows an example of the diffraction pattern of the laser beams diffracted by the checkerboard phase pattern on the SLM at the Fourier plane of the 4f imaging system (shown in Figure 6.1). The pattern was recorded by a CCD camera. Surrounding the 0th order diffraction in the center, four 1st order diffractions (labeled 1, 2, 3, and 4) form a pattern that has 4-fold symmetry. A Fourier filter is used to let the beams inside the red circles pass through. Propagating through the second lens, these five

beams are overlapped in the 4f plane. The wave vectors of the diffracted beams at the 4f interference plane are arranged four-fold symmetrically with beam 5 propagating on the optical axis, as arranged in the coordinate system shown in Figure 10.1(c). The five beams are represented by the following equations:

$$E_1(r,t) = E_1 \cos[(k \sin\theta) y + (k \cos\theta)z - \omega t + \delta_1]$$
(10.2)

$$E_2(r,t) = \mathbf{E}_2 \cos[-(k\sin\theta)x + (k\cos\theta)z - \omega t + \delta_2]$$
(10.3)

$$E_3(r,t) = \mathbf{E}_3 \cos[-(k\sin\theta)y + (k\cos\theta)z - \omega t + \delta_3]$$
(10.4)

$$E_4(r,t) = \mathbf{E}_4 \cos[(k\sin\theta) x + (k\cos\theta)z - \omega t + \delta_4]$$
(10.5)

$$E_5(r,t) = \mathbf{E}_5 \cos[kz - \omega t + \delta_5] \tag{10.6}$$

where  $E_i$  is the electric field, k is the wave vector, and  $\delta_i$  is the initial phase of the beam. An interference pattern is formed when the five beams are overlapped. The intensity distribution in the interference pattern can be determined by the following equation and the interference pattern in x-y plane is shown in Figure 10.1(d):

$$I(r) = I_0 + \Delta I(r) = \langle \sum_{i=1}^{5} E_i^2(r,t) \rangle + \sum_{i < j}^{5} \mathbf{E}_i \cdot \mathbf{E}_j \cos[(k_j - k_i) \cdot r + (\delta_j - \delta_i)]$$
 (10.7)

If we integrate the functional defects into the phase pattern, the first order diffracted beams carry the spatial frequency information of the defect line. The amplitude patterns associated with each first-order diffracted beam are shifted with the same spatial frequency from the origin by an amount of  $\sin \theta/\lambda$ . When the diffracted beams are overlapped for the interference, the interfering beams not only carry the defect's content, but also the defect

related phase information. The phase shift of interfering beams near the functional defects will modify the photonic lattice near the defects.

### 10.2 Functional Defect Lines in Square Photonic Lattices through 5-Beam Interference

In this section, the lattice shift during the direct imaging of functional defect lines in the PhC lattice is studied through five-beam interference lithography. The checkerboard pattern is used as a background phase pattern with a bright gray level of 255 and a dark gray level of 30, as shown in Figure 10.2(a). For the functional defect line, the gray levels of a line of pixels are changed to 255 to create a white line defect in the background phase as shown in Figure 10.2(a). In Figure 10.2(b), an enlarged view of the line defect in the phase pattern is shown. The red dashed square indicates a unit cell from which the phase of the interfering beams can be calculated. Before adding the defect line to the phase pattern, the pixel for beam 4 in the defect phase shown in Figure 10.2(b) had a gray level of 30. After adding the defect, the gray level of the pixel for beam 4 is changed to 255. Thus, the phase of beam 4 in the defect line in Figure 10.2(b) is shifted by  $\beta*2\pi$ , where  $\beta=((255-30)/255)*0.25$ . The lattice shift in the defect region of the five-beam interference pattern due to beam 4 can be written as:

$$\Delta I_4 = \mathbf{E}_1 \cdot \mathbf{E}_4 \cos[(-k\sin\theta)x + (k\sin\theta)y + (\phi_1 - \phi_4) - \beta \cdot 2\pi]$$

$$+ \mathbf{E}_2 \cdot \mathbf{E}_4 \cos[(-2k\sin\theta)x + (\phi_2 - \delta_4) - \beta \cdot 2\pi]$$

$$+ \mathbf{E}_3 \cdot \mathbf{E}_4 \cos[(-k\sin\theta)x - (k\sin\theta)y + (\phi_3 - \phi_4) - \beta \cdot 2\pi]$$

$$+ \mathbf{E}_4 \cdot \mathbf{E}_5 \cos[(k\sin\theta)x + (k\cos\theta - k)z + (\phi_4 - \phi_5) + \beta \cdot 2\pi].$$
(10.8)

The lattice constant in the x-y plane is defined to be  $a=\lambda/\sin\theta$ , and the lattice constant in the z-direction is defined to be  $c=\lambda/((1-\cos\theta))$ , where  $\lambda$  is the wavelength of the interfering beams. Based on these lattice constants, Eq. (10.8) can be rewritten as:

$$\Delta I_4 = \mathbf{E}_1 \cdot \mathbf{E}_4 \cos[-(2\pi/a)x + (2\pi/a)y + (\delta_1 - \delta_4) - \beta \cdot 2\pi]$$

$$+ \mathbf{E}_2 \cdot \mathbf{E}_4 \cos[-(4\pi/a)x + (\delta_2 - \delta_4) - \beta \cdot 2\pi]$$

$$+ \mathbf{E}_3 \cdot \mathbf{E}_4 \cos[-(2\pi/a)x - (2\pi/a)y + (\delta_3 - \delta_4) - \beta \cdot 2\pi]$$

$$+ \mathbf{E}_4 \cdot \mathbf{E}_5 \cos[(2\pi/a)x + (2\pi/c)z + (\delta_4 - \delta_5) + \beta \cdot 2\pi]$$
(10.9)

The shift in the defect lattice relative to the background lattice due to the phase shift of  $\beta*2\pi$  in beam 4 can be determined by the following equation (which is modified from Eq.(10.9)):

$$\Delta I_{4} = \mathbf{E}_{1} \cdot \mathbf{E}_{4} \cos[2\pi((-1/a)i + (1/a)j + 0k)(x + y + z + \beta(0.5a + 0.5a \pm 0.5c)) + (\delta_{1} - \delta_{4})]$$

$$+ \mathbf{E}_{2} \cdot \mathbf{E}_{4} \cos[2\pi((-2/a)i + 0j + 0k)(x + y + z + \beta(0.5a \pm 0.5a \pm 0.5c)) + (\delta_{2} - \delta_{4})]$$

$$+ \mathbf{E}_{3} \cdot \mathbf{E}_{4} \cos[2\pi((-1/a)i + (-1/a)j + 0k)(x + y + z + \beta(0.5a - 0.5a \pm 0.5c)) + (\delta_{3} - \delta_{4})]$$

$$+ \mathbf{E}_{4} \cdot \mathbf{E}_{5} \cos[2\pi((1/a)i + 0j + (-1/c)k)(x + y + z + \beta(0.5a \pm 0.5a - 0.5c)) + (\delta_{4} - \delta_{5})]$$
(10.10)

The x and y axes are labeled in Figure 10.2(b). A phase shift of  $\beta*2\pi$  can result in a pattern shift of  $\beta$  (0.5a±0.5a±0.5c) in the defect region, indicated by the red arrows in Figure 10.2(b). By applying different x- and y-axes, the same analysis can be applied to the unit cells immediately above, opposite to, or to the right of the dashed red square in Figure 10.2(b). The

blue arrows indicate the lattice shift directions for three unit cells. The theoretical analysis predicts that the photonic pattern near the defect line is stretched and squeezed periodically in the horizontal direction and shifted away vertically from the center of the defect line, leaving a gap on either side of the line defect. Figure 10.2(c) shows an optical microscope image of the fabricated PhC structures with designed defect line in DPHPA photoresist. Although a 3D pattern is predicted in Eq. (10.7), a 2D PhC lattice is formed in Figure 10.2(c) when we use very thin film of DPHPA. In the region near the defect line, the lattice pattern is squeezed periodically in the horizontal direction and shifted away from the line center as predicted by the theory.

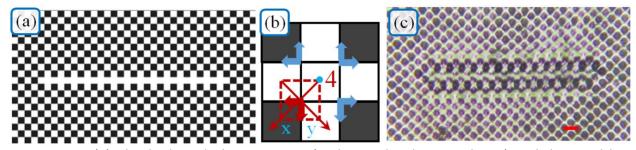


Figure 10.2. (a) Checkerboard phase pattern (with gray levels 30 and 255) and designed line defect (gray level 255). Each bright or dark square in the pattern represents a single square SLM pixel. (b) Close-up of portion of line defect in phase pattern. Arrows indicate the direction of the lattice shift due to the phase shift. Red square represents the unit cell for calculating phases of the interfering beams. (c) Optical microscope image of fabricated structures in DPHPA. Scale bar measures 8 microns.

If the gray level for the pixels in the defect line is assigned to be 30 (black) instead of 255 (white), the phase shift of beam 4 as shown in Figure 10.3(a) is  $\beta$ =((30-255)/255)\*0.25 relative to the background pattern. This causes an interference pattern shift in a direction of (-1, 1) or (-1, -1) for 2D pattern in the defect region as shown by red arrows in Figure 10.3(b), the

opposite direction as shown by red arrows in Figure 10.2(b). As indicated by the red and blue arrows in Figure 10.3(b), the lattice in the defect region is expected to squeeze together and stretch away periodically in the horizontal direction and shift toward the center of the defect line vertically. This is what has been seen in the interference pattern recorded in the DPHPA photoresist in Figure 10.3(c). These studies approve that the diffracted beams not only carry the defect-content but also shifted-phase information.

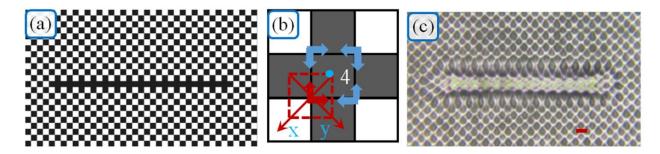


Figure 10.3. (a) Checkerboard phase pattern with black (gray level 30) defect line. (b) Enlarged view of line defect in phase pattern. Arrows indicate the direction of the lattice shift due to the presence of the line defect phase. The red square represents the unit cell for calculating phases of the beams. (c) Optical microscope image of line defect embedded in PhC lattice in DPHPA fabricated through holographic lithography. Scale bar measures 8 microns.

## 10.3 Functional Line Defects in Square Photonic Lattices through Three-Beam Interference

As shown in Figure 10.2(b) and Figure 10.3(b), each unit cell carries the phase shift information of the diffracted beams, and these phase effects cause unintended squeezing of the lattice near the defect line. In an attempt to mitigate the effects of the phase content in the diffracted beams, two of the beams (1 and 2 in red) were blocked at the Fourier filter as shown in Figure 10.4(a). The two remaining diffracted beams (3 and 4) plus the central zero order beam (5) form an interference pattern, as shown in Figure 10.4(b). The interference pattern still

maintains a square lattice. Figure 10.4(c) and Figure 10.4(d) are enlarged views the of phase patterns in Figure 10.2(a) and Figure 10.3 (a), respectively. The unit cell in the top dashed red square in Figure 10.4(c) and Figure 10.4(d) has a shifted-phase contribution in diffracted beam 2, while the unit cell at the bottom dashed square contributes to the phase of beam 1. Because the diffraction beams 1 and 2 are blocked, only diffracted beams from the blue solid squares in Figure 10.4(c) and Figure 10.4(d) carry the phase shift signal and form the interference pattern with shift directions as indicated by the blue arrows.

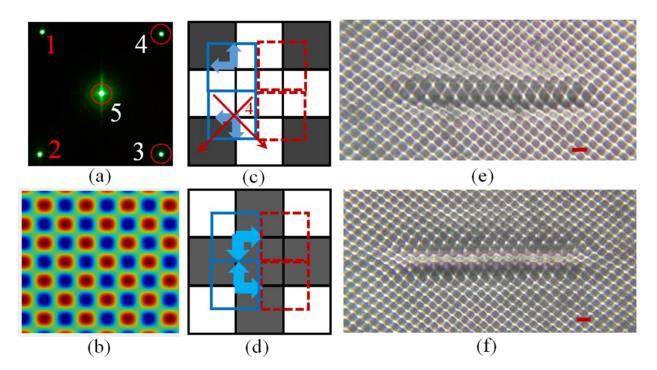


Figure 10.4. (a) CCD image of the diffraction pattern at the Fourier plane. The red circles indicate beams passing through the Fourier filter. (b) Interference pattern of two 1st order side beams with the central zero order beam. Scheme of white (gray level 255) (c) and dark (gray level 33) (d) defect phase. Blue arrows indicate direction of the lattice shift due to the presence of the defect. (e-f) Optical microscope images of fabricated defects in PhC lattice using the defect phases in background phase pattern in (c-d), respectively. Scale bar measures 8 microns.

In theory, it can be understood by the formula for three-beam interference and assuming a phase shift of  $\beta*2\pi$  for beam 4:

$$\begin{split} \mathbf{I}(\mathbf{r}) &= \mathbf{I}_{0} + \Delta \mathbf{I}(\mathbf{r}) = \mathbf{I}_{0} \\ &+ \mathbf{E}_{3} \cdot \mathbf{E}_{4} \cos \left[ 2\pi \left( (-1/a)i + (-1/a)j + 0k \right) \left( x + y + z \right) \right. \\ &+ \beta \left( 0.5a + 0.5a \pm 0.5c \right) \right) + \left( \delta_{3} - \delta_{4} \right) \right] \\ &+ \mathbf{E}_{3} \cdot \mathbf{E}_{5} \cos \left[ 2\pi \left( 0i + (-1/a)j + (-1/c)k \right) \left( x + y + z \right) + \left( \delta_{3} - \delta_{5} \right) \right] \\ &+ \mathbf{E}_{4} \cdot \mathbf{E}_{5} \cos \left[ 2\pi \left( (1/a)i + 0j + (-1/c)k \right) \left( x + y + z + \beta \left( 0.5a \pm 0.5a - 0.5c \right) \right) \right. \\ &+ \left. \left( \delta_{4} - \delta_{5} \right) \right] \end{split}$$

We fabricated PhC patterns with the designed defects by exposing the photoresist DPHPA to the interference pattern given by two first order diffracted beams (3 and 4) and the central beam 5. Figure 10.4(e) and Figure 10.4(f) show optical microscope images of fabricated PhC patterns with designed defects in DPHPA using the designed defect lines in Figure 10.4(c) and Figure 10.4(d) in the background phase pattern, respectively. The fabricated samples in Figure 10.4(e) and Figure 10.4(f) show no squeezing or stretching in the horizontal direction, in contrast to the fabricated samples in Figure 10.2(c) and Figure 10.3(c). In the vertical direction, the photonic lattice in Figure 10.4(e) is shifted away from the defect line center, similar to the phenomenon in Figure 10.2(c), while the photonic lattice in Figure 10.4(f) is shifted toward the defect line center, similar to the phenomenon in Figure 10.3(c). The theory predicts an alternating shifting in defect lattices in vertical direction because beams 1 and 2 are blocked by the Fourier filter. The width of the central squeezed region in vertical direction in Figure 10.4(f) is narrower than the one in Figure 10.3(c) due to the alternating shifting. From these results,

there is an improvement in the direct imaging of functional defects, by using 2+1 interference rather than 4+1 interference.

# 10.4 45° Orientation of Functional Line Defect in Square Photonic Crystal Lattice

When the square pixels are periodically arranged along the horizontal and vertical directions as in the checkerboard pattern in Figure 10.1(a), the interference pattern is a square lattice that is aligned at 45 degrees relative to the horizontal direction as shown in Figure 10.1(d). However the fabricated defect line in the PhC is still in the original orientation as in the designed phase pattern. In order to register the defect lines along the lattice vector directions (oriented 45 degrees relative to horizontal or vertical direction) in the PhC lattice, the orientation of the line defect in the phase pattern is rotated 45° from the horizontal (or vertical) axis as shown in Figure 10.5(a).

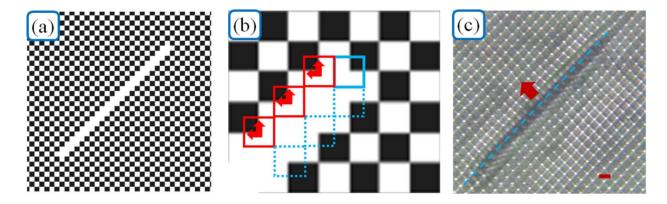


Figure 10.5. (a) Enlarged view of a diagonal line defect phase in the checkerboard phase pattern. (b) Diagram of defect phase with accompanying lattice shifts indicated by the red arrows. (c) Optical microscope image of fabricated structures in DPHPA produced by overlapping two of the 1st order beams with the central zero order region diffracted from the phase pattern in (a) displayed on the SLM. The red arrow indicates the pattern shifting

direction. The dashed blue line indicates the location of lattices if there is no pattern shifting. Scale bar measures 8 microns.

The ordinarily black pixels along a diagonal line in the checkerboard phase pattern are changed into white pixels, creating the line defect phase. Figure 10.5(b) shows an enlarged view of a portion of the line defect in the background phase pattern. The red and blue squares indicate the unit cells from which the phase shift is calculated. In the unit cell of solid red squares, the diffracted beam 3 carries the information of the shifted phase relative to the background phase pattern. Diffracted beams 1 and 2 carry the shifted phase information for the unit cells in dashed blue squares and in solid blue squares, respectively. The first order diffracted beams (1 and 2) are blocked by the Fourier filter at the 2f plane, so only the unit cells indicated by the red squares in Figure 10.5(b) contribute to the shifting of the lattice due to the presence of the defects. The red arrows indicate the direction of the lattice shift in the interference pattern. Figure 10.5(c) shows an optical microscope image of the fabricated PhC lattices with line defects in DPHPA. In the image, only photonic lattices on one side of line defects are shifted away from the defect as indicated by the red arrows in Figure 10.5(c) and the lattices on the opposite side are not distorted, in very good agreement with the prediction in Figure 10.5(b). By orienting the defect at 45 degrees and using 2+1 interference, several improvements have been realized including (a) alignment of the defect with the lattice side direction (instead of diagonal direction) of the background lattice square and (b) the shifting is only in one side of the defects.

#### 10.5 Registering the Functional Line Defect in Square Photonic Crystal Lattices

After fully understanding the lattice shift due to the "defect-content" and "shiftedphase" in the diffracted beams, we improved the design from Figure 10.5(a). The new design includes a defect with a smaller relative phase shift and utilizes the difference in diffraction efficiency between the defect region and the background. Three beam (3, 4 and 5 as shown in Figure 10.6(a)) interference was used. Gray levels of 158 and 254 were used for the dark pixels and white pixels in the background phase pattern, respectively. These two numbers are selected due to the high diffraction efficiency of 12.3% of the first order diffracted beams relative to the total power reflected by the SLM. The dark pixels along the defect line in Figure 10.6(b)-top were changed to a light gray with a gray level of 224. A square phase pattern with gray levels of 224 and 254 has a low diffraction efficiency of just 1.6% for the first order diffracted beams. The dashed squares near the defect line indicate the unit cells that do not carry the shifted phase information in the diffracted beams 3 and 4, relative to beams diffracted from the background phase pattern. The solid red squares are the unit cells that carry the shifted-phase information and will shift the lattice vertically up and the blue solid square is for the unit cell that shifts the lattice to the left.

However the phase shift of  $2\pi^*$   $\beta$ =((228-158)/255)\*0.25\*2 $\pi$  is three times smaller than the phase shift of ((255-30)/255)\*0.25\*2 $\pi$  in Figure 10.5(b). Figure 10.6(b)-bottom shows the fabricated defect line in the background PhC lattice. Due to the small phase shift, the PhC lattices near the defect line are almost registered with the background lattice. In the middle of defect line, we can see void lattices due to the low diffraction efficiency. For the lattice at the ends of the defect line indicated by the blue and yellow arrows, the unit cells have half (158,

254) and half (224, 254) pixels. These two lattices survive after the holographic lithography. The lattice indicated by the blue arrow is smaller (or weaker) than the lattice indicated by the yellow arrow due to the pattern shifting in the former lattice. Overall, walls at the boundaries of the line defect are smaller than the other due to the diffraction efficiency. This effect can be removed if the phase pattern at the boundaries is designed to shift the pattern from the background toward the boundaries to compensate the low diffraction efficiency. Under an exposure with a longer exposure time, the lattice in the middle of the defect line can also survive. Figure 10.6(c)-top shows a CCD image of the interference pattern with a defect line. Figure 10.6(c)-bottom shows a fabricated defects-integrated PhC lattice in DPHPA with smaller (or weaker) but surviving defect lattices. These results clearly demonstrate that a desired and functional defect lattice can be registered into the background lattice through direct imaging. A similar method can be used to make more complex defect structures in 2D such as ring resonators and resonant add-drop filters or couplers [22,153] or even to 3D if an objective lens and a thick photoresist film are used.

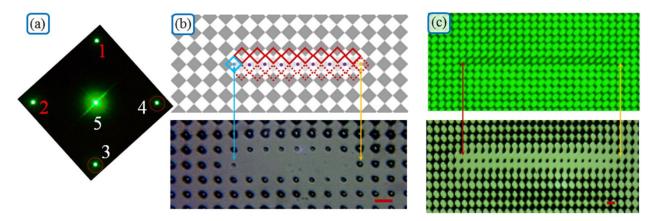


Figure 10.6. (a) CCD image of the diffraction pattern in the Fourier plane f1. All images are rotated 45 degrees to orient the defect along the horizontal direction. Beams 1 and 2 were

filtered out with a mask. (b) The phase pattern displayed on the SLM and an optical microscope image of the fabricated structure. The background of the SLM image consists of single pixels of grey levels 254 and 158 and in the defect, the grey pixels have been changed to 224. (c) CCD image of the interference pattern and optical microscope image of the recorded interference generated by the phase pattern in (b), however with a longer defect. Scale bar is 5.65 microns as measured by atomic force microscope.

The direct imaging of designed defects in PhC lattices has been achieved by utilizing the high resolution capability of the SLM. We understand the defect related pattern shifting near the designed defect through the theoretical prediction and experimental validation. By reducing the relative phase shift and incorporating different diffraction efficiencies for the defect line and background phase pattern, we have simultaneously fabricated designed defects in a PhC lattice where the defect lattices are registered with the PhC lattice.

#### CHAPTER 11

#### CONCLUSION

To summarize, the research detailed in this dissertation focused primarily on the use of a spatial light modulator to simultaneously generate multiple beams and locally manipulate the phases of those beams for the purpose of interfering them for the holographic fabrication of 2D and 3D photonic crystal templates in photoresist polymer. Through manipulation and control of the phases of the beams, a multitude of structures are possible, including engineered defect structures in the photonic crystal templates.

Before we explored the use of the SLM, we used a lab-made, silicon-based, reflective optical element to generate and steer multiple beams, and also change their polarizations, manipulate their phase shifts and intensity ratios. The generated beams were then used to holographically fabricate 3D woodpile-type photonic crystal templates in DPHPA using a single optical element and single exposure process. The PDMS mold technique used for the ROE in Chapter 5 was later abandoned in favor of 3D printed ROEs, which allow more flexibility in design and fabricated structures.

Then, we turned our focus to study tunable holographic lithography using an electrically addressable spatial light modulator. For the first time, we were able to understand and assign the phase for the diffracted beams from the phase pattern displayed on the SLM. The phases of the interfering beams were found to be tunable by the gray levels in the phase pattern and verified by the holographically fabricated structures. By assigning gray levels for cellular pixels in the phase pattern at specific locations using the SLM, we were able to design spatially variant phase patterns for the fabrication of graded photonic lattices, including a missing lattice or

single lattice embedded in dual lattice structures. By interfering beams generated by a binary checkerboard phase pattern displayed on the SLM, woodpile structures were fabricated. The checkerboard pattern was explored further by arranging the gray levels into supercells in the phase pattern, allowing us the ability to produce simple, spatially-varying holographic structures. We then explored a method of registering defect lattices within background periodic lattices through local modification of the diffraction efficiency of the phase pattern. Through local modification of the diffraction efficiency, we were able to modify the local fill fraction of polymerized materials, and simultaneously achieve lattice matching between modified and background regions. We then turned to a second method of registering spatially variant lattices with a 90° bend within the background periodic lattice through two steps of phase engineering of the laser beam. Finally, we achieved direct imaging of designed defects in PhC lattices by utilizing the high resolution capability of the SLM. We understand the defect related pattern shifting near the designed defect through the theoretical prediction and experimental validation. By reducing the relative phase shift and incorporating different diffraction efficiencies for the defect line and background phase pattern, we simultaneously fabricated the designed defects in PhC lattice where the defect lattices are registered with the PhC lattice. Through SLM-based holographic lithography, the setup is made simpler, and local manipulation of the phases of the beams allows the fabrication and registration of defect structures in photonic crystal templates. The results reported in this dissertation mark a step toward a fast, single step approach for holographic fabrication of photonic circuits embedded in PhCs.

#### **BIBLIOGRAPHY**

- [1] R. W. Keyes, "Fundamental limits of silicon technology," Proceedings of the IEEE 89, 227-239 (2001).
- [2] H. John Caulfield & Shlomi Dolev, "Why supercomputing requires optics," Nature Photonics 4, 261 263 (2010).
- [3] R. G. Beausoleil, P. J. Kuekes, G. S. Snider, S. Y. Wang and R. S. Williams, "Nanoelectronic and Nanophotonic Interconnect," Proceedings of the IEEE 96, 230-247 (2008).
- [4] E. Yablonovitch, "Inhibited spontaneous emission in solid state physics and electronics", Phys. Rev. Lett., 58, 2059, (1987).
- [5] S. John, "Strong localization of photons in certain disordered dielectric super lattices," Phys. Rev. Lett. 58, 2486–2489 (1987).
- [6] J.D. Joannopoulos, S.G. Johnson, R.D. Meade, and J.N. Winn, Photonic Crystals; Princeton University Press:Princeton, NJ, USA (2008).
- [7] E. Kuramochi, K. Nozaki, A. Shinya, K. Takeda, T. Sato, S. Matsuo, H. Taniyama, H. Sumikura, and M. Notomi, "Large-scale integration of wavelength-addressable all-optical memories on a photonic crystal chip," Nature Photonics 8, 474-481 (2014).
- [8] C. Sun, M.T. Wade, Y. Lee, J.S. Orcutt, L. Alloatti, M.S. Georgas, A.S. Waterman, J.M. Shainline, R.R. Avizienis, S. Lin, B.R. Moss, R. Kumar, F. Pavanello, A.H. Atabaki, H.M. Cook, A.J. Ou, J.C. Leu, Y.H. Chen, K. Asanovic, R.J. Ram, M.A. Popovic and V.M. Stojanovic, "Single-chip microprocessor that communicates directly using light," Nature 528, 534-538 (2015).

- [9] S. Y. Lin, E. Chow, V. Hietala, P.R. Villenueve, and J.D. Joannnopoulous, "Experimental demonstration of guiding and bending electromagnetic waves in a photonic crystal," Science 274-276 (1998).
- [10] M. Loncar, D. Nedelijkovic, T. Doll, J. Vuckovic, A. Scherer, and T.P. Pearscall, "Waveguiding in planar photonic crystal," Appl. Phys. Lett. 77, 1937-1939 (2000).
- [11] W. Bogaerts, R. Baets, P. Dumon, V. Wiaux, S. Beckx, D. Taillaert, B. Luyssaert, J. Van Campenhout, P. Bientsman, and D. Van Thourhout, "Nanophotonic waveguides in siliconon-insulator fabricated with CMOS technology," J. Lightwave Tech. 23, 401-412 (2005).
- [12] J.H. Chen, Y.T. Huang, Y.L. Yang, and M.F. Lu, "Design, fabrication, and characterization of Si-based ARROW-B photonic crystal sharp-bend waveguides and power splitters," J. Lightwave Tech. 30, 2345-2351 (2012).
- [13] L. Wu, M. Mazilu, J.F. Gallet, and T.F Krauss, "Dual lattice photonic crystal beam splitters," Appl. Phys. Lett. 86, 211106 (2005).
- [14] S. Kawashima, M. Okano, M. Imada, and S. Noda, "Design of compound-defect waveguides in three-dimensional photonic crystals," Opt. Express 6303-6307 (2006).
- [15] J. Romero-Vivas, D.N. Chigrin, A.V. Lavrimenko, and C.M. Sotomayor Torres, "Resonant add-drop filter based on a photonic quasicrystal," Opt. Express 13, 826-835 (2005).
- [16] Z. Qiang, W. Zhou, and R.A. Soref, "Optical add-drop filters based on photonic crystal ring resonators," Opt. Express 15, 1823-1831 (2007).
- [17] S. Fan, P.R. Villenueve, J.D. Joannopoulos, and H.A. Haus, "Channel-drop filters in photonic crystals," Opt. Express 3, 4-11 (1998).

- [18] M. Notomi, A. Shinya, S. Mitsugi, E. Kuramochi, and H.Y. Ryu, "Waveguides, resonators, and their coupled elements in photonic crystal slabs," Opt. Express 12, 1551-1561 (2004).
- [19] J.J. Vegas Olmos, M. Tokushima, and K. Kitayama, "Photonic add-drop filter based on integrated photonic crystal structures," IEEE J. of Selected Topics in Quantum Electronics 16, 332-337 (2010).
- [20] O. Painter, R.K. Lee, A. Scherer, A. Yariv, J.D. O'Brien, P.D. Papkus, and I. Kim, "Two-dimensional band-gap defect mode laser," Science 284, 1819-1821 (1999).
- [21] Y. Akahane, T. Asano, B.S. Song, and S. Noda, "High-Q photonic nanocavity in a two-dimensional photonic crystal," Nature 425, 944-947 (2003).
- [22] M. Qi, E. Lidorikis, P.T. Rakich, S.G. Johnson, J.D. Joannopoulos, E.P. Ippen, and H.I. Smith, "A three-dimensional optical photonic crystal with designed point defects," Nature 429, 538-542 (2004).
- [23] Z. Zhang, T. Yoshie, X. Zhu, J. Xu, and A. Scherer, "Visible two dimensional photonic crystal slab laser," Appl. Phys. Lett. 89, 071102 (2006).
- [24] V.G. Veselago, "The electrodynamics of substances with simultaneously negative values of  $\epsilon$  and  $\mu$ ," Sov. Phys. Uspekhi 10, 509-514 (1968).
- [25] M. Notomi, "Theory of light propagation in strongly modulated photonic crystals: Refractionlike behavior in the vicinity of the photonic band gap," Phys. Rev. B 62, 696-705 (2000).
- [26] C. Luo, S.G. Johnson, J.D. Joannopoulos, and J.B. Pendry, "All-angle negative refraction without negative effective index," Phys. Rev. B. 65, 201104 (2002).

- [27] S. Foteinopoulou and C.M. Soukoulis, "Negative refraction and left-handed behavior in two-dimensional photonic crystals," Phys. Rev. B 67 235107 (2003).
- [28] E. Cubukcu, K. Aydin, E. Ozbay, S. Foteinopoulou, C.M. Soukoulis, "Negative refraction by photonic crystals," Nature 423, 604-605 (2003).
- [29] E. Cubukcu, K. Aydin, E. Ozbay, S. Foteinopoulou, C.M. Soukoulis, "Subwavelength resolution in a two-dimensional photonic crystal based superlens," Phys. Rev. Lett. 91, 207401 (2003).
- [30] P.V. Parimi, W.T. Lu, P. Vodo, and S. Sridhar, "Imaging by flat lens using negative refraction," Nature, 426, 404 (2003).
- [31] Moussa, R., Foteinopoulou, S., Zhang, L., Tuttle, G., Guven, K., Ozbay, E. and Soukoulis, C.M., "Negative refraction and superlens behavior in a two-dimensional photonic crystal," Phys. Rev. B 71, 085106 (2005).
- [32] Ohlinger, K., Olvera, I. and Lin, Y., "Negative refraction behaviors in two-dimensional elliptical-rod photonic crystals in a centered rectangular lattice," J. Appl. Phys. 106, 023516 (2009).
- [33] Lutkenhaus, J., Ohlinger, K., Zhang, H., Lin, Y., "Negative refraction in the third photonic band of a two-dimensional elliptical rod photonic crystal in a centered rectangular lattice," Proc. SPIE 8269, Photonic and Phononic Properties of Engineered Nanostructures II, 8269F (2012).
- [34] H. Kurt and D.S. Citrin, "Graded index photonic crystals," Opt. Express 15, 1240-1253 (2007).

- [35] H. Kurt and D.S. Citrin, "A novel optical coupler design with graded-index photonic crystals," IEEE Photonics Tech. Lett. 19, 1532-1534 (2007).
- [36] Q. Wu, J.M., Gibbons, and W. Park, "Graded negative index lens by photonic crystals,"

  Opt. Express 16, 16941-16949 (2008).
- [37] C. Tan, T. Niemi, C. Peng, and M. Pessa, "Focusing effect of a graded index photonic crystal lens," Opt. Comm. 284, 3140-143 (2011).
- [38] B. Vasic and R. Gajic, "Self-focusing media using graded photonic crystals: focusing, Fourier transforming and imaging, directive emission, and directional cloaking," J. of Appl. Phys. 110, 053103 (2011).
- [39] J.Li and J.B. Pendry, "Hiding under the carpet: A new strategy for cloaking," Phys. Rev. Lett. 101, 203901 (2008).
- [40] T. Ergin, N. Stenger, P. Brenner, J.B. Pendry, and M. Wegener, "Three-dimensional invisibility cloak at optical wavelengths," Science 328, 337-339 (2010).
- [41] G. Zheng, H. Zhang, and Y. Lin, "Design of low-cost photonic crystal based three-dimensional invisibility cloak," Proc. of SPIE 8031, 803130 (2011).
- [42] A.J. Wolf, H. Hauser, V. Kubler, C. Walk, O. Hohn, B. Blasi, "Origination of nano- and microstructures on large areas by interference lithography," Microelectronic Eng. 98, 293-296 (2012).
- [43] C. Kittel, Introduction to Solid State Physics, John Wiley & Sons, Inc.: Hoboken, NJ, USA (2005).
- [44] D. Levine and P.J. Steinhardt, "Quasicrystals: A new class of ordered structures," Phys. Rev. Lett. 53, 2477 (1984).

- [45] Z.V. Vardeny, A. Nahata, and A. Agrawal, "Optics of photonic quasicrystals," Nature Photonics 7, 177-187 (2013).
- [46] C. Jin, B. Qin, M. Yang, and R. Qin, "Photonic band gap in two-dimensional triangular non-Bravais lattice, "Proc. of SPIE 2891, 284-288 (1996).
- [47] X. Zhang, M. Theuring, Q. Song, W. Mao, M. Begliarbekov, and S. Strauf, "Holgraphic control of motive shape in plasmonic nanogap arrays," Nano Lett. 11, 2715-2719 (2011).
- [48] W. Setyawan and S. Curtarolo, "High-throughput electronic band structure calculations: Challenges and tools," Computational Mat. Sci. 49, 299-312 (2010).
- [49] S.G. Johnson and J.D. Joannopoulos, "Block-iterative frequency domain methods for Maxwell's equations in a planewave basis," Opt. Express 8, 173-190 (2001).
- [50] M. Plihal and A.A. Maradudin, "Photonic band structure of two-dimensional systems: the triangular lattice," Phys. Rev. B 44, 8565-8571 (1991).
- [51] R. Wang, X.H. Wang, B.Y. Gu, and G.Z. Yang, "Effects of shapes and orientations of scatterers and lattice symmetries on the photonic band gap in two-dimensional photonic crystals," J. of Appl. Phys. 90, 4307-4313 (2001).
- [52] C.M. Anderson, and K.P. Giapis, "Larger two-dimensional photonic band gaps," Phys. Rev. Lett. 77, 2949-2952 (1996).
- [53] F. Wen, S. David, X. Checoury, M. El Kurdi, and P. Boucaud, "Two dimensional photonic crystals with large complete photonic band gaps in both TE and TM polarizations," Opt. Express 16, 12278-12289 (2008).
- [54] K.M. Ho, C.T. Chan, and C.M. Soukoulis, "Existence of a photonic gap in periodic dielectric structures," Phys. Rev. Lett. 65, 3152-3155 (1990).

- [55] E. Yablonovitch, T.J. Gmitter, and K.M. Leung, "Photonic band structure: The face-centered-cubic case employing nonspherical atoms," Phys. Rev. Lett. 67, 2295-2298 (1991).
- [56] S.Y. Lin, J.G. Fleming, D.L. Hetherington, B.K. Smith, R. Biswas, K.M. Ho, M.M. Sigalas, W. Zubrzycki, S.R. Kurtz, and J. Bur, "A three-dimensional photonic crystal operating at infrared wavelengths," Nature 394, 251-253 (1998).
- [57] S.Y. Lin and J.G. Fleming, "A three-dimensional optical photonic crystal," J. Lightwave Tech. 17, 1944-1947 (1999).
- [58] Y. Lin and P.R. Herman, "Effect of structural variation on the photonic band gap in woodpile photonic crystal with body-centered-cubic symmetry," J. Appl. Phys. 98, 063104 (2005).
- [59] J. Lutkenhaus, D. George, B. Arigong, H. Zhang, U. Philipose, and Y. Lin, "Holographic fabrication of functionally graded photonic lattices through spatially specified phase patterns," Appl. Opt. 53, 2548-2555 (2014).
- [60] M. Notomi, E. Kuramochi, and H. Taniyama, "Ultrahigh –Q nanocavity with 1D photonic gap," Opt. Express 16, 11095-11102 (2008).
- [61] A. Chelnolkov, S. Rowson, J.M. Lourtioz, L. Duvillaret, and J.L. Coutaz, "Light controllable defect modes in three-dimensional photonic crystal," Elec. Lett. 34, 1965-1967 (1998).
- [62] H. Altug, D. Englund, and J. Vuckovic, "Ultrafast photonic crystal nanocavity laser,"

  Nature Physics 2, 484-488 (2006).
- [63] Y.A. Vlasov, X.Z. Bo, J.C. Sturm, and D.J. Norris, "On-chip natural assembly of silicon photonic bandgap crystals," Nature 414, 289-293 (2001).

- [64] S.H. Kim, S.Y. Lee, S.M. Yang, and G.R. Yi, "Self-assembled colloidal structures for photonics," NPG Asia Mat. 3, 25-33 (2011).
- [65] R. Rengarajan, D. Mittleman, C. Rich, and V. Colvin, "Effect of disorder on the optical properties of colloidal crystals," Phys. Rev. E 71, 016615 (2005).
- [66] C.C. Cheng and A. Scherer, "Fabrication of photonic band gap crystals," J. Vac. Sci. Technol. B 13, 2696 (1995).
- [67] S. Takayama, H. Kitagawa, Y. Tanaka, T. Asano, and S. Noda, "Experimental demonstration of complete photonic band gap in two-dimensional photonic crystal slabs," Appl. Phys. Lett. 87, 061107 (2005).
- [68] H.K. Fu, Y.F. Chen, R.L. Chern, and C.C. Chang, "Connected hexagonal photonic crystals with largest full band gap," Opt. Express 13, 7854-7860 (2005).
- [69] M. Stepanova and S. Dew, Nanofabrication, Springer-Verlag Wien: New York, USA (2012).
- [70] H.B. Sun, S. Matsuo, H. Misawa, "Three-dimensional photonic crystal structures achieved with two-photon-absorption photopolymerization of resin," Appl. Phys. Lett. 74, 786 (1999).
- [71] M. Deubel, G. Von Freymann, M. Wegener, S. Pereira, K. Busch, and C.M. Soukoulis, "Direct laser writing of three-dimensional photonic crystal templates for telecommunications," Nature Materials 3, 444-447 (2004).
- [72] M. Thiel, J. Fischer, G. von Freymann, and M. Wegener, "Direct laser writing of three-dimensional submicron structures using a continuous wave laser at 532 nm," Appl. Phys. Lett. 97, 221102 (2010).

- [73] E. Hecht, Optics, Addison Wesley: New York, USA (2002).
- [74] L.Z. Cai, X.L. Yang, and Y.R. Wang, "All fourteen Bravais lattices can be formed by interference of four noncoplanar beams," Opt. Lett. 27, 900-902 (2002).
- [75] L.Z. Cai, X.L. Yang, Q. Liu, and Y.R. Wang, "What kind of Bravais lattice can be made by interference of four umbrellalike beams?," Opt. Comm. 224, 243-246 (2003).
- [76] Y. Zono and T. Ochi, "All fourteen Bravais lattices can be fabricated by triple exposure of two-beam interference fringes," Proc. of SPIE 6327, 632709 (2006).
- [77] R. Proietti Zaccaria, S. Shoji, H.B. Sun, and S. Kawata, "Multi-shot interference approach for any kind of Bravais lattice," Appl. Phys. B 93, 251-256 (2008).
- [78] Y.K. Pang, J.C.W. Lee, C.T. Ho, and W.Y. Tam, "Realization of woodpile structure using optical interference holography," Opt. Express 14, 9113-9120 (2006).
- [79] Y.Yang and G.P. Wang, "Realization of periodic and quasiperiodic microstructures with sub-diffraction-limit features sizes by far-field holographic lithography," Appl. Phys. Lett. 89, 111104 (2006).
- [80] J. Xu, R. Ma, X. Wang, and W.Y. Tam, "Icosahedral quasicrystals for visible wavelengths by optical interference holography," Opt. Express 15, 4287-4295 (2007).
- [81] Y. Yang, Q. Li, and G.P. Wang, "Fabrication of periodic complex photonic crystals constructed with a portion of photonic quasicrystals by holographic lithography," Appl. Phys. Lett. 93, 061112 (2008).
- [82] A. Harb, F. Torres, K. Ohlinger, Y. Lin, K. Lozano, D. Xu, and K.P. Chen, "Holographically-formed three-dimensional Penrose-type photonic quasicrystal through a lab-made single diffractive optical element," Opt. Express 18, 20512-20517 (2010).

- [83] H.M. Su, Y.C. Zhong, X. Wang, X.G. Zheng, J.F. Xu, and H.Z. Wang, "Effects of polarization on laser holography for microstructure fabrication," Phys. Rev. E. 67, 056619 (2003).
- [84] J.H. Klein-Wiele and P. Simon, "Fabrication of periodic nanostructures by phase-controlled multiple-beam interference," Appl. Phys. Lett. 83, 4707-4709 (2003).
- [85] J.H. Moon, S.M. Yang, D.J. Pine, and W.S. Chang, "Multiple-exposure holographic lithography with phase shift," Appl. Phys. Lett. 85, 4184-4186 (2004).
- [86] J.W. Menezes, L. Cescato, E.J. de Carvalho, and E.S. Braga, "Recording different geometries of 2D hexagonal photonic crystals by choosing the phase between two-beam interference exposures," Opt. Express 14, 8578-8583 (2006).
- [87] X.S. Xie, M. Li, J. Guo, B. Liang, Z.X. Wang, A. Sinitskii, Y. Xiang, and J.Y. Zhou, "Phase manipulated multi-beam holographic lithography for tunable optical lattices," Opt. Express 15, 7032-7037 (2007).
- [88] Y. Lin, A. Harb, D. Rodriguez, K. Lozano, D. Xu, and K.P. Chen, "Holographic fabrication of photonic crystals using multidimensional phase masks," J. of Appl. Phys. 104, 113111 (2008).
- [89] J. Lutkenhaus, D. George, M. Moazzezi, U. Philipose, and Y. Lin, "Digitally tunable holographic lithography using a spatial light modulator as a programmable phase mask,"

  Opt. Express 21, 26227-26235 (2013).
- [90] Microchem. "SU-8 2025-2075 Data Sheet," [Online] Available:
  <a href="http://www.microchem.com/pdf/SU-82000DataSheet2025thru2075Ver4.pdf">http://www.microchem.com/pdf/SU-82000DataSheet2025thru2075Ver4.pdf</a> [Accessed: June 14, 2016].

- [91] Spectra Group Limited, Inc. "H-Nu 470 Visible/UV-Visible Photoinitiator." [Online]

  Available: <a href="http://www.sglinc.com/Portals/0/Images/limited/PDFS/photoinitiators/H-Nu%20470%20TDS.pdf">http://www.sglinc.com/Portals/0/Images/limited/PDFS/photoinitiators/H-Nu%20470%20TDS.pdf</a> [Accessed: June 14, 2016].
- [92] Sigma-Aldrich. "Dipentaerythritol penta-/hexa-acrylate" [Online] Available: <a href="http://www.sigmaaldrich.com/catalog/product/aldrich/407283?lang=en&region=US">http://www.sigmaaldrich.com/catalog/product/aldrich/407283?lang=en&region=US</a>
  [Accessed June 14, 2016].
- [93] Y.Lin, A. Harb, D. Rodriguez, K. Lozano, D. Xu, and K.P. Chen, "Fabrication of two-layer integrated phase mask for single-beam and single-exposure fabrication of three-dimensional photonic crystal," Opt. Express 16, 9165-9172 (2008).
- [94] Y. Lin, A. Harb, K. Lozano, D. Xu, and K.P. Chen, "Five beam holographic lithography for simultaneous fabrication of three-dimensional photonic crystal templates and line defects using phase tunable diffractive optical element," Opt. Express 17, 16625-16631 (2009).
- [95] N. Tetreault, G. von Freymann, M. Deubel, M. Hermatschweiler, F. Perez-Willard, S. John, M. Wegener, and G.A. Ozin, "New route to three-dimensional photonic bandgap materials: Silicon double inversion of polymer templates," Adv. Mat. 18, 457-460 (2006).
- [96] X. Wang, J.F. Xu, H.M. Su, Z.H. Zeng, Y.L. Chen, H.Z. Wang, Y.K. Pang, and W.Y. Tam, "Three-dimensional photonic crystals fabricated by visible light holographic lithography," Appl. Phys. Lett. 82, 2212-2214 (2003).
- [97] N.D. Lai, W.P. Liang, J.H. Lin, C.C. Hsu, and C.H. Lin, "Fabrication of two- and three-dimensional periodic structures by multi-exposure of two-beam interference technique,"

  Opt. Express 13, 9605-9611 (2005).

- [98] L. Wu, Y. Zhong, C.T. Chan, K.S. Wong, G.P. Wang, "Fabrication of large area two-and three-dimensional polymer photonic crystals using single refracting prism holographic lithography," Appl. Phys. Lett. 86, 241102 (2005).
- [99] L. Wu, Y. C. Zhong, K. S. Wong, G. P. Wang, and L. Yuan, "Fabrication of hetero-binary and honeycomb photonic crystals by one-step holographic lithography," Appl. Phys. Lett. 88, 09115 (2006).
- [100] M. Lei, B. Yao, and R.A. Rupp, "Structuring by multi-beam interference using symmetric pyramids," Opt. Express 14, 5803-5811 (2006).
- [101] Y. Yang, Q. Li, and G.P. Wang, "Design and fabrication of diverse metamaterial structures by holographic lithography," Opt. Express 16, 11275-11280 (2008).
- [102] D. Xu, K.P. Chen, A. Harb, D. Rodriguez, K. Lozano, and Y. Lin, "Phase tunable holographic fabrication for three-dimensional photonic crystal templates by using a single optical element," App. Phys. Lett. 94, 231116 (2009).
- [103] X.H. Sun, X.M. Tao, and Y.Y. Wang, "Various photonic crystal structures fabricated by using a top-cut hexagonal prism," Appl. Phys. A 98, 255-261 (2010).
- [104] S.X. Hong, L. Wei, W.G. Liang, and T.X. Ming, "Optics design of a top-cut prism interferometer for holographic photonic quasicrystals," Opt. Comm. 285, 4593-4598 (2012).
- [105] J. Lutkenhaus, F. Farro, D. George, K. Ohlinger, H. Zhang, Z. Poole, K. Chen, and Y. Lin, "Holographic fabrication of 3D photonic crystals using silicon based reflective optical element," Opt. Mater. Express 2, 1236-1241 (2012).

- [106] J. Lutkenhaus, D. George, D. Garrett, H. Zhang, Y. Lin, "Holographic formation of compound photonic crystal and nano-antenna templates through laser interference," Journal of Applied Physics, 113, 103103 (2013).
- [107] D. George, J. Lutkenhaus, D. Lowell, M. Moazzezi, M. Adewole, U. Philipose, H. Zhang, Z. Poole, K. Chen, and Y. Lin, "Holographic fabrication of 3D photonic crystals through interference of multi-beams with 4 + 1, 5 + 1 and 6 + 1 configurations," Opt. Express 22, 22421-22431 (2014).
- [108] K. Ohlinger, H. Zhang, Y. Lin, D. Xu, and K.P. Chen, "A tunable three layer phase mask for single laser exposure 3D photonic crystal generations: bandgap simulation and holographic fabrication," Opt. Mater. Express 1, 1034-1039 (2011).
- [109] J. C. Tracy, L. F. Thompson, R. D. Heidenreich, and J. L. Merz, "Gratings for Integrated Optics by Electron Lithography," Appl. Opt. 13, 1695-1702 (1974)
- [110] V. Berger, O. Gauthier-Lafaye, and E. Costard, "Fabrication of a 2D photonic bandgap by a holographic method," Elec. Lett. 33, 425-426 (1997).
- [111] I. Divliansky, T.S. Mayer, K.S. Holliday, and V.H. Crespi, "Fabrication of three-dimensional polymer photonic crystal structures using single diffraction element interference lithography," Appl. Phys. Lett. 82, 1667-1669 (2003).
- [112] Texas Instruments, Inc. "Laser power handling for DMDs" [Online] Available: <a href="http://www.ti.com/lit/wp/dlpa027/dlpa027.pdf">http://www.ti.com/lit/wp/dlpa027/dlpa027.pdf</a> [Accessed: June 14, 2016]
- [113] T. Haist and W. Osten, "Holography using pixelated spatial light modulators part 1: theory and basic considerations," J. Micro/Nanolith. MEMS MOEMS 14, 041310 (2015).

- [114] B.E.A. Saleh and M.C. Teich, Fundamentals of Photonics, John Wiley & Sons, Inc.: Hoboken, NJ, USA (2007).
- [115] Z. Zhang, Z. You, and D. Chu, "Fundamentals of phase-only liquid crystal on silicon (LCOS) devices," Light: Science & Applications 3, e213 (2014).
- [116] Holoeye.com. "HoloEye Photonics AG >> Spatial Light Modulators," [Online] Available: <a href="http://holoeye.com/spatial-light-modulators/">http://holoeye.com/spatial-light-modulators/</a> [Accessed: June 14, 2016].
- [117] A. Marquez, F.J. Martinez, S. Gallego, M. Ortuno, J. Frances, A. Belendez, and I. Pascual, "Study of the modulation capabilities of parallel aligned nematic liquid crystal on silicon displays," Proc. of SPIE 8855, 885504 (2013).
- [118] J. Xavier, M. Boguslawski, P. Rose, J. Joseph, and C. Denz, "Reconfigurable optically induced quasicrystallographic three-dimensional complex nonlinear photonic lattice structures," Adv. Materials 22, 356-360 (2010).
- [119] V. Arrizon, D. Sanchez-de-la-Llave, G. Mendez, and U. Ruiz, "Efficient generation of periodic and quasi-periodic non-diffractive optical fields with phase holograms," Opt. Express 19, 10553 (2011).
- [120] M. Boguslawski, P. Rose, and C. Denz, "Increasing the structural variety of discrete nondiffracting wave fields," Phys. Rev. A 84, 013832 (2011).
- [121] M. Boguslawski, A. Kelberer, P. Rose, and C. Denz, "Multiplexing complex two-dimensional photonic superlattices," Opt. Express 20, 27331 (2012).
- [122] J. Xavier and J. Joseph, "Tunable complex photonic chiral lattices by reconfigurable optical phase engineering," Opt. Letters 36, 403 (2011).

- [123] J. Li, Y. Liu, X. Xie, P. Zhang, B. Liang, L. Yan, J. Zhou, G. Kurizki, D. Jacobs, K.S. Wong, and Y. Zhong, "Fabrication of photonic crystals with functional defects by one-step holographic lithography," Opt. Express 16, 12899-12905 (2008).
- [124] Kelberer, A., Boguslawski, M., Rose, P., and Denz, C., "Embedding defect sites into hexagonal nondiffracting wave fields," Opt. Letters 37, 5009 (2012).
- [125] Kumar, M., and Joseph, J., "Embedding a nondiffracting defect site in helical lattice wave-field by optical phase engineering," App. Optics 52, 5653 (2013).
- [126] J. Xavier and J. Joseph, "Complex photonic lattices embedded with tailored intrinsic defects by a dynamically reconfigurable single step interferometric approach," Appl. Phys. Lett. 104, 081104 (2014).
- [127] J. Lutkenhaus, D. George, B. Arigong, H. Zhang, U. Philipose, and Y. Lin, "Holographic fabrication of functionally graded photonic lattices through spatially specified phase patterns,"Appl. Opt. 53, 2548-2555 (2014).
- [128] K. Ohlinger, J. Lutkenhaus, B. Arigong, H. Zhang, Y. Lin, "Spatially addressable design of gradient index structures through spatial light modulator based holographic lithography,"

  Journal of Applied Physics, 114, 213102 (2013).
- [129] M. Kumar, and J. Joseph, "Embedding multiple nondiffracting defect sites in periodic lattice wavefield by optical phase engineering," J. of Nanophotonics 8, 083894 (2014).
- [130] M. Kumar, and J. Joseph, "Generating a hexagonal lattice wave field with a gradient basis structure," Opt. Letters 39, 2459 (2014).

- [131] M. Kumar and J. Joseph, "Optical generation of a spatially variant two-dimensional lattice structure by using a phase only spatial light modulator," Appl. Phys. Letters 105, 051102 (2014).
- [132] M. Boguslawski, A. Kelberer, P. Rose, and C. Denz, "Apodized structures for the integration of defect sites into photonic lattices," Appl. Phys. Letters 105, 111102 (2014).
- [133] J. Lutkenhaus, D. George, D. Lowell, B. Arigong, H. Zhang, U. Philipose, and Y. Lin, "Registering functional defects into periodic holographic structures," App. Opt. 54, 7007-7012 (2015).
- [134] A. Kapoor, M. Kumar, P. Senthilkumaran, and J. Joseph, "Optical vortex array in spatially varying lattice," Opt. Comm. 365, 99-102 (2016).
- [135] J. Lutkenhaus, D. Lowell, D. George, H. Zhang, and Y. Lin, "Holographic fabrication of designed functional defect lines in photonic crystal lattice using a spatial light modulator," Micromachines 7, 59 (2016).
- [136] P. Zhang, X. Xie, Y. Guan, J. Zhou, K. Wong, and L. Yan, "Adaptive synthesis of optical pattern for photonic crystal lithography," Appl. Phys. B 104, 113-116 (2011).
- [137] R.C. Rumpf, and J. Pazos, "Synthesis of spatially variant lattices," Opt. Express 20, 15263 (2012).
- [138] R.C. Rumpf, J. Pazos, C.R. Garcia, L. Ochoa, and R. Wicker, "3D printed lattices with spatially variant self-collimation," Progress in EM Research, 139, 1-14 (2013).
- [139] J.L. Digaum, J.J. Pazos, J. Chiles, J. D'Archangel, G. Padilla, A. Tatulian, R.C. Rumpf, S. Fathpour, G.D. Boreman, and S.M. Kuebler, "Tight control of light beams in photonic crystals with spatially variant lattice orientation," Opt. Express 22, 25788 (2014).

- [140] R.C. Rumpf, J. Pazos, J.L. Digaum, S.M. Kuebler, "Spatially variant periodic structures in electromagnetics," Phil. Trans. R. Soc. A 373, 20140359 (2015).
- [141] David F. Edwards, "Silicon (Si)," in Handbook of Optical Constants of Solids, E.D. Palik, ed. (Academic, Orlando, Fla., 1985).
- [142] Y.Lin, P.R. Herman, and K. Darmawikarta, "Design and holographic fabrication of tetragonal and cubic photonic crystals with phase mask: toward the mass-production of three-dimensional photonic crystals," Appl. Phys. Lett. 96, 071117 (2005).
- [143] S.G. Park, M. Miyake, S.M. Yang, and P.V. Braun, "Cu2O Inverse woodpile photonic crystals by prism holographic lithography and electrodeposition," Adv. Mat. 23, 2749-2752 (2011).
- [144] T.Y.M. Chan, O. Toader, and S. John, "Photonic band-gap formation by optical-phase-mask lithography," Phys. Rev. E 73, 046610 (2005).
- [145] J. Xavier, R. Dasgupta, S. Ahlawat, J. Joseph, and P.K. Gupta, "Three-dimensional optical twisters-driven helically stacked multilayered microrotors," Appl. Phys. Lett. 100, 121101 (2012).
- [146] Pendry, J.B., Schurig, D., Smith, D. R., "Controlling Electromagnetic Fields," Science 312, 1780 (2006).
- [147] Leonhardt, U., "Optical Conformal Mapping," Science 312, 1777 (2006).
- [148] J.H. Moon and S. Yang, "Creating three-dimensional polymeric microstructures by multi-beam interference lithography," J. Macromol. Sci. Polym. Rev. C 45, 351-373 (2005).
- [149] Vasic, B., Isic, G., Gajic, R., and Hingerl, K., "Controlling electromagnetic fields with graded photonic crystals in metamaterial regime," Opt. Express 18, 20321-20333 (2010).

- [150] Arigong, B., Shao, J., Ren, H., Zheng, G., Lutkenhaus, J., Kim, H., Lin, Y., and Zhang, Y., "Reconfigurable surface plasmon polariton wave adapter designed by transformation optics," Opt. Express 20, 13789-13797 (2012).
- [151] Levy, U., Nezhad, M., Kim, H.C., Tsai, C.H., Pang, L., and Fainman, Y., "Implementation of a graded-index medium by use of subwavelength structures with graded fill factor," J. Opt. Soc. Am. A 22, 724-733 (2005).
- [152] Smigaj, W., and Gralak, B., "Validity of the effective medium approximation of photonic crystals," Phys. Rev. B 77, 235445 (2008).
- [153] K. Ohlinger, F. Torres, Y. Lin, K. Lozano, D. Xu, and K.P. Chen, "Photonic crystals with defect structures fabricated through a combination of holographic lithography and two-photon lithography," J. Appl. Phys. 108, 073113 (2010).
- [154] Y. Lin, D. Rivera, and K.P. Chen, "Woodpile-type photonic crystal with orthorhombic or tetragonal symmetry formed through phase mask techniques," Opt Express 14, 887-892 (2006).
- [155] Y.J. Hung, S.L. Lee, Y.T. Pan, B.J. Thibeault, and L.A. Coldren, "Holographic realization of hexagonal two-dimensional photonic crystal structures with elliptical geometry," J. Vac. Sci. Technol. B 28, 1030-1038 (2010).
- [156] M. Campbell, D.N. Sharp, M.T. Harrison, R.G. Denning, and A.J. Turberfield, "Fabrication of photonic crystals for the visible spectrum by holographic lithography," Nature 404, 53-56 (2000).

- [157] S. Yang, M. Megens, J. Aizenberg, P. Wiltzius, P.M. Chaikin, and W.B. Russell, "Creating periodic three-dimensional structures by multibeam interference of visible laser," Chem. of Mat. 14, 2831-2833 (2002).
- [158] C.K. Ullal, M. Maldovan, E.L. Thomas, G. Chen, Y.J. Han, and S. Yang, "Photonic crystals through holographic lithography: Simple cubic, diamond-like, and gyroid-like structures," Appl. Phys. Lett. 84, 5434-5436 (2004).
- [159] Y.K. Pang, J.C.W. Lee, H.F. Lee, W.Y. Tam, C.T. Chan, and P. Sheng, "Chiral microstructures (spirals) fabrication by holographic lithography," Opt. Express 13, 7615-7620 (2005).
- [160] W.D. Mao, J.W. Dong, Y.C. Zhong, G.Q. Liang, and H.Z. Wang, "Formation principles of two-dimensional compound photonic lattices by one-step holographic lithography," Opt. Express 13, 2994-2999 (2005).
- [161] G.Q. Liang, W.D. Mao, H. Zou, B.C. Chen, J.F. Cao, Y.Y. Pu, X.W. Wen, and H.Z. Wang, "Holographic formation of large area split-ring arrays for magnetic metamaterials," J. of Mod. Opt. 55, 1463-1472 (2008).
- [162] Z. Poole, D. Xu, K.P. Chen, I. Olvera, K. Ohlinger, and Y. Lin, "Holographic fabrication of three-dimensional orthorhombic and tetragonal photonic crystal templates using a diffractive optical element," Appl. Phys. Lett. 91, 251101 (2007).
- [163] D. Chanda and P. Herman, "Phase tunable multilevel diffractive optical element based single laser exposure fabrication of three dimensional photonic crystal templates," Appl. Phys. Lett. 91, 061122 (2007).

- [164] D. Chanda, L.E. Abolghasemi, and P. Herman, "Single laser exposure fabrication of diamond-like 3-dimensional photonic crystal microstructures using circularly polarized light," Appl. Phys. A 93, 33-37 (2008).
- [165] N.D. Lai, W.P. Liang, J.H. Lin, and C.C. Hsu, "Rapid fabrication of large-area periodic structures containing well-defined defects by combining holography and mask techniques,"

  Opt. Express 13, 5331-5337 (2005).
- [166] V. Ramanan, E. Nelson, A. Brzezinski, P.V. Braun, and P. Wiltzius, "Three-dimensional silicon-air photonic crystals with controlled defects using interference lithography," Appl. Phys. Lett. 92, 173304 (2008).
- [167] Y. Zhong, L. Wu, H. Su, K.S. Wong, and H. Wang, "Fabrication of photonic crystals with tunable surface orientation by holographic lithography," Opt. Express 14, 6837-6843 (2006).
- [168] G.Q. Liang, W.D. Mao, Y.Y. Pu, H. Zou, H.Z. Wang, and Z.H. Zeng, "Fabrication of two-dimensional coupled photonic crystal resonator arrays by holographic lithography," Appl. Phys. Lett. 89, 041902 (2006).
- [169] D.C. Meisel, M. Wegener, and K. Busch, "Three-dimensional photonic crystals by holographic lithography using the umbrella configuration: Symmetries and complete photonic band gaps," Phys. Rev. B, 165104 (2004).
- [170] T.Y.M. Chan and S. John, "Circuits for light in holographically defined photonic band-gap materials," Phys. Rev. A 78, 033812 (2008).
- [171] G.M. Burrow, M.C.R. Leibovici, and T.K. Gaylord, "Pattern-integrated interference lithography: single exposure fabrication of photonic crystal structures," Appl. Opt. 51, 4028-4041 (2012).

- [172] M.C.R. Leibovici and T.K. Gaylord, "Custom-modified three-dimensional periodic microstructures by pattern-integrated interference lithography," J. Opt. Soc. Am. A 31, 1515-1519 (2014).
- [173] M.C.R. Leibovici and T.K. Gaylord, "Photonic crystal waveguide structure by pattern-integrated interference lithography," Opt. Lett. 40, 2806-2809 (2015).
- [174] A. Lizana, N. Martin, M. Estape, E. Fernandez, I. Moreno, A. Marquez, C. Iemmi, J. Campos, and M.J. Yzuel, "Influence of incident angle in the performance of Liquid Crystal on Silicon displays," Opt. Express 17, 8491-8505 (2009).
- [175] Q. Zhou, W. Yang, F. He, R. Stoian, R. Hui, and G. Cheng, "Femtosecond multi-beam interference lithography based on dynamic wavefront engineering," Opt. Express 21, 9851 (2013).
- [176] G. Zito, B. Piccirillo, E. Santamato, A. Marino, V. Tkachenko, and G. Abbate, "Two-dimensional photonic quasicrystals by single beam computer-generated holography," Opt. Express 16, 5164-5170 (2008).
- [177] J. Becker, P. Rose, M. Boguslawski, and C. Denz, "Systematic approach to complex periodic vortex and helix lattices," Opt. Express 19, 9848 (2011).
- [178] MATLAB R2015a, The Mathworks, Inc., Natick, MA (2015).